Title
Probing Luttinger Liquid Plasmons in Single Walled Carbon Nanotubes

Author
Wang, Sheng

Publication Date
2020

Peer reviewed|Thesis/dissertation

Probing Luttinger Liquid Plasmons in Single Walled Carbon Nanotubes

By

Sheng Wang

A dissertation submitted in partial satisfaction of the

requirements for the degree of

Doctor of Philosophy

in

Physics

in the

Graduate Division

of the

University of California, Berkeley

Committee in charge:

Professor Feng Wang, Chair

Professor Michael F. Crommie

Professor Eli Yablonovitch

Spring 2020

Abstract

Probing Luttinger Liquid Plasmons in Single Walled Carbon Nanotubes

By

Sheng Wang

Doctor of Philosophy in Physics

University of California, Berkeley

Professor Feng Wang, Chair

Single walled carbon nanotubes (SWNTs) are one-dimensional (1D) rolled-up hollow cylinders composed of graphene sheets. Since their discovery about three decades ago, they have been one of the most fascinating and unique nanoscale structures. There have been tremendous and still ongoing research on SWNTs for both fundamental science as well as technological devices. SWNTs have been a good platform to study electron-electron interaction in solid state systems, including Coulomb blockage effect and Luttinger liquid formulism. SWNTs exhibit unique electrical, mechanical and thermal properties, making them potentially useful in a variety of applications including nano-electronics, optics, energy storage, and nanomedicine. Notably, carbon nanotube field-effect transistor-based digital circuits may be a viable route for next-generation beyond-silicon electronic systems for post-Moore's Law era. Recent major advance includes a 16-bit computer built entirely from carbon nanotube transistors.

Despite the intense established research, SWNTs have never ceased to surprise researchers with their emerging properties and potential applications. During the past decade, advances in the synthesis and processing have enabled the controlled growth of high quality ultralong SWNTs on different substrates even with desirable chirality. On the other hand, developments in powerful surface science characterization tools provide a viable route to probe the electronic and optical properties of individual SWNTs. We take advantage of these advances mainly in two ways. First, we grow ultraclean and very long SWNTs on hexagonal boron nitride (h-BN) flakes and fabricate them into field-effect transistor (FET) devices to tune their carrier density. Second, we optimize the performance of recently developed infrared scanning near-field microscopy (IR-SNOM) to achieve measurements of plasmonic excitations of individual SWNTs even at low electron densities.

In the first chapter of the dissertation, I will introduce the fundamental properties of SWNTs. I will also discuss the Luttinger liquid formulism in 1D systems and the emerging nonlinear Luttinger liquid theory accounting for the effects of nonlinear band dispersion on the electron excitations. IR-SNOM, the main experiment tool we employ to probe the Luttinger liquid plasmons, will also be introduced.

In the following chapters, I will discuss our findings and understandings achieved by infrared nanoimaging of SWNT FET devices supplemented with electronic transport. We experimentally

demonstrate the logarithm diameter scaling and carrier density independence of Luttinger liquid plasmons in metallic SWNTs. The unusual behaviors are signatures of the Luttinger liquid and stand in sharp contrast with conventional plasmons in metallic nanoshells. We further correlate infrared nano-imaging measurements and electrical tunneling at a cross junction between two metallic SWNTs, providing a parameter free test of the Luttinger liquid theory in SWNTs. While metallic SWNTs with linear band dispersion are perfect realizations of the linear Luttinger liquid, semiconducting SWNTs featuring hyperbolic band dispersion deviates from the paradigm. We demonstrate that electric-field tunable plasmonic excitations in semiconducting SWNTs behave consistently with the nonlinear Luttinger liquid theory, providing a platform to study non-conventional one-dimensional electron dynamics and realize integrated nanophotonic devices. We further fabricate individual SWNT nanocavities of controllable length by scanning probe nanolithography. We resolve the plasmon resonance of individual nanotube cavities by spectrally resolved infrared nanoimaging. These findings and understandings reveal the unusual 1D electron dynamics in metallic and semiconducting SWNTs and lay the foundation for carbon nanotube plasmonics.

To My Parents

Xingyu Chen & Taifang Qin

Table of contents

Acknowledgements

It has been a wonderful experience pursuing my graduate study at Wang Lab at Berkeley physics department. I remember myself as an ambitious and aspiring young man with big smiles when I first stepped into this beautiful campus. Looking over the bay area for the first time from the top of the Campanile tower, I had the feeling that I was going to make a big difference. Six years has passed and there comes the graduation. I went back to the top of the Campanile tower again. The view was still gorgeous just as six years ago, but my mindset and my understanding had significantly improved. Thinking back, I experienced ups and downs in my research as well as in my mindset. I even spent one whole night sitting on the bench near the Campanile tower, looking up at the stars with my mind wandering around the universe. During the graduate study, I believe I have gradually grasped how to become a good researcher and gained invaluable understandings about myself and the universe. This growth in my research and mindset cannot happen without Wang group members and other colleagues and friends.

I would like to thank my advisor Feng Wang for his guidance and support during my graduate study. I learned a lot from his deep thinking and intuitive explanation. From interaction with him, I gradually learned how to identify the most important problems in a field and then how to work out a solution. He acted as a plasmonic nanoparticle for me. Near him, I get substantial enhancement of thinking and working.

I would also like to thank Prof. Y.R. Shen, who offers critical comments on scientific problems and invaluable advice on academic career. He is a great scientist to look up to and learn from.

I'm also genuinely grateful to my lab mates in the Wang group. When I first joined the group, Dr. Zhiwen Shi and Dr. Lili Jiang introduced to me how to prepare samples and perform infrared nanoimaging. I also learned a lot about nanophotonics from many discussions with Dr. Jihun Kang. I would also like to thank Dr. Sihan Zhao on device fabrications. Also, I want to thank all the other lab mates in Wang group for their support and help. They are Dr. Chenhao Jin, Dr. Wenyu Zhao, Dr. Long Ju, Dr. Sufei Shi, Dr. Jonghwan Kim, Dr. Jason Horng, Dr. Bo Zeng, Dr. SeokJae Yoo, Dr. Shaowei Li, Dr. Yoseob Yoon, Dr. Zuocheng Zhang, Dr. Alexander Zibrov, Iqbal Utama, Danqing Wang, Tairu Lyu, Shaoxin Wang, Emma Regan, Steve Drapcho, Halleh B. Balch, Hongyuan Li, Shilong Zhao, Jiu Chang. I also get a lot of help and support from many students and postdocs not in Wang group, including Dr. Zhaoli Gao, Dr. Qicheng Zhang, Weicheng Zhong, Minliang Lai, Zhihang Wang, Meng Wu and Yi Chen.

Many findings are accompanied by great collaboration with different groups inside and outside of Berkeley. I want to thank Prof. Chongwu Zhou and Dr. Fanqi Wu for the close and long-term collaboration. I also want to thank Prof. Alex Zettl for the help on device fabrication.

I would also like to thank the considerate and patient staff members in our department and at the international house office. They make my life much easier as an international student at Berkeley physics. I would like to pay special thanks to my parents and friends for their continuous encouragement in the period of self-doubt when things didn't go smoothly. I also want to pay gratitude to myself for the extraordinary gift for hope, strong optimism and childish enthusiasm. With the encouragement, determination and hope, I was able and will continue to get off the ground and get things done.

Chapter 1 – Introduction

1.1 Background and Motivation

Single walled carbon nanotubes (SWNTs) can be viewed as seamless hollow cylinders rolled up from graphene sheets. They have been pursued aggressively as an exceptional nanomaterial over the last three decades[1-6]. SWNTs offer a versatile platform for various aspects of studies in condensed matter physics. Electronic transport in SWNTs reveals intriguing physical phenomena in the 1D system including conductance quantum, Coulomb blockade, Luttinger liquid physics, spin-valley physics[7, 8]. Rich exciton physics, Raman spectroscopy and nonlinear optics are among extensive optical studies of SWNTs[1, 2, 9]. With the remarkable combination of ultrastrong strength, unique electrical and optical properties, vast applications based on SWNTs have been proposed and investigated. The applications include realistic ones such as nanoelectronics and bio/molecular nanosensors to fanciful ones including carbon nanotube-based space elevator[4, 6, 10-12].

The excitements about SWNTs have diminished in the last decade. More research has been directed to emerging materials such as graphene and other 2D materials. Some unfinished work and unanswered questions remain in the field of SWNTs. Recent progress in controlled synthesis of SWNTs and advanced characterization tools enable a revisit to problems previously beyond reach[13-15]. Some notable examples are the observation of electronic Wigner crystal in SWNTs by an ultrasensitive scanning probe down to single electron level and a 16-bit computer built entirely from carbon nanotube transistors[16, 17]. We seem to have gone past the "Trough of Disillusionment" and are moving towards the "Slope of Enlightenment" in the Gartner Hype Cycle curve[18].

In this thesis, I present my research on probing Luttinger liquid plasmons in SWNTs standing upon the latest advances in growth of ultraclean SWNTs on h-BN and developments in infrared nanoimaging techniques[19-22]. We established experimentally the unusual phenomenology that plasmon excitation in 1D metallic SWNTs can be completely independent of charge carrier and provided an experimental determination of the Luttinger liquid parameter and its logarithm scaling with the nanotube diameter. We combined electrical tunneling and infrared nano-imaging measurement in a SWNT tunneling junction to provide the first definitive parameter-free test of the Luttinger liquid phenomena in SWNTs. We achieved electric-field tuning of nonlinear Luttinger liquid plasmons in semiconducting SWNTs which provides experimental demonstration of 1D electron dynamics beyond the conventional linear Luttinger liquid paradigm. We establish semiconducting SWNTs as a great platform to study nonconventional 1D electron excitations and dynamics and realize integrated nanophotonic devices. Plasmonic resonance of individual metallic SWNT nanocavities was resolved by spectrally resolved infrared nano-imaging. These new understanding and findings serve as a small renewed step among the giant resurgent research on SWNTs to unlock their potential as a wonder nanomaterial for numerous futuristic applications.

1.2 Outline of Thesis

Chapter 2 introduces the basics of SWNTs, the Luttinger liquid physics in one dimension and infrared scanning near-field optical microscopy (IR-SNOM).

Chapter 3 discusses the peculiar signatures of Luttinger liquid plasmons in SWNTs visualized by IR-SNOM, including the intriguing logarithm diameter scaling and counterintuitive carrier density independence. These peculiar plasmon signatures agree excellently with the Luttinger liquid theory and stand in stark contrast to plasmons in conventional metal nanostructures.

Reference: Sheng Wang, *et al.* Logarithm Diameter Scaling and Carrier Density Independence of One-Dimensional Luttinger Liquid Plasmon. *Nano Letters*, *19*(4), 2360-2365 (2019).

Chapter 4 demonstrates a parameter-free test of the Luttinger liquid theory by correlating two completely distinct physical properties i.e. electron tunneling and plasmon propagation in the same Luttinger liquid system, which are controlled by the same Luttinger liquid parameter. This is achieved by a direct combination of electrical transport and optical nanoscopy on the same metallic SWNT cross junctions, which provides independent experimental determination of Luttinger parameters through the power-law electron tunneling and the renormalized plasmon propagation velocity, respectively.

Reference: Sihan Zhao, Sheng Wang, *et al.* Correlation of Electron Tunneling and Plasmon Propagation in a Luttinger Liquid. Physical Review Letters, *121(4), 047702* (2018).

Chapter 5 discusses nonlinear Luttinger liquid plasmons in semiconducting SWNTs. The infrared nanoimaging of gate tunable plasmons in semiconducting SWNTs reveals that the lifetime of plasmonic excitations in semiconducting SWNTs is found to strongly depend on the carrier density, which is well captured by the nonlinear Luttinger liquid theory. The findings establish semiconducting SWNTs as a model system to study non-conventional one-dimensional electron dynamics and realize integrated nanophotonic devices.

Reference: Sheng Wang, *et al.* Nonlinear Luttinger liquid plasmons in semiconducting single-walled carbon nanotubes. *Nature Materials, 1-6* (2020).

Chapter 6 presents the study of probing plasmon resonance of individual plasmonic carbon nanotube nanocavity. We demonstrate that metallic SWNT nanocavities serve as one of the most compact nanoplasmonic elements with exceptional tunability and low loss. For a broad spectrum from near-infrared to terahertz light, SWNT plasmonic nanocavities could serve in a role analogous to that of metallic nanostructures for visible frequencies, which paves the way for various nanophotonic applications based on plasmons in SWNTs.

References: Sheng Wang, *et al.* Metallic Carbon Nanotube Nanocavities as Ultracompact and Low-loss Fabry–Perot Plasmonic Resonators. *Nano Letters, 20(4), 2695-2702* (2020).

Chapter 2 – Introduction to SWNTs, Luttinger liquid, IR-SNOM

2.1 Basics of SWNTs

Graphene is a plane layer of carbon atoms bonded together in honeycomb lattice as shown in Figure 2.1a[23-25]. SWNTs can be viewed as rolled-up versions of graphene sheets. To understand the fundamental properties of SWNTs, we can start with the band structures of graphene. Figure 2.1b shows the Bravais lattice of graphene with primitive lattice vectors $\boldsymbol{a_1}$ and $\boldsymbol{a_2}$. The carbon-carbon bond length is a = 0.142 nm. The reciprocal lattice vectors $\mathbf{b_1}$ and $\mathbf{b_2}$ are defined by $\boldsymbol{a_i} \cdot \boldsymbol{b_j} = 2\pi\delta_{ij}$. The first Brillouin zone of the graphene reciprocal lattice is shown in Figure 2.1b in the form of a hexagon with an edge length of $4\pi/3a$.

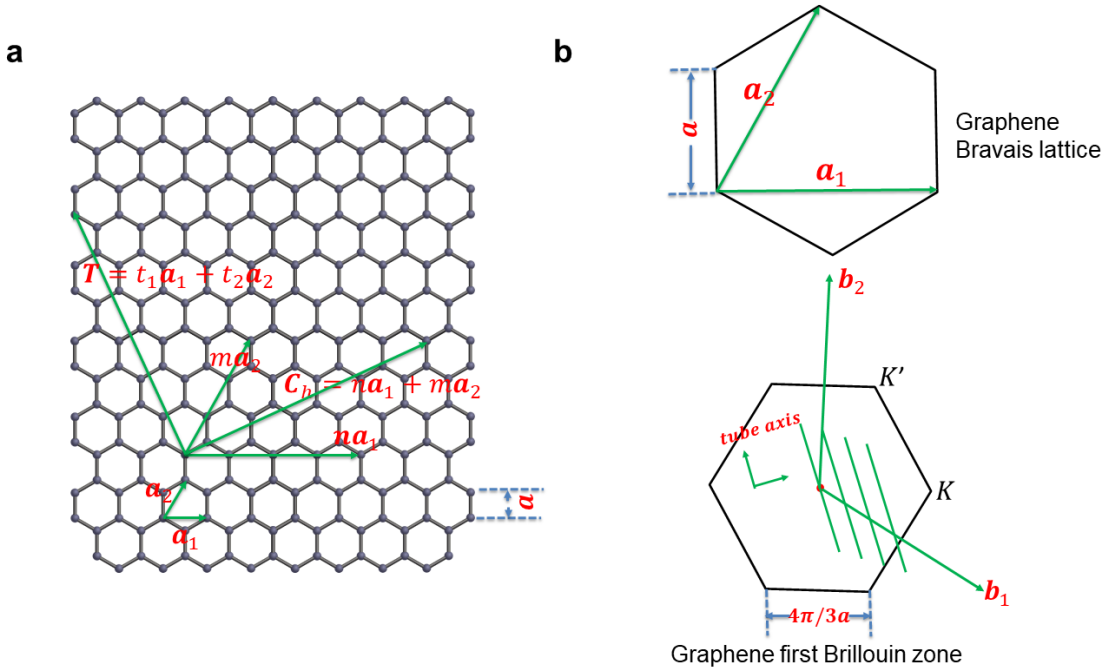

Figure 2.1 Relation between nanotube and graphene through the chiral vector $\boldsymbol{C_h}$. (a) A nanotube with chiral index (n, m) corresponds to a chiral vector $\boldsymbol{C_h} = n\boldsymbol{a_1} + m\boldsymbol{a_2}$, and is formed by rolling up the chiral vector into a closed circle. The 1D translational vector $\boldsymbol{T}$ is parallel to the nanotube axis and normal to $\boldsymbol{C_h}$. (b) Primitive lattice of graphene with lattice vectors $\boldsymbol{a_1}$ and $\boldsymbol{a_2}$ and its corresponding reciprocal lattice with vectors $\mathbf{b_1}$ and $\mathbf{b_2}$.

Graphene is known to host relativistic Dirac electrons in the proximity at *K/K'* points in the reciprocal lattice. The Hamiltonian of graphene can be written in the form $\widehat{H} = \hbar v_0 \boldsymbol{\sigma} \cdot \boldsymbol{k}$, where $\boldsymbol{\sigma} = (\sigma_x, \sigma_y)$ and $\boldsymbol{k} = (k_x, k_y)$ are respectively the Pauli operator and wavevector in 2D, v_0 is the graphene Fermi velocity. The eigenvalues of the Hamilton are $E(k) = s\hbar v_F|k|$, where $s = \pm 1$,

corresponding to conduction and valence bands. The corresponding eigenvector, i.e., the electron wavefunction is $|sk\rangle = \frac{1}{\sqrt{2}}\binom{1}{se^{i\theta_k}}e^{i\boldsymbol{k}\cdot\boldsymbol{r}}$, where $\theta_k = arctan(k_y/k_x)$ is the polar angle.

An essential aspect of SWNTs is its chirality describing the how the graphene is wrapped up. The chirality of a SWNT can be specified by the chiral vector $\boldsymbol{C}_h = n\boldsymbol{a}_1 + m\boldsymbol{a}_2$, where n, m are integers $0 \leq m \leq n$ and (n, m) is the chiral index. SWNTs have very large aspect ratios (10^4-to^5) and the two ends of a nanotube in the form of fullerene caps can be neglected. For a first step, we can further neglect the curvature effects due to the rolling up. The band structure of a SWNT will be directly associated with that of graphene and is uniquely determined by the chiral index. Armchair nanotubes have an index (n, n) with n = m and zigzag nanotubes have an index (n, 0) with m = 0. Both armchair and zigzag nanotubes are achiral nanotubes because they have a mirror image that is identical to its original structure. All other nanotubes are chiral ones. The chiral vector $\boldsymbol{C}_h$ forms the circumference of the cylinder and the diameter of a nanotube is thus $d = |\boldsymbol{C}_h|/\pi = |n\boldsymbol{a}_1 + m\boldsymbol{a}_2|/\pi = \sqrt{3}a\sqrt{n^2 + m^2 + mn}/\pi$. Depending on the ratio between n and m, there will be an angle θ between $\boldsymbol{C}_h$ and $\boldsymbol{a}_1$, given by $\theta = \tan^{-1}\frac{\sqrt{3}m}{2n+m}$. θ is referred to as the chiral angle of a nanotube with values in the range of 0 to 30 degrees due to the hexagonal symmetry of the honeycomb lattice.

We can further determine the unit vector of a given nanotube along the axis by searching for the shortest lattice vector $\boldsymbol{T}$ of graphene that is normal to $\boldsymbol{C}_h$. A general form of the unit vector $\boldsymbol{T}$ can be expressed as $\boldsymbol{T} = (t_1\boldsymbol{a}_1 + t_2\boldsymbol{a}_2)$ where $\boldsymbol{t_1} = \frac{(n+2m)}{d_R}, t_2 = \frac{(2n+m)}{d_R}$, $d_R = \gcd(n + 2m, 2n + m)$ is the greatest common divisor of $(n + 2m)$ and $(2n + m)$. The unit cell of the 1D SWNT is the rectangle defined by the vectors $\boldsymbol{C}_h$ and $\boldsymbol{T}$. In SWNTs, the two ends of $\boldsymbol{C}_h$ are connected so that the electron wavefunction should satisfy $\psi(\boldsymbol{r}) = \psi(\boldsymbol{r} + \boldsymbol{C}_h)$. This periodic boundary condition leads to the quantization of wavevector in the circumferential direction whereas the wavevector along the nanotube axis remains continuous for nanotube of infinite length. Due to the wavevector constraints imposed by the quantization, the band structure of a 1D SWNT is represented be by a set of 1D energy dispersion relations which are described by discrete cutting lines separated by $\Delta\boldsymbol{k}_\mu = 2\pi/C_h$ in 2D graphene band structure. These cutting lines are labeled by an integer μ. If for a nanotube with chiral index (n, m), the cutting line passes through a *K* point of the 2D graphene Brillouin zone (Figure 2.1b), the 1D energy band will be a linear Dirac band with a constant density of states below the second energy subband. These nanotubes are thus metallic. For other nanotubes with chiral index such that the cutting lines don't pass through a *K* point of the 2D graphene Brillouin zone, the nanotube is expected to exhibit semiconducting behaviors with a finite bandgap. The condition for metallic nanotubes is that the wavevector at *K* point satisfies the quantization condition, or equivalently, $\boldsymbol{C}_h \cdot \boldsymbol{k}(K) = 2\pi\mu$, where $\boldsymbol{C}_h = n\boldsymbol{a}_1 + m\boldsymbol{a}_2$ is the chiral vector, $\boldsymbol{k}(K) = 2/3\mathbf{b_1} + 1/3\,\mathbf{b_2}$ is the wavevector at *K* point and μ is an integer. Using $\boldsymbol{a_i} \cdot \boldsymbol{b_j} = 2\pi\delta_{ij}$, the condition is reduced to (2n + m)/3 = $2\pi\mu$ or equivalently (n – m) is a multiple of 3. Note that armchair nanotubes with chiral index (n, n) are always metallic, whereas zigzag nanotubes with chiral index (n, 0) are metallic only when n is a multiple of 3.

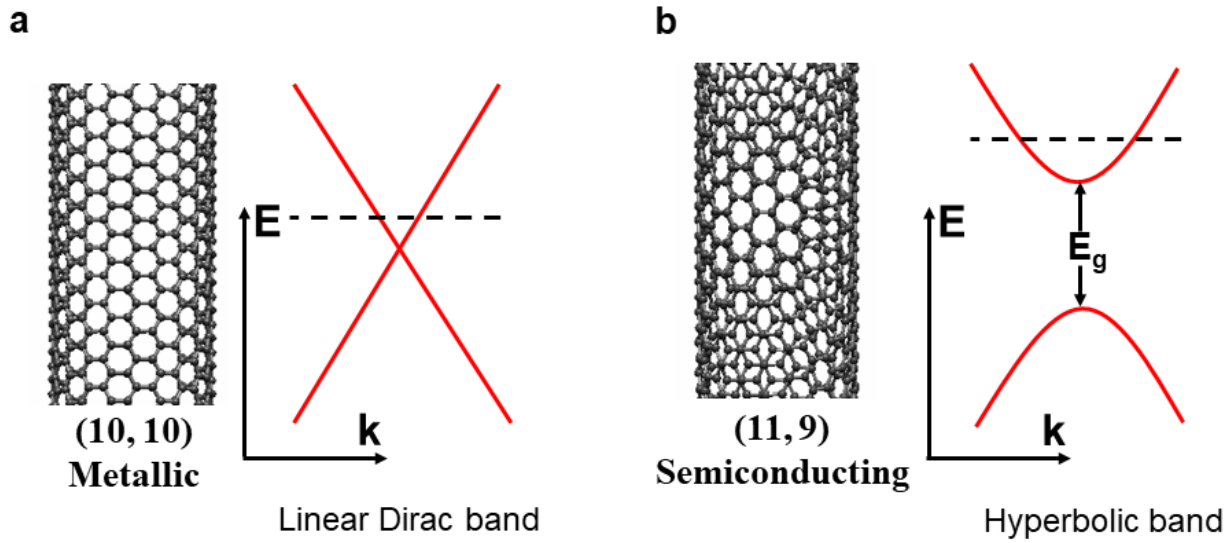

Figure 2.2 Band structures of metallic and semiconducting nanotubes. (a) Metallic nanotubes, with a chiral index (10, 10) as an example, have a linear Dirac band. (b) Semiconducting nanotubes, with a chiral index (11, 9) as an example, have a hyperbolic band with a finite bandgap E_g. Nanotubes (10, 10) and (11, 9) have completely different electronic properties though they have similar diameters.

Figures 2.2a and 2.2b show the respective band structures of metallic and semiconducting SWNTs. Metallic nanotubes, for instance with a chiral index (10, 10), have a linear Dirac band, $E = \hbar v_0 k_F$, where $\hbar$ is the reduced Planck's constant, $v_0 \sim 0.8 \times 10^6\ m/s$ is the Fermi velocity in graphene, and k_F is the Fermi wavevector. In contrast, semiconducting nanotubes, for instance with a chiral index (11, 9), have a hyperbolic band with a finite bandgap E_g, $E^2 = (E_g/2)^2 + (\hbar v_0 k_F)^2$. Nanotubes (10, 10) and (11, 9) have similar diameters but completely different electronic properties. The bang gap E_g is determined by the cutting line closet to the K point. The closest distance between this cutting line to K point can be determined to be $\Delta k = \frac{2\pi}{3C_h}$, where $C_h = \pi d$ is the circumference of the nanotube cylinder. The band gap of the semiconducting nanotube is then $E_g = 2\hbar v_0 \Delta k = \frac{4\hbar v_0}{3d}$. The band gap of a semiconducting nanotube is inversely proportional to the nanotube diameter d as $E_g = 0.75eV/d\ (nm)$.

Note that the discussion above has neglected curvature effects, which are known to have profound effects on the band dispersion, especially for nanotubes with small diameters. Considering the curvature effects, armchair nanotubes remain metallic owing to symmetry. Other metallic nanotubes will have a small gap inversely proportional to $1/d^2$ and are referred to as semimetallic nanotubes. In some extreme cases, the curvature induced hybridization of σ and π electrons can turn a semiconducting nanotube into a metallic one[26-28].

SWNTs with their unique electrical, optical and mechanical properties have been intensively studied for fundamental science as well as technological nanodevices. Transistors based on semiconducting SWNTs have been proposed to replace silicon transistors with their high on-off ratio and larger current density[29]. Steady progress has been made along this way including a

recent breakthrough, a 16-bit computer that is built entirely from carbon-nanotube transistors[16]. Metallic SWNTs and films have been proposed as transparent conductors. Electron-electron interaction is also greatly enhanced in one dimension and can greatly alter the electron behaviors. Coulomb blockade effects and Luttinger liquid behaviors have been reported. Electronic Wigner crystal in SWNTs is also observed thanks to an ultrasensitive scanning probe down to single electron level[17]. The strong Coulomb interactions also lead to strongly bound electron-hole pairs, called excitons, with a binding energy on the order of 300 to 500 meV[2, 30, 31]. The unique optical properties and the abundance of various nanotubes also promise carbon nanotube-based optoelectronic devices. SWNTs have also been widely explored as ultrasensitive bio/chemical nanosensors[32]. They also find applications in biomedicine as a nanochannel to deliver tiny chemicals to cells[33].

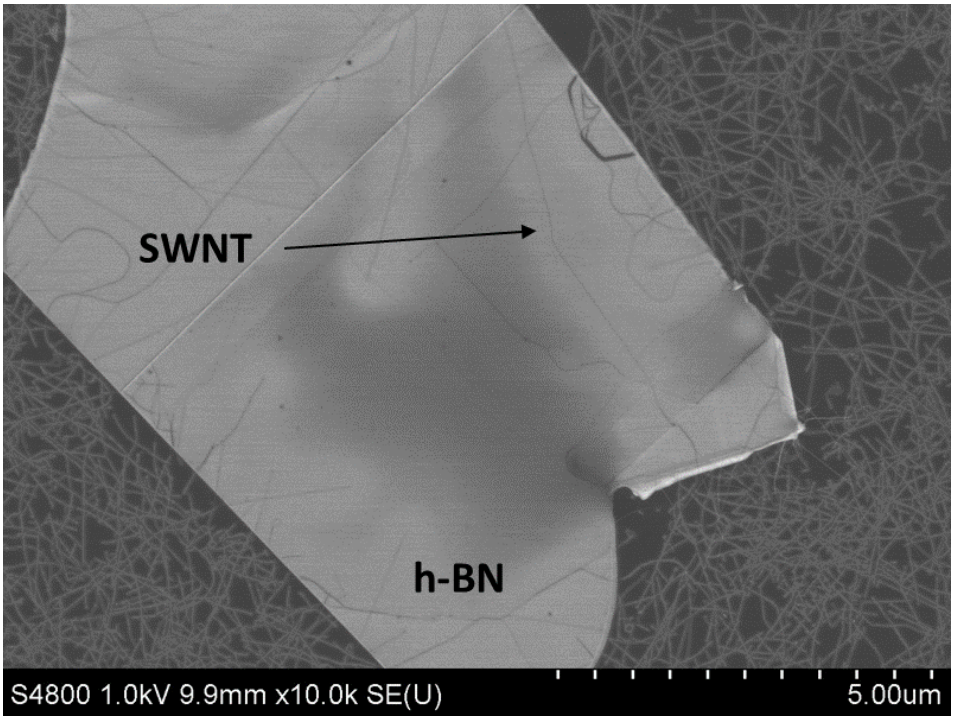

Figure 2.3 A Scanning electron microscope (SEM) image of high quality SWNTs grown directly on h-BN flakes by chemical vapor deposition.

A major challenge in the nanotube community is the controlled synthesis of SWNTs in a scalable and environmental way[18]. Chirality control in nanotube synthesis is still under intense investigation through the combination of experimental analysis and theoretical modeling. Intense research directed to 2D materials including graphene has brought new insight to the field of SWNTs. Lessons and experiences from the 2D community can provide some novel guidance to the synthesis, characterization and modeling of SWNTs. Recent progress in controlled synthesis of SWNTs and advanced characterization tools with nanoscale resolution enable further interrogation of SWNTs at their intrinsic level.

One big advance towards ultraclean SWNTs in our set of experiments is the usage of hexagonal boron nitride (h-BN) flakes as the substrates for SWNTs. H-BN flakes have been well

established in the 2D community to be ideal substrates for nanomaterials because they are atomically flat and contain very few impurities compared to more conventional substrates such as SiO_2/Si substrates. Nanomaterials with properties easily susceptible to environmental surroundings can thus remain pristine when placed on h-BN flakes. Figure 2.3 displays a scanning electron microscope (SEM) image of high quality SWNTs grown directly on h-BN flakes by chemical vapor deposition (CVD). The CVD method is as follows: Ferritin solution (0.1 mmol L^{-1}) is drop-casted onto SiO_2/Si substrates (SiO_2, 285 nm). The substrates are incubated at room temperature for 10 min. The substrates are then rinsed with isopropyl alcohol and are subsequently blow-dried. The substrates are annealed in air at 900 °C for 30 min to convert ferritin to Fe_2O_3 nanoparticles. Then h-BN flakes are mechanically exfoliated onto the SiO_2/Si substrates with Fe_2O_3 nanoparticles. High-quality SWNTs are then directly grown on the substrates by CVD. We use an ambient-pressure CVD system equipped with a one-inch quartz tube. The system is first purged with hydrogen gas for 10 min to get rid of the air. After that, the temperature is raised to 900 °C in 15 min under 300 sccm of hydrogen flow. When the temperature reaches 900 °C, 110 sccm of argon is introduced through a bubbler with ethanol, which works as the carbon precursor, while 300 sccm of hydrogen flow is maintained to reduce iron compound nanoparticles to iron nanoparticles, which act as catalysts for SWNT growth. The temperature is kept at 900 °C for 15 min, followed by naturally cooling to room temperature under a hydrogen flow of 300 sccm.

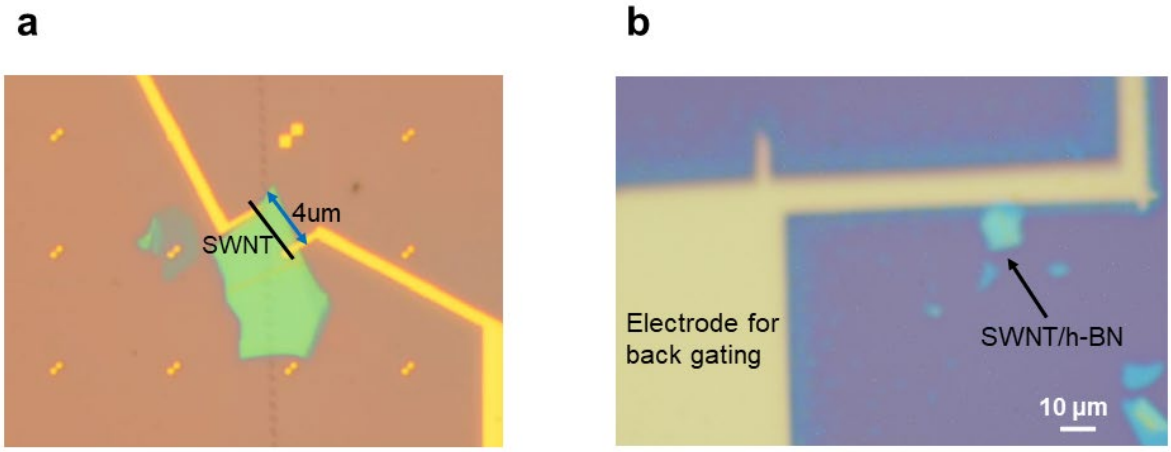

Figure 2.4 Optical image of SWNTs in FET nanodevices. (a) An SWNT FET nanodevice with two electrodes for electronic transport. (b) An SWNT FET device with one electrode for infrared nanoimaging. By applying a gate voltage between the electrode and the conductive Si layer, we can continuously tune the carrier density in the SWNT while in situ performing infrared nanoimaging.

SWNTs with different species can be grown by this method. The nanotubes are also very long on h-BN substrates and can be readily fabricated into field-effect transistor (FET) nanodevices for electronic transport measurements. Electrical contacts on the SWNTs are fabricated using standard e-beam lithography or shadow masks. E-beam lithography is used to define two electrodes for electronic transport measurements. For individual nanotube transport measurement, SWNTs on SiO_2 are thoroughly eliminated by an oxygen plasma, with the nanotube between the electrodes left for transport measurement. Figure 2.4a displays an as-fabricated SWNT FET nanodevice with a channel length of 4 μm. Shadow masks are used to define one contact for back gating to avoid polymer contamination and to keep the nanotubes ultraclean for gate-controlled infrared nano-imaging. An optical image of an-fabricated SWNT FET nanodevice is shown in Figure 2.4b. By

applying a gate voltage between the electrode and Si layer, we can continuously tune the carrier density in the SWNT while in situ performing infrared nanoimaging. Our combined infrared nanoimaging and electronic transports indicate the SWNTs on h-BN have a remarkable mean free path and carrier relaxation life, which is comparable to SWNTs of the highest quality reported in literature. These ultraclean SWNTs in FET configuration allow interrogation of intrinsic properties of SWNTs even at low carrier concentration.

2.2 Luttinger Liquid in SWNTs

Electrons in three- and two-dimensional metals are described by quasiparticles as in the Fermi liquid theory[34]. Despite the electron-electron interactions in a Fermi liquid, electrons interact with the surrounding in such a way that the net effect of the interactions is to make the fermions behave as dressed quasiparticles. Electrons in the interacting Fermi liquid system thus have an ono-to-one correspondence to fermions in a noninteracting Fermi gas system. The quasiparticles carry the same spin, charge and momentum as the original particles but with renormalized dynamic properties such as effective mass and magnetic momentum. This picture breaks down in one dimension due to enhanced electron-electron correlation.

The reason for relatively weak correlation between electrons in 3D and 2D metals is that they are free to propagate in any direction, limiting the time over which they are close to each other and may interact strongly[35]. In 1D, however, electrons with the same energy propagating in the same direction will have the same Fermi velocity. As a result, they can remain close to each other for a long time and interact strongly during the propagation. This can also be understood in the scattering cross section in the momentum space. For 3D and 2D metals, the Fermi surfaces respectively consist of a sphere and a circle. Coulomb interactions cause scattering among electrons near the Fermi surface. Due to the constraints imposed by Pauli's exclusion principle and energy/momentum conservation, the phase space volume of possible states after scattering is limited[36]. The scattering rate for electrons with energy E near Fermi energy E_F is $\frac{1}{\tau_{ee}} \sim \left(\frac{1}{\tau_0}\right)\left(\frac{E}{E_F}\right)^2$, where $\frac{1}{\tau_0}$ is the classical scattering rate. As the energy E becomes small, the scattering rate becomes negligible compared to its energy, which ensures well-defined quasiparticles near the Fermi surface. In 1D however, energy and momentum have a one-to-one correspondence because energy is locally linear in k. In the scattering process, momentum is simultaneously conserved when energy conservation is satisfied. The scattering rate becomes $\frac{1}{\tau_{ee}} \sim \left(\frac{1}{\tau_0}\right)\frac{E}{E_F}$, on the order of its energy. The energy corresponding to this scattering rate $\hbar\frac{1}{\tau_{ee}}$ thus cannot be neglected even when the energy is small. As a result, the concept of free quasiparticles with well-defined energy breaks down in 1D. The fundamental excitations in 1D systems are collective in nature and should be described by the Luttinger liquid theory instead of the Fermi liquid theory[37-39].

Metallic SWNTs with its linear band dispersion provide an attractive realization of a Luttinger liquid[40]. As discussed in Chapter 2.1, the free particle Hamiltonian without Coulomb interaction

can be written as $H_0 = \sum_{\alpha\beta} \int dx v_0 [\psi^\dagger_{R\alpha\beta} i\partial_x \psi_{R\alpha\beta} - \psi^\dagger_{L\alpha\beta} i\partial_x \psi_{L\alpha\beta}]$, where *R, L* represent right and left moving particles, α and β are spin and valley indices respectively, v_0 is the Fermi velocity. Through Bosonization $\psi_{R/L\alpha\beta} = e^{i(\phi_{\alpha\beta} \pm \theta_{\alpha\beta})}$, the free particle Hamiltonian takes the form $H_0 = \sum_{\alpha\beta} \mathcal{H}_0(\theta_{\alpha\beta}, \phi_{\alpha\beta})$ and $\mathcal{H}_0(\theta, \phi) = \int dx \frac{\hbar v_0}{2\pi} [(\partial_x \theta)^2 + (\partial_x \phi)^2]$, where electron density in a given channel given by $\rho_{\alpha\beta} = (\partial_x \theta_{\alpha\beta}/\pi)$. The Coulomb interaction can be introduced by the charging energy to the nanotube. For an individual suspended SWNT of radius R screened by a concentric metal shell of radius R_s, the energy it takes to charge a unit length of a nanotube is $\mathcal{H}_{int} = \frac{e^2}{4\pi\varepsilon_{eff}} \rho^2 \ln(R_s/R)$, where $\rho = \sum_{\alpha\beta} (\partial_x \theta_{\alpha\beta}/\pi)$ is the total charge density.

The interaction Hamiltonian $\mathcal{H}_{int}$ involves only ρ and we can rewrite the four channels as $\theta_\rho = 1/(\sqrt{4})(\theta_{\alpha1\beta1} + \theta_{\alpha1\beta2} + \theta_{\alpha2\beta1} + \theta_{\alpha2\beta2})$, $\theta_s = 1/(\sqrt{4})(\theta_{\alpha1\beta1} + \theta_{\alpha1\beta2} - \theta_{\alpha2\beta1} - \theta_{\alpha2\beta2})$, $\theta_{V1} = 1/(\sqrt{4})(\theta_{\alpha1\beta1} - \theta_{\alpha1\beta2} + \theta_{\alpha2\beta1} - \theta_{\alpha2\beta2})$, $\theta_{V2} = 1/(\sqrt{4})(-\theta_{\alpha1\beta1} + \theta_{\alpha1\beta2} - \theta_{\alpha2\beta1} + \theta_{\alpha2\beta2})$, where $\alpha 1,2$ are spin up/down states, $\beta 1,2$ are two valley states. The Hamiltonian $\mathcal{H}_0 + \mathcal{H}_{int}$ is now composed of four separate channels with θ_ρ as the charge channel and θ_s as the spin channel. For the spin mode, the Hamiltonian takes the form $\mathcal{H}_s = \int dx \frac{\hbar v_0}{2\pi} [(\partial_x \theta_s)^2 + (\partial_x \phi_s)^2]$. The eigenstate is a collective spin wave with a propagating velocity of v_0, usually referred to as spinon. For the charge mode, the Hamiltonian becomes $\mathcal{H}_\rho = \int dx \frac{\hbar v_0}{2\pi} \left[(1 + \frac{8e^2}{4\pi\varepsilon_{eff}} \rho^2 \ln(R_s/R)) (\partial_x \theta_\rho)^2 + (\partial_x \phi_\rho)^2 \right]$. The collective charge wave, i.e. plasmon wave, has an renormalized velocity as $\frac{v_p}{v_0} = \frac{1}{g} = \sqrt{1 + \frac{8e^2}{4\pi\varepsilon_{eff}\pi\hbar v_0} \ln(\frac{R_s}{R})}$, where g is the Luttinger liquid parameter describing the interaction strength. This leads to the remarkable phenomenon of spin-charge separation. The concept of free quasiparticles carrying both charge and spin breaks down. The collective excitations, i.e. spinon and plasmon, become two separate entities moving independently with different velocities. In the spectral function, we no longer see single sharp quasiparticle peak of the Fermi liquid. Instead, there will be two sharp features characterizing the collective spin and charge excitations.

Luttinger liquid has intriguing implications for physical properties of SWNTs. In the Fermi liquid picture without interaction, the 1D density of states of metallic SWNTs with a linear band is a constant. When the interaction is considered, the electron tunneling into 1D SWNTs is suppressed at low energies because there is no available quasiparticle state in the system and the tunneling electron must excite the collective excitations. By evaluating the electron's Green's function, one can find that the tunneling density of state exhibit a power law dependence on energy as $\rho(E) \propto E^\alpha$, where *E* is the energy way from the Fermi energy, and the power index α depends on the interaction parameter g as $\alpha = (g + g^{-1} - 2)/8$. These signatures of Luttinger liquid in SWNTs have been well explored in various experiments. Electron tunneling measurements through a metal contact or a STM tip to SWNTs have confirmed the power-law suppression of tunneling density of states[41-44]. Spin-charge separation in the spectral function was also observed in angle-resolved photoemission spectroscopy (ARPES)[45].

In general 1D systems, the band dispersion is not linear anymore. The nonlinearity can qualitatively modify the nature of electron excitations[46, 47]. In a linear Luttinger liquid, where the low-energy electronic dispersion is assumed to be linear, the resulting plasmonic excitations are non-interacting. Instead, a Luttinger liquid in 1D materials with nonlinear electronic bands is expected to show strong plasmon-plasmon interactions, resulting in a strong reduction of plasmon lifetime. Semiconducting SWNTs with hyperbolic band dispersion provide a great platform to probe the nature of electron excitations in 1D systems with nonlinear dispersion. For semiconducting SWNTs with a band gap E_g and a hyperbolic dispersion $E^2 = (E_g/2)^2 + (\hbar v_0 k_F)^2$, where v_0 is the Fermi velocity in metallic nanotubes, k_F is the Fermi wavevector, the Fermi velocity is given by

$$v_F = \frac{\partial E}{\hbar \partial k_F} = \frac{\hbar {v_0}^2 k_F}{\sqrt{(E_g/2)^2 + (\hbar v_0 k_F)^2}}$$

The Fermi velocity is a constant v_0 in metallic nanotubes with linear dispersion whereas it depends on carrier density and is thus gate tunable in semiconducting nanotubes. For an individual suspended SWNT of radius R screened by a concentric metal shell of radius R_s, the linear Luttinger liquid theory predicts the Luttinger liquid interaction parameter g to be (2.1)

$$\frac{1}{g} = \frac{v_p}{v_F} = \sqrt{1 + \frac{8e^2}{4\pi\varepsilon_{eff}\pi\hbar v_F} \ln(\frac{R_s}{R})}$$

where v_p is the velocity of the collective charge excitation, i.e. plasmon velocity, v_F i (2.2) ıi velocity and ε_{eff} is the effective dielectric constant due to substrate screening. From ınfrared nano-imaging measurements on metallic SWNTs, the Luttinger liquid parameter is determined to be $g = v_0/v_p \sim 0.31$, which indicates strong coulomb repulsion between electrons in metallic SWNTs (see Chapter 3 for details). For semiconducting SWNTs, g becomes even smaller. As a result, the electron-electron interaction energy is always dominant in semiconducting SWNTs. From Eq. 2.2, the plasmon velocity can be approximated with

$$v_p = \sqrt{v_F \frac{8e^2}{4\pi\varepsilon_{eff}\pi\hbar} \ln(\frac{R_s}{R})} = \sqrt{\alpha v_F} \quad (2.3)$$

where $\alpha = \frac{8e^2}{4\pi\varepsilon_{eff}\pi\hbar} \ln(\frac{R_s}{R})$ is a constant related to the capacitance of the system under a certain dielectric environment. The Luttinger parameter can be expressed as

$$g \approx 1/\sqrt{1 + \alpha/v_F} \quad (2.4)$$

We experimentally measured the Luttinger liquid parameter in metallic SWNTs to be $g_m \approx \frac{1}{\sqrt{1+\alpha/v_0}} \approx 0.31$ and with that we can estimate $\alpha \approx 9v_0$. Combining Eq. 2.1 and Eq. 2.3, the plasmon wavelength is determined to be proportional to the square root of Fermi velocity v_F and is described as

(2.5)

$$\lambda_p = \lambda_{p0}\sqrt{\frac{v_F}{v_0}} = \lambda_{p0}\sqrt{\frac{\hbar v_0 k_F}{\sqrt{(E_g/2)^2 + (\hbar v_0 k_F)^2}}}$$

where λ_{p0} and v_0 are the plasmon wavelength and Fermi velocity in metallic nanotubes for a given frequency. With increasing carrier density n and wavevector $k_F = \frac{\pi}{4}n$, plasmon wavelength in semiconducting nanotubes will increase and progressively approach that in metallic ones.

Apart from the tunable plasmon wavelength, the nonzero curvature of the band dispersion will also modify the plasmon lifetime by inducing plasmon-plasmon interaction. This is reflected in the dynamic structure factor (DSF), which is defined as the probability per unit time to excite a density fluctuation by an external source coupled to charge density. In metallic nanotubes with a linear dispersion, the DSF takes the form $\mathrm{S}(\mathrm{q},\omega) = 2g|q|\delta(\omega - v_p q)$, which suggests the absence of intrinsic relaxation. The behavior is within the realm of the linear Luttinger liquid. In semiconducting nanotubes with a hyperbolic band dispersion, when considering the leading quadratic correction to the plasmon spectrum, the DSF is given by

$$\mathrm{S}(\mathrm{q},\omega) = 2\frac{\tilde{m}g}{|q|}\theta\left(\frac{q^2}{2\tilde{m}} - \left|\omega - v_p q\right|\right)$$

with an effective mass $\tilde{m}$. The effective mass $\tilde{m}$ depends on electron-electron interactions and it can be expressed as

$$\frac{1}{\tilde{m}} = \frac{v_p}{2g}\frac{\partial}{\partial E_F}(v_p\sqrt{g}) \tag{2.6}$$

(2.7)

The upper and lower bounds of the plasmon spectrum can be described as

$$\omega_{\pm}(q) = v_p q \pm \frac{q^2}{2\tilde{m}} \tag{2.8}$$

and the width of the plasmon spectrum is

$$\delta\omega(q) = q^2/\tilde{m} \tag{2.9}$$

The broadening $\delta\omega(q)/\omega(q)$ in the spectrum is a manifestation of the finite lifetime of the plasmon excitation. Combining Eq. 2.3, Eq. 2.4, Eq. 2.7 and Eq. 2.9, this broadening can be expressed as

$$\frac{\delta\omega(q)}{\omega(q)} = \frac{3}{4}\frac{v_p}{2g}\alpha^{1/4}{v_F}^{-1/4}\frac{\partial v_F}{\partial E_F} \tag{2.10}$$

The Fermi velocity v_F and Fermi energy E_F depend on the Fermi wavevecto ıe dependences are described by energy dispersion and Eq. 2.1, respectively. We can then determine

$$\frac{\partial v_F}{\partial E_F} = \frac{\partial v_F/\partial k_F}{\partial E_F/\partial k_F} = \frac{1}{\hbar k_F}\frac{(E_g/2)^2}{(E_g/2)^2 + (\hbar v_0 k_F)^2} \tag{2.11}$$

Combining Eq. 2.10 and Eq. 2.11, $\delta\omega(q)/\omega(q)$ is further determined to be

(2.12)

$$\frac{\delta\omega(q)}{\omega(q)} = \frac{3}{8}\left(\frac{\alpha}{v_F}\right)^{1/4}\frac{(E_g/2)^2}{(E_g/2)^2 + (\hbar v_0 k_F)^2}\frac{\omega}{v_F k_F}$$

Under our experimental environment conditions, $\alpha \approx 9v_0$ has been estimated from the plasmon measurements in metallic nanotubes. Therefore, for semiconducting nanotubes with a band gap of E_g and at an excitation energy ω, $\delta\omega(q)/\omega(q)$ is a function of k_F as

$$\frac{\delta\omega(q)}{\omega(q)} = \frac{3\sqrt{3}}{8}\left(\frac{\sqrt{(E_g/2)^2 + (\hbar v_0 k_F)^2}}{\hbar v_0 k_F}\right)^{\frac{5}{4}}\frac{(E_g/2)^2}{(E_g/2)^2 + (\hbar v_0 k_F)^2}\frac{\omega}{v_0 k_F} \qquad (2.13)$$

In summary, electron-electron interaction qualitatively alters the electron excitations in 1D SWNTs. In metallic SWNTs, plasmons are expected to be long lived with lifetime limited by electron-phonon coupling in the system. The plasmon velocity is greatly enhanced compared to Fermi velocity which is directly controlled by the Luttinger liquid parameter g. In addition, there is suppression of electron tunneling into the 1D system in the form of a power-law dependence with the power index governed by the same Luttinger liquid parameter g. In strong contrast, plasmon lifetime in semiconducting SWNTs is expected to depend sensitively on the nonzero band curvature. For semiconducting nanotubes with a band gap E_g and at an excitation energy ω, both the plasmon wavelength λ_p and plasmon quality factor $Q = \omega(q)/\delta\omega(q)$ depend sensitively on the Fermi wavevector k_F. Under our experimental conditions, the dependence on k_F can be expressed as:

$$\lambda_p = \lambda_{p0}\sqrt{\frac{\hbar v_0 k_F}{\sqrt{(E_g/2)^2 + (\hbar v_0 k_F)^2}}} \qquad (2.14)$$

$$Q = \frac{\omega(q)}{\delta\omega(q)} = \frac{8}{3\sqrt{3}}\left(\frac{\hbar v_0 k_F}{\sqrt{(E_g/2)^2 + (\hbar v_0 k_F)^2}}\right)^{\frac{5}{4}}\frac{(E_g/2)^2 + (\hbar v_0 k_F)^2}{(E_g/2)^2}\frac{v_0 k_F}{\omega} \qquad (2.15)$$

The signatures of the Luttinger liquid in both metallic and semiconducting SWNTs described by the picture can be tested with a combined interrogation of infrared nanoimaging and electronic transport. The experimental results and the comparison with theoretical model will be discussed in detail in Chapters 3, 4, 5.

2.3 Infrared Scanning Near-field Optical Microscope

Conventional far-field spectroscopy is a versatile and powerful tool to investigate a wealth of properties of matter through light-matter interaction at different energy, length and time scales. However, the achievable resolution of this far-field technique is usually around half of the excitation wavelength owing to the Abbe's diffraction limit. Evanescent field near the surface of objects drops off rapidly away from the surface and carries the high frequency spatial information.

Utilizing this near field can potentially leads to an optical probe beyond the diffraction limit. A realistic implementation of this idea yields scanning near-field optical microscope (SNOM). Progress in SNOM techniques has led to the developments of different instrumental configurations to interrogate and image materials with nanoscale resolution, good signal to noise ratio and a broad spectrum from visible to teraHertz[15, 48]. The modality we employ to probe plasmons in SWNTs is a scattering-type SNOM working at infrared frequencies (IR-SNOM).

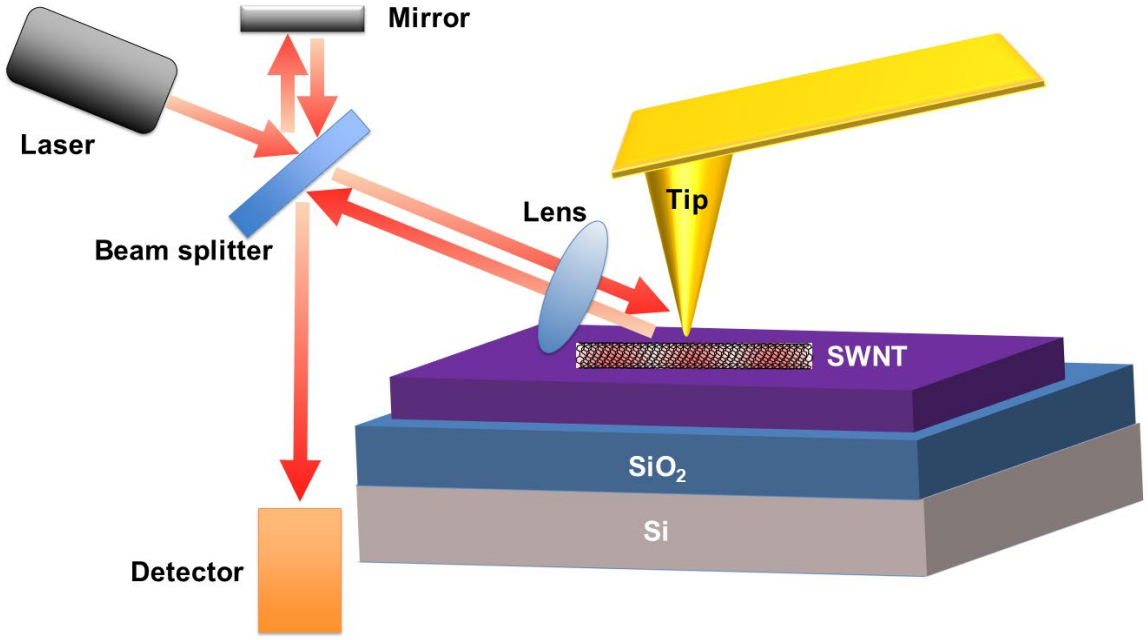

Figure 2.5 Schematic of scattering-type infrared scanning near-field optical microscope.

Figure 2.5 illustrates the schematic of the scattering-type IR-SNOM. The infrared nanoimaging technique is based on a tapping mode atomic force microscope (AFM). For infrared nanoimaging, an infrared beam is focused onto the apex of the metallic AFM tip by an aspherical ZnSe lens or a gold-coated parabolic mirror. The infrared source can be a CO_2 laser with wavelength 10.6 μm for a single wavelength measurement or a quantum cascade laser with tunable wavelength from 11.1 to 9.5 μm for a spectrally resolved measurement. The light elastically scattered from the tip apex is captured by a mercury cadmium telluride (MCT) detector in the far field. The total scattered signal measured by the detector is $I_{det} \propto (E_{nf} + E_{bg})(E_{nf}{}^{*} + E_{bg}{}^{*}) = E_{nf}{}^{2} + E_{bg}{}^{2} + 2|E_{nf}||E_{bg}|\cos(\Delta\emptyset)$, where E_{nf} is the local near-field signal, E_{bg} is the background signal and $\Delta\emptyset$ is the phase difference between the two electric field. In many cases, $|E_{nf}| \ll |E_{bg}|$ and the background signal dominates over near field signal. To extract the near-field information, the AFM tip is tapped at a frequency of $\Omega \sim 240$ kHz and an amplitude ~80 nm, respectively. The near-field signal decreases significantly when tip is retracted a short distance of ~ 80 nm but the background change very little. The detector signal is demodulated at a frequency 3Ω by a lock-in amplifier to suppress the background scattering from the tip shaft and sample. The demodulated signal becomes $I_{demo} \propto |E_{nf}||E_{bg}|\cos(\Delta\emptyset)$, because $E_{nf}{}^{2}$ is negligibly small and $E_{bg}{}^{2}$ is not modulated. By recording the demodulated signal while scanning the sample, near-field images are obtained simultaneously with the topography. The demodulated signal contains the

local near field but still includes a constant component of background scattering as interference, resulting in a convolution of near-field amplitude and phase. This scheme is commonly referred to as self-homodyne detection. To extract both the phase and amplitude of near field, a pseudo-heterodyne detection is required. This scheme utilizes a Michelson interferometer, with the sample positioned in one arm and a vibrating mirror placed in the other arm as shown in Figure 2.5. A combination of demodulation and varying phase of the reference beam from the vibrating mirror allows extraction of both near-field amplitude and phase. However, mirror instability or drift in a pseudo-heterodyne scheme may contribute to larger noise and lower signal-to-noise ratios compared to a self-homodyne scheme.

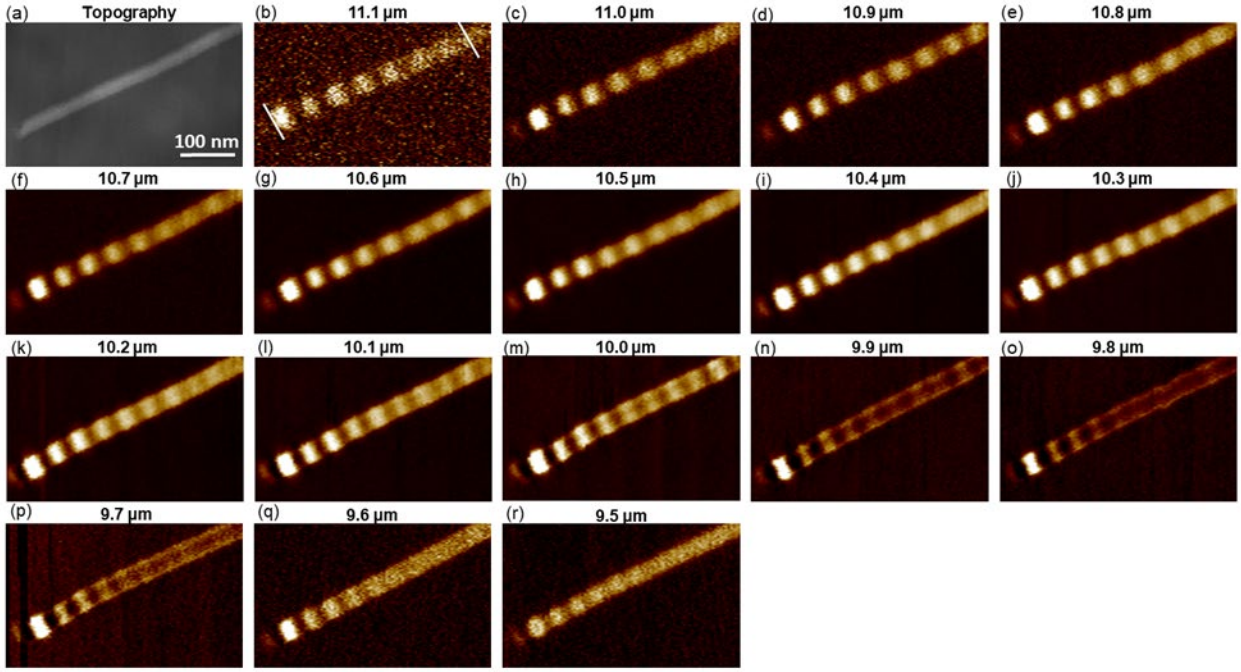

Figure 2.6 Spectrally resolved infrared nano-imaging of a long metallic carbon nanotube. (a) Topography of a representative metallic carbon nanotube. (b) to (r) Corresponding near-field response images at excitation wavelengths from 11.1 to 9.5 µm. Plasmon wavelength equal to twice the oscillation period shortens as excitation wavelength is decreased from 11.1 to 9.5 µm.

Figure 2.6 shows a spectrally resolved infrared nanoimaging of a representative metallic SWNT. In the topography image (Figure 2.6a), there is no variation along the SWNT whereas there are prominent oscillations along the SWNT in the near-field images (Figures 2.6b to 2.6r). These oscillations correspond to the interference of tip-launched and end-reflected plasmon waves. To achieve best signal-to-noise near-field signal from the tiny SWNTs, we utilize the self-homodyne scheme.

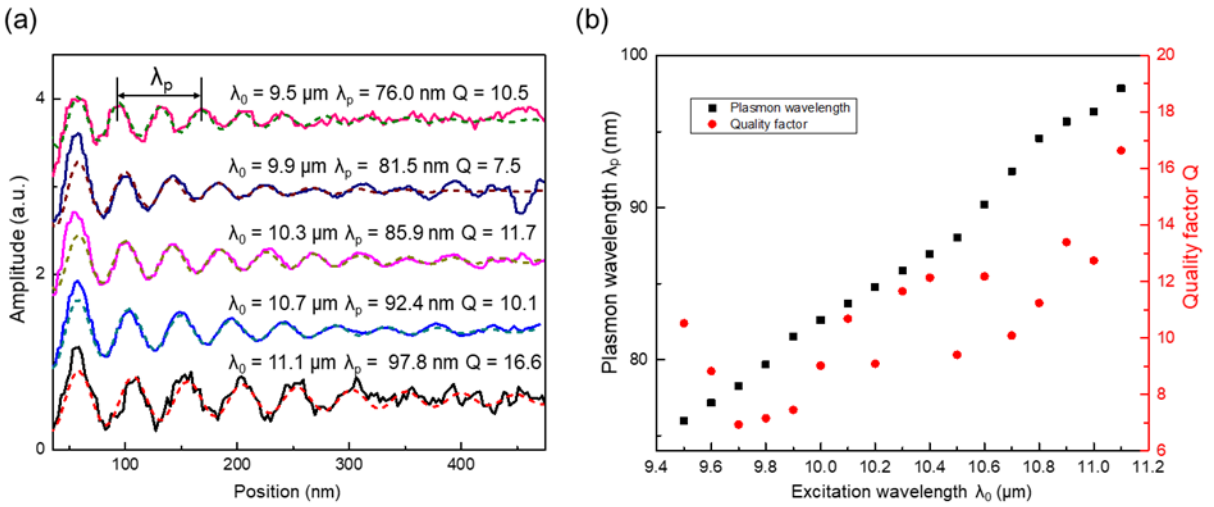

Figure 2.7 Line profiles of near-field images in Figure 2.6 and plasmon analysis. (a) Near-field response line profiles and extraction of plasmon wavelength λ_p and quality factor Q. Solid lines represent the near-field profiles taken along SWNTs between the two white bars in the near-field images in Figure 2.6 at excitation wavelengths 11.1, 10.7, 10.3, 9.9, 9.5 μm. Plasmon wavelength equal to twice the oscillation period in the near-field images is marked by the black double arrow. We can extract both the plasmon wavelength λ_P and quality factor Q as a function of wavelength by fitting the line profiles with a damped oscillator form $e^{-2\pi x/(Q\cdot\lambda_P)}\sin\left((4\pi x)/\lambda_p\right)$ from the nanotube end. The fitting curves for each wavelength are shown in dashed lines. (b) Extracted plasmon wavelength and quality factor as a function of excitation wavelength from 11.1 to 9.5 μm.

Figure 2.7 shows plasmon analysis for the measured wavelength range from 11.1 to 9.5 μm. Solid lines in Figure 2.7a represent the near-field profiles taken along SWNTs between the two white bars in the near-field images in Figure 2.6 at excitation wavelengths 11.1, 10.7, 10.3, 9.9, 9.5 μm. Plasmon wavelength equal to twice the oscillation period in the near-field images is marked by the black double arrow. The line profiles in Figure 2.6a reveal how the plasmon wave is damped as it propagates. We can extract both the plasmon wavelength λ_P and quality factor Q as a function of wavelength by fitting the line profiles with a damped oscillator form $e^{-2\pi x/(Q\cdot\lambda_P)}\sin\left((4\pi x)/\lambda_p\right)$ from the nanotube end. The fitting curves for each wavelength are shown in dashed lines. Figure 2.7b shows the extracted plasmon wavelength and quality factor as a function of excitation wavelength from 11.1 to 9.5 μm. The plasmon wavelength shortens almost in a linear fashion as excitation wavelength is decreased from 11.1 to 9.5 μm, which is characteristic of 1D plasmons. The plasmon quality factor also depends on excitation wavelength, which may be associated with wavelength-dependent dielectric constants of the h-BN substrate.

Chapter 3 – Logarithm Diameter Scaling and Carrier Density Independence of One-dimensional Luttinger Liquid Plasmon

3.1 Introduction and Background

Interacting electrons in three- and two-dimensional metals are well described by quasi-particles within the Fermi liquid theory. In one dimension (1D), however, Coulomb interactions qualitatively alter the electron behaviors and lead to a new type of correlated electron system — the Luttinger liquid. Many novel phenomena can emerge in the Luttinger liquid, such as charge-spin separation, where the collective charge excitation (plasmon) and collective spin excitation (spinon) propagate independently at different velocities. Metallic single walled carbon nanotubes (SWNTs) provide an ideal model system to study the Luttinger liquid behavior due to the strong electron quantum confinement in the lateral dimensions and the presence of different metallic nanotubes of varying chiralities and diameters. It has been predicted that the electron-electron interaction strength, and therefore the Luttinger liquid plasmon excitation, has a logarithm dependence on the nanotube diameter[37-40]. In addition, the electron density in SWNTs can be controlled conveniently through electrostatic gating in a field-effect transistor device configuration. In spite of intense interests in the Luttinger liquid physics in SWNTs, the dependence of Luttinger liquid behavior on the nanotube diameter and the carrier density has never been explored experimentally. The abundance of ultraclean and long SWNTs on hexagonal boron nitride (h-BN) flakes (Chapter 2.1) and the improved performance of scattering-type IR-SNOM (Chapter 2.3) enable the visualization of plasmons in individual SWNTs with great signal to noise ratio, which makes possible the quantitative analysis of its behaviors.

3.2 Logarithm Diameter Scaling of Plasmons in Metallic SWNTs

Ultraclean SWNTs were directly grown on exfoliated h-BN flakes on silicon substrate with 285 nm oxide layers by chemical vapor deposition (CVD). Different species of SWNTs on h-BN substrates can be grown by such CVD processes. Atomic force microscopy (AFM) characterization of the SWNTs shows that SWNTs with diameters ranging from 0.7 nm to 2.0 nm exist in our samples. Plasmons in these nanotubes were probed by means of IR-SNOM at an excitation wavelength of 10.6 μm.

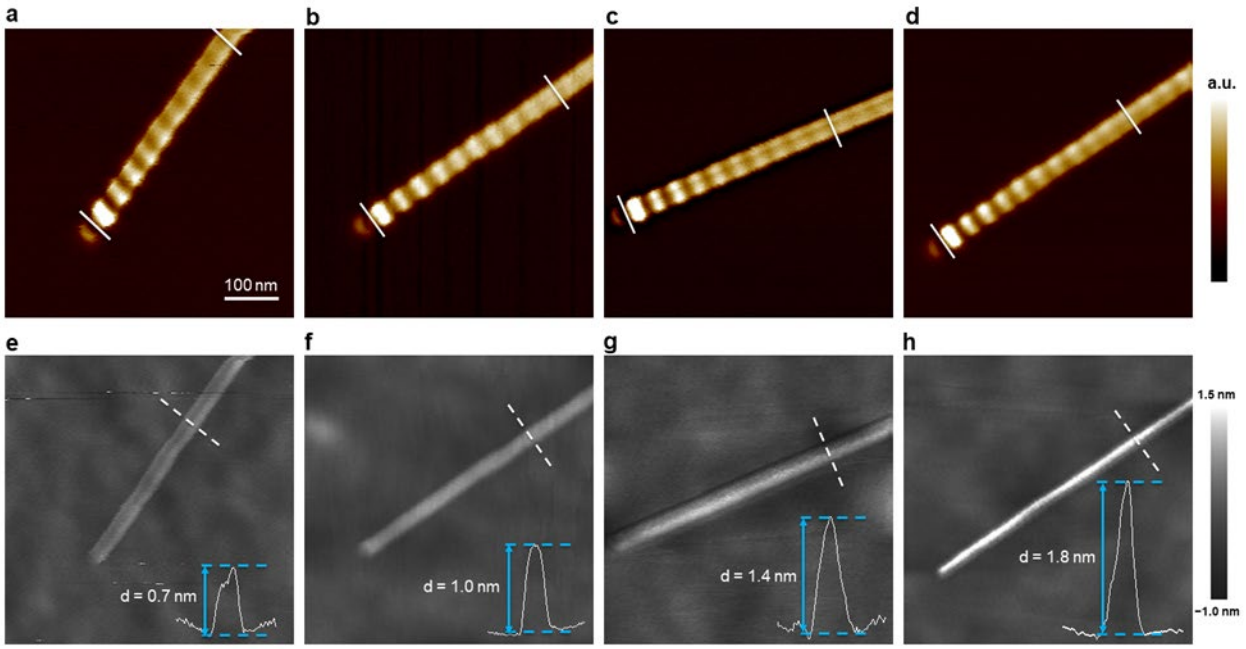

Figure 3.1 Correlation of near-field optical response and nanotube size in various metallic SWNTs. (a) to (d) Near-field images of representative metallic SWNTs with varying diameters. Prominent oscillation peaks persist in various metallic SWNTs. (e) to (h) Corresponding topography images of the metallic SWNTs. Insets are height profiles across SWNTs taken along the white dashed lines. Diameters are determined to be 0.7 nm, 1.0 nm, 1.4 nm, 1.8 nm, respectively. Note that all images share the same scale bar as shown in (a) for direct comparison.

Figures 3.1a-d display infrared nano-imaging results of representative metallic SWNTs with varying diameters. It's evident that prominent oscillations persist in these different metallic SWNTs. The oscillation peaks in the near-field images correspond to the constructive interference between the plasmon wave excited by the tip and that reflected by the end of the nanotube. The plasmon wavelength λ_p thus can be simply determined as twice the separation between adjacent peaks in the near-field images. Plasmon velocity can then be readily acquired as $v_p = \lambda_p f$ where f ~ 28.3 THz is the frequency of the excitation light. The diameters of the SWNTs can be determined from the topography images, which are obtained simultaneously with near-field images during the scanning. Figures 3.1e-h show the topography images corresponding to the near-field images Figures 3.1a-d. Insets are the line profiles across SWNTs taken along the white dashed lines. From the height profiles, diameters of SWNTs in Figures 3.1e-h are determined to be 0.7 nm, 1.0 nm, 1.4 nm, 1.8 nm, respectively. Correlation of the near-field optical response and the structural property enables a systematic revelation of the size dependence of the plasmon velocity.

To better present the measured data, we plot in Figure 3.2a (solid lines) the near-field response profiles taken along the nanotubes between two white bars in the near-field images Figures 3.1a-d. Plasmon wavelength equal to twice the oscillation period is marked by the black double arrow. From the near-field response profiles, it's clearly seen that the plasmon wavelength decreases as diameter increases[49, 50]. This trend is in sharp contrast to conventional 1D metal nanoshells

with electrons described by the Drude model. Plasmon wavelength in a 1D metal nanoshell under the Drude model has been theoretically predicted to increase almost in a linear fashion as diameter increases. Experimentally, plasmon wavelength in 1D metallic nanowires has been observed to increase dramatically with increasing diameter[51]. The different trend highlights the unique quantum nature of 1D plasmons in metallic SWNTs.

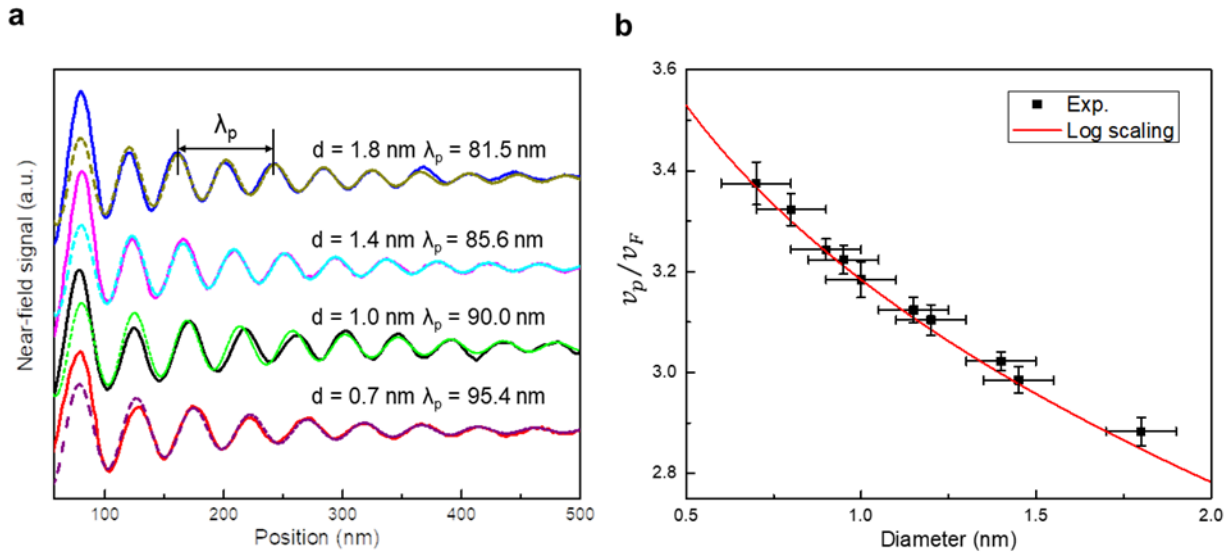

Figure 3.2 Logarithmic diameter dependence of the plasmon velocity. (a) Near-field response line profiles and extraction of plasmon wavelength. Solid lines represent the near-field profiles taken along SWNTs between two white bars in the near-field images Figures 3.1a-d. Plasmon wavelength equal to twice the oscillation period in the near-field images is marked by the black double arrow. We can extract both the plasmon wavelength λ_P and quality factor Q as a function of diameter by fitting the line profiles with a damped oscillator form $e^{-2\pi x/(Q\cdot\lambda_P)}\sin\left((4\pi x)/\lambda_p\right)$ from the nanotube end. The fitting curves for each diameter are shown in dashed lines. (b) The experimental data (black squares) agree excellently with a logarithmic diameter dependence (red curve). Horizontal errors bars reflect the precision with which diameter can be determined from the AFM topography measurements. Vertical error bars indicate a 95% confidence interval determined from the curve fitting of the near-field profiles with a damped oscillator form.

Near-field line profiles along the nanotubes represented by the solid lines in Figure 3.2a reveal how the plasmon wave gets damped as it propagates. For a quantitative study, we can extract both the plasmon wavelength λ_P and quality factor Q as a function of diameter by fitting the line profiles with a damped oscillator form $e^{-2\pi x/(Q\cdot\lambda_P)}\sin\left((4\pi x)/\lambda_p\right)$ from the nanotube end. The fitting curves for each diameter are shown in dashed lines in Figure 3.2a. In our measured diameter range from 0.7 nm to 1.8 nm, plasmon wavelength λ_p is determined to be from 95.4 nm to 81.5 nm with a 95% confidence interval of ~ 2.0 nm from the fitting. Plasmon velocity are then easily calculated as $v_p = \lambda_p f \sim 2.7 \times 10^6\, m/s$ to $2.3 \times 10^6\, m/s$ where f ~ 28.3 THz is the frequency of the excitation light. In metallic SWNTs, $v_F \sim 0.8 \times 10^6\, m/s$ is the Fermi velocity. Figure 3.2b summarizes the dependence of plasmon velocity in terms of v_p/v_F on diameter for metallic SWNTs with an ample range of diameters including those shown in Figure 3.1. Horizontal error bars reflect the precision with which diameter can be determined from the AFM topography measurement. Vertical error bars indicate the uncertainty from the fitting. These data points can

be explicitly compared with predictions by the Luttinger liquid theory. For an individual SWNT of diameter d residing on a substrate, the Luttinger liquid theory predicts the Luttinger liquid interaction parameter g to be

$$\frac{1}{g} = \frac{v_p}{v_F} = \sqrt{1 + \frac{8e^2}{4\pi\varepsilon_{eff}\pi\hbar v_F} \mathrm{In}(\frac{\lambda_p}{\pi d})} \quad (3.1)$$

where v_p is the velocity of the collective charge mode, i.e. plasmon velocity, $v_F \sim 0.8 \times 10^6\, m/s$ is the Fermi velocity, ε_{eff} is the effective dielectric constant due to substrate screening and the plasmon wavelength λ_p determines the cutoff length of the Coulomb interactions and acts as the screening length. The second term arises from the long-range Coulomb interaction which goes as $q^2/2C$, where $C \sim 2\pi\varepsilon_{eff}/In(\frac{\lambda_p}{\pi d})$ is the capacitance per unit length. Therefore, the electron-electron interaction in the Luttinger liquid exhibits a logarithm scaling with the nanotube diameter. In our measured diameter range from 0.7 nm to 1.8 nm, plasmon velocity v_p has been obtained to be from $2.7 \times 10^6\, m/s$ to $2.3 \times 10^6\, m/s$. The Luttinger liquid parameter g describing the interaction in SWNTs can then also be determined to be $g = v_F/v_p \sim 0.29$ to 0.34, which indicates strong Coulomb repulsion between electrons in all studied metallic SWNTs. Because interaction energy dominates in studied metallic SWNTs, we can safely neglect the first term in equation (3.1). The plasmon velocity thus becomes $v_p = \sqrt{\frac{8e^2 v_F}{4\pi\varepsilon_{eff}\pi\hbar} \mathrm{In}(\frac{\lambda_p}{\pi d})} \propto \sqrt{\mathrm{In}(\frac{\lambda_p}{\pi d})}$. Note that plasmon wavelength λ_p also varies with diameter but the change (~ 16%) is much smaller compared to the change in diameter (more than 100%). This predicted logarithmic dependence on the diameter is depicted in Figure 3.2b by the red curve, which shows excellent agreement with the experimental results represented by the black squares.

3.3 Carrier Density Independence of Plasmons in Metallic SWNTs

We next systematically investigate the dependence of plasmon behaviors on carrier density in metallic SWNTs. Figure 3.3a illustrates the schematic of infrared nano-imaging of SWNTs with carrier density controlled by applying a back gate voltage V_g. In order to observe the prominent Luttinger liquid plasmon oscillations by our infrared nano-imaging technique, we utilize the nanotube end as a well-defined reflector to create the standing plasmon wave. The metallic nanotubes are sitting on h-BN substrates and their charge neutral points tend to be close to a zero gate voltage. When gate voltage V_g is varied from -20 to 30 V, the carrier type in carbon nanotubes changes from hole doping to charge neutrality and then to electron doping. The near-field optical responses at these different gate voltages are shown in Figures 3.3c-h. It's evident that prominent plasmons are excited at different gate voltages or carrier densities. Figure 3.4 displays the line profiles along the carbon nanotube in the near-field images Figures 3.3c-h. Vertical dashed lines serve as guide to the eye. When the gate voltage is varied from -20 V to 30 V, the period of plasmon standing wave remains unchanged. There are small changes in the exact amplitude of the near-field signal, which may arise from the slightly different AFM scanning condition due to the presence of the back gate voltage. In contrast, differences in the plasmon oscillation periods are

clearly observable after several cycles in the nanotube diameter dependence as shown in Figure 3.2a.

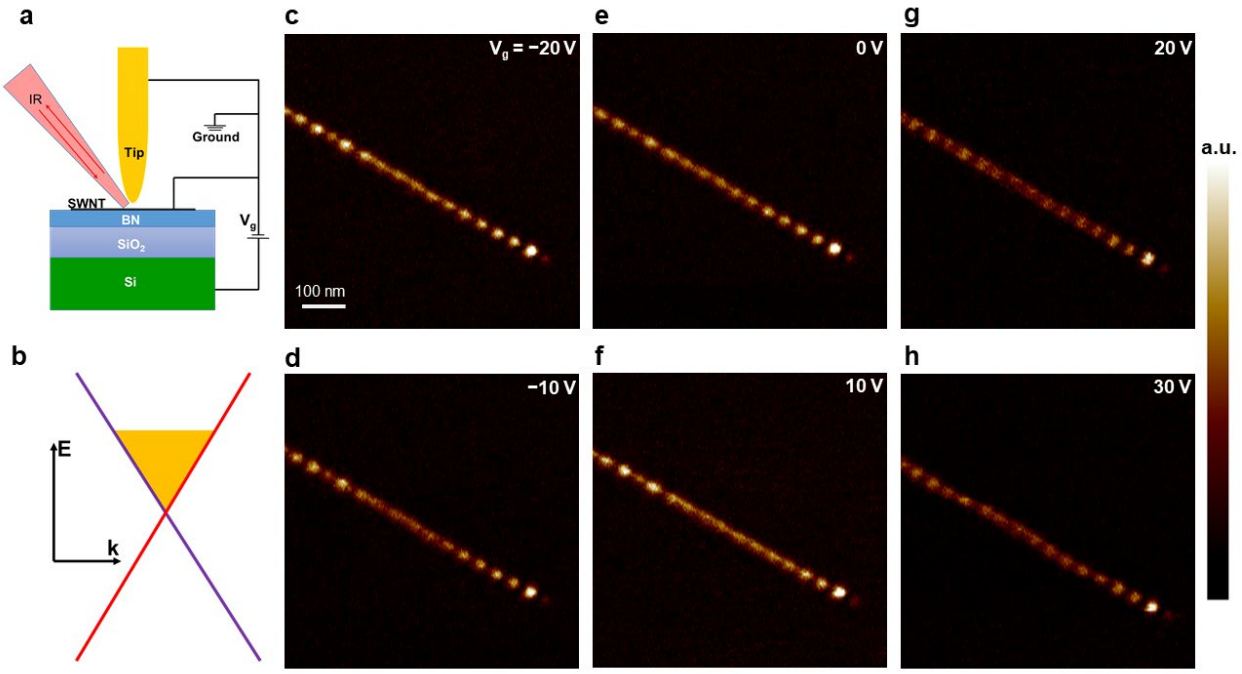

Figure 3.3 Infrared nano-imaging of an electrostatically gated metallic nanotube. (a) Schematic of infrared nano-imaging of a nanotube with carrier density controlled by applying a back gate voltage V_g. (b) Illustrative band diagram of metallic SWNTs. With this linear dispersion and 1D nature, the Fermi velocity as well as the density of state remains a constant independent on the Fermi energy. (c) to (h) Near-field responses of a metallic SWNT at different gate voltages. From (c) to (h), the gate voltage is varied from -20 to 30 V and the nanotube changes from hole doping to charge neutrality and then to electron doping. Plasmon wavelength determined as twice the oscillation period and plasmon amplitude reflected in the near-field intensity are largely independent on gate voltages.

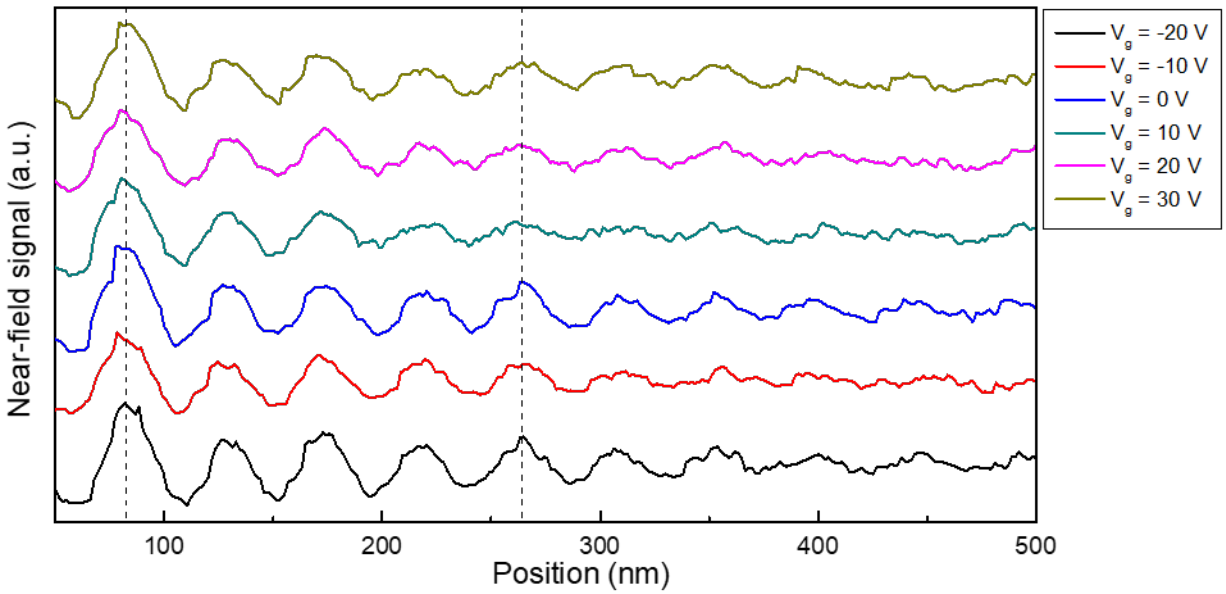

Figure 3.4 Line profiles along the carbon nanotube in the near-field images Figures 3.3c-h. Vertical dashed lines serve as guide to the eye. When the gate voltage is varied from -20 to 30 V, the period of plasmon standing wave remains exactly the same. There are small changes in the exact amplitude of the near-field signal, which may arise from the slightly different AFM scanning condition due to the presence of the back gate voltage. In contrast, differences in the plasmon oscillation periods are clearly observable after several cycles in the nanotube diameter dependence as shown in Figure 3.2a.

Note that even at around charge neutrality (Figures 3.3d-e, Figure 3.4), the plasmon oscillations still exist and behave the same way as the highly doped ones (Figure 3.3h, Figure 3.4). This counter-intuitive carrier density independent plasmon behavior in metallic nanotubes stands in striking contrast to conventional plasmons. In conventional 2D or 3D systems, plasmon wavelength and amplitude are closely associated with the carrier density for a given frequency. For instance, plasmons in graphene have been demonstrated to be continuously tuned by changing gate voltages[52-54]. This peculiar plasmon behavior in metallic SWNTs arises from its unique 1D massless Dirac electrons. Figure 3.3b illustrates the band diagram of a metallic SWNT which features a linear dispersion. With this linear dispersion and 1D nature, the Fermi velocity as well as the density of state remains a constant independent on the Fermi energy. Quantum excitations including the plasmons of an electron liquid close to the Fermi energy are determined by the Fermi velocity and density of state rather than the total carrier concentration. The plasmon excitation in metallic SWNTs therefore shows no dependence on carrier density. The peculiar behavior is also explicitly evident in the prediction by the Luttinger liquid theory as shown in equation (3.1). It's clear from the prediction that plasmon wavelength is a function of only the Fermi velocity for a given nanotube under certain dielectric environment. Because Fermi velocity is a constant in metallic SWNTs with linear dispersion, the plasmon behaviors will remain exactly the same regardless of carrier density.

3.4 Summary and Discussion

In summary, we report the observation of peculiar Luttinger liquid plasmon signatures in metallic SWNTs, including an intriguing logarithmic dependence of plasmon wavelength on diameter and a counter-intuitive independence on carrier density. These signatures stand in stark contrast to conventional plasmons and are prime examples of quantum size effects in nanoscale plasmonic systems. Our findings not only provide fundamental insight into Luttinger liquid physics in 1D systems but also pave the way for promising nanophotonic applications based on SWNTs.

We would like to remark that Random phase approximation (RPA) theory will predict the same plasmon dispersion behaviors as those obtained by the Luttinger liquid theory[55]. Therefore, the measurement of plasmons cannot provide a definitive proof of the Luttinger liquid by itself. To unambiguously demonstrate the Luttinger liquid behavior, one can combine the study of nanotube plasmon (which can determine the Luttinger liquid parameter g) with electrical tunneling study that has a power low scaling with index determined by g. This correlative study will be discussed in Chapter 4. Our study in this chapter serves to further test the specific predictions of the Luttinger liquid theory, including the logarithmic dependence of plasmon velocity and the independence of carrier concentration. Our study establishes experimentally the unusual phenomenology that plasmon excitation in 1D quantum systems can be completely independent on charge carrier, and it provides an experimental determination of the Luttinger liquid parameter g and its scaling with the nanotube diameter.

Chapter 4 – Correlation of Electron Tunneling and Plasmon Propagation in a Luttinger Liquid

4.1 Introduction and Background

In Chapter 3, we have demonstrated that infrared nanoimaging of plasmons in metallic SWNTs provides an experimental determination of the Luttinger liquid parameter g and its logarithm scaling with the nanotube diameter. Both the power index of the correlation function and the velocity ratio between charge and spin modes are uniquely defined by a single Luttinger liquid interaction parameter g. To unambiguously demonstrate the Luttinger liquid behavior, one can combine the study of nanotube plasmon (which can determine the Luttinger liquid parameter g) with electrical tunneling study that has a power low scaling with index determined by g. Because the massless Dirac electrons exhibit linear energy dispersion up to 1 eV, the Luttinger liquid behavior in metallic SWNTs is rigorous for temperatures up to thousands of Kevin. Previously, Luttinger liquid behavior in SWNTs has been mostly studied through electrical tunneling measurements in nanotubes and their ropes, which shows power-law like tunneling probability[41-43, 56, 57]. However, that interpretation is plagued by the unknown structure of the SWNT-metal contact tunnel junction, and the unknown Luttinger parameter of nanotube ropes. Two crossed metallic SWNTs provide an attractive realization of Luttinger liquid tunnel junction[56, 58]. Here we investigate SWNT cross junctions with high quality that are directly grown on hexagonal boron nitride (hBN) flakes as shown in Figure 4.1.

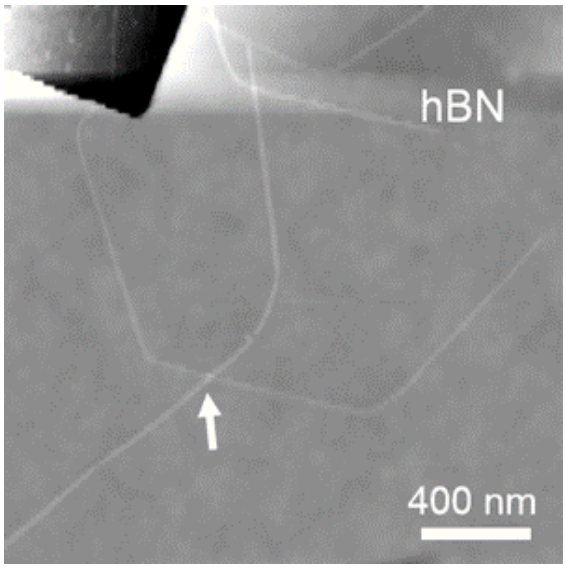

Figure 4.1 AFM topography image of a representative SWNT cross junction sample on h-BN. The SWNT cross junction is composed of two individual SWNTs with a point contact (indicated by the arrow).

The SWNT cross junction compare favorably with SWNT/metal junction in two ways. On one hand, the complicated mechanism at the tunneling process from SWNT to metal can be

circumvented when tunneling between SWNTs dominate. On the other hand, the suppression of tunneling density of states exist in both SWNTs, resulting in a larger power index for the power-law suppression of the tunneling conductance. As discussed in Chapter 2.2, the tunneling density of state of a Luttinger liquid is suppressed as a power-law function of energy, $\rho(E) \propto E^{\alpha}$, where E is the energy way from the Fermi energy, and the power index α depends on the interaction parameter g as $\alpha = (g + g^{-1} - 2)/8$. By applying a bias between two Luttinger liquids with respective Luttinger parameter g1 and g2 and corresponding power index $\alpha 1$ and $\alpha 2$, the tunneling current I between the two Luttinger liquids at a bias V is given by

$$I \propto \int_0^V (x)^{\alpha 1}(V-x)^{\alpha 2} dx = \frac{\Gamma(\alpha 1+1)\Gamma(\alpha 2+1)}{\Gamma(\alpha 1+\alpha 2+1)} V^{\alpha 1+\alpha 2+1}$$

The differential tunneling conductance dI/dV should vary with the bias as $\mathrm{d}I/\mathrm{d}V \propto V^{\alpha 1+\alpha 2}$, where $\alpha 1(2) = (g1(2) + g1,(2)^{-1} - 2)/8$. For a SWNT cross junction, Luttinger parameter g for both SWNTs can be determined from plasmon propagation. If both SWNTs have the same Luttinger liquid parameter g, then the power index $\alpha = \alpha 1 + \alpha 2 = (g + g^{-1} - 2)/4$. The power index can be obtained through the differential conductance measurement.

4.2 Distinguish Metallic and Semiconducting SWNTs by Infrared Nanoimaging

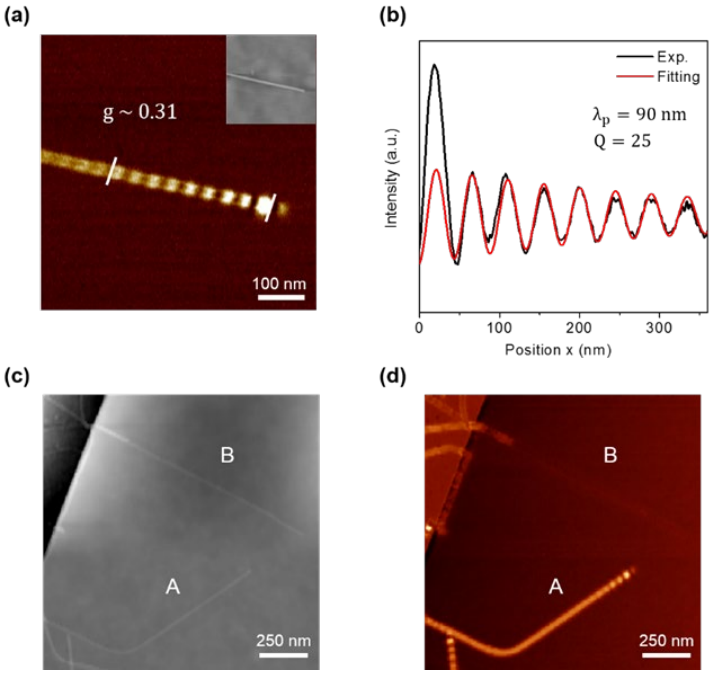

Figure 4.2. Near-field optical nanoscopy characterizations on SWNTs on h-BN. (a) Near-field optical nanoscopy image of an individual metallic SWNT with a diameter of ~ 1 nm. Inset shows the corresponding topography image that is simultaneously recorded. (b) Experimental intensity profile (in black) of Luttinger liquid plamon oscillations and the corresponding theoretical fitting (in red) with the damped oscillator form $e^{-2\pi x/(Q\cdot\lambda_P)} \sin\left((4\pi x)/\lambda_p\right)$ along the tube axis between two bars in (a), where λ_p is the plasmon

wavelength and Q is the quality factor. Luttinger parameter g ~ 0.31 (shown in (a)) is directly obtained from the measured plasmon wavelength λ_p. (c) AFM topography image of an individual metallic SWNT (tube A) and an individual semiconducting SWNT (tube B) on hBN with similar diameters ~ 0.8 nm. (d) The corresponding near-field optical nanoscopy image of (c). The metallic SWNT (tube A) exhibits prominent Luttinger liquid plasmon oscillations, whereas the semiconducting SWNT (tube B) barely shows any near-field optical response.

Infrared nanoimaging of SWNTs on h-BN flakes provides unambiguous distinguishment between metallic and semiconducting SWNTs, and directly yields an experimental determination of Luttinger parameter g of the SWNT. We observe well-defined Luttinger liquid plasmon oscillations with high quality factor in individual metallic SWNTs on h-BN as shown in Figure 4.2a. The inset of Figure 4.2a is an AFM topography image of the same nanotube (diameter ~ 1 nm) which is simultaneously recorded. Oscillation peaks in Figure 4.2a correspond to the constructive interference between the excited plasmons under the tip and the reflected plasmon waves by the tube end. Therefore, the plasmon wavelength λ_p is simply two times the oscillation period of the near-field signal. We determine λ_p and quality factor Q by fitting the experimental plasmon oscillation profile in Figure 4.2a (between two white bars) with the damped oscillator form $e^{-2\pi x/(Q\cdot\lambda_p)}\sin\left((4\pi x)/\lambda_p\right)$. The results are presented in Figure 4.2b. The fitting can reproduce the experimental data very well, which yields $\lambda_p = 90\,\mathrm{nm}$ and $Q = 25$. Very importantly, the observation of high quality Luttinger liquid plasmons by near-field optical nanoscopy enables us to directly measure the Luttinger parameter g without relying on other parameters. With known λ_p, the plasmon velocity v_p is determined to be $v_p \sim 2.55 \times 10^6\,\mathrm{m/s}$ by using $v_p = c \times \lambda_p/\lambda_0$, where c is the speed of light and λ_0 is the wavelength of the infrared probe light (10.6 μm). We can then directly obtain the Luttinger parameter g ~ 0.31 for this metallic SWNT by using $1/g = v_p/v_F$ with Fermi velocity $v_F \sim 8 \times 10^5\,\mathrm{m/s}$. Note that we observe consistent Luttinger liquid plasmon oscillations and Luttinger parameters in all of our investigated individual metallic SWNT samples on h-BN.

Luttinger liquid behaviors in metallic SWNTs and semiconducting SWNTs are predicted to be very different[47]. We employ near-field optical nanoscopy to identify metallic SWNTs from semiconducting species in order to find SWNT cross junctions composed of two metallic SWNTs. We observe dramatically distinct near-field optical response between individual metallic and semiconducting SWNTs. As an example, Figures 4.2c and 4.2d present the topography image and the corresponding near-field optical nanoscopy image of two individual SWNTs on h-BN, respectively; the two nanotubes (labeled as A and B) have similar diameters ~ 0.8 nm. Nanotube A in Figure 4.2d exhibits prominent Luttinger liquid plasmon oscillations that are similar to those in Figure 4.2a, whereas nanotube B barely shows any near-field optical contrast. Nanotube A that exhibits Luttinger liquid plasmon oscillations corresponds to a metallic SWNT with zero band gap, and nanotube B which is dark is a semiconducting SWNT with a finite band gap that is much larger than the infrared laser excitation energy. A detailed study of plasmons in semiconducting SWNTs will be discussed in Chapter 5. We further confirm this by complementary electrical transport measurements as shown in Figure 4.3. Tube A and B respectively exhibit a weak (on/off < 5) and strong gate dependence (on/off > 1000) in conductance at room temperature, characteristics of metallic and semiconducting nanotubes.

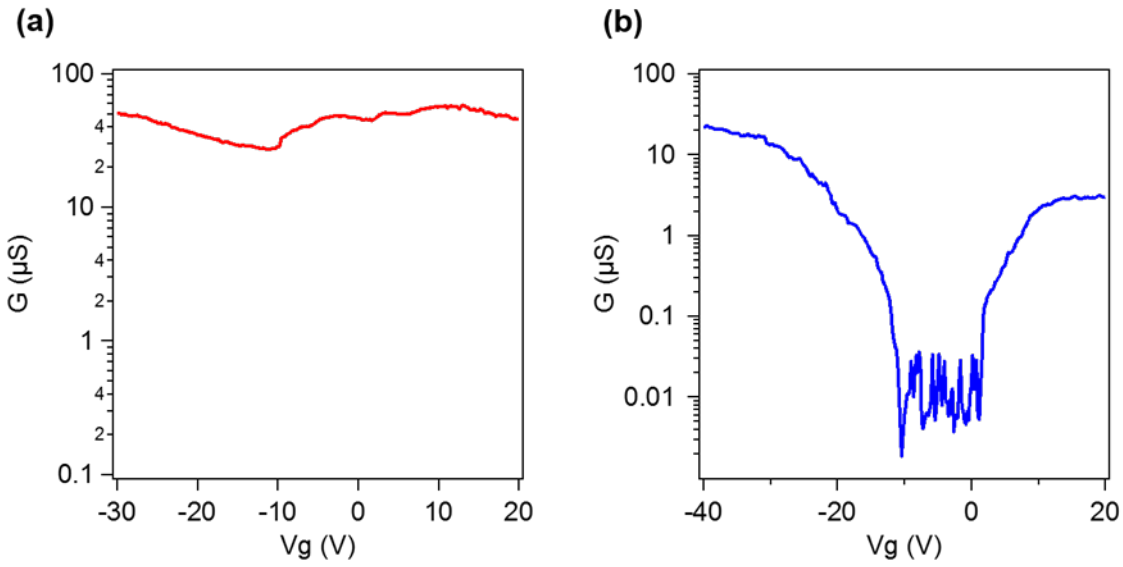

Figure 4.3 Transport data on individual metallic and semiconducting SWNTs characterized by near-field optical nanoscopy. (a) Transport data of an individual metallic SWNT (tube A in Figure 4.2c) with weak dependence on backgate voltage (on/off < 5). (b) Transport data of an individual semiconducting SWNT (tube B in Figure 4.2c) with strong dependence on backgate voltage (on/off > 1000). Measurements in (a) and (b) are carried out at room temperature in vacuum by standard lock-in technique.

4.3 Correlation of Electron Tunneling and Plasmon Propagation at a SWNT Junction

Two metallic SWNT cross junctions (i.e. crossed Luttinger liquid junctions) characterized by near-field optical nanoscopy are shown in Figure 4.4 and Figure 4.5. Clear observation of Luttinger liquid plasmons in each of the constituent SWNTs provides an unambiguous identification of metallic SWNTs in these junctions. In the following, we will turn our focus to the experimental determination of Luttinger parameters g that are independently measured from two different physical properties, i.e. electron tunneling density of states and plasmon velocity in crossed Luttinger liquid junctions.

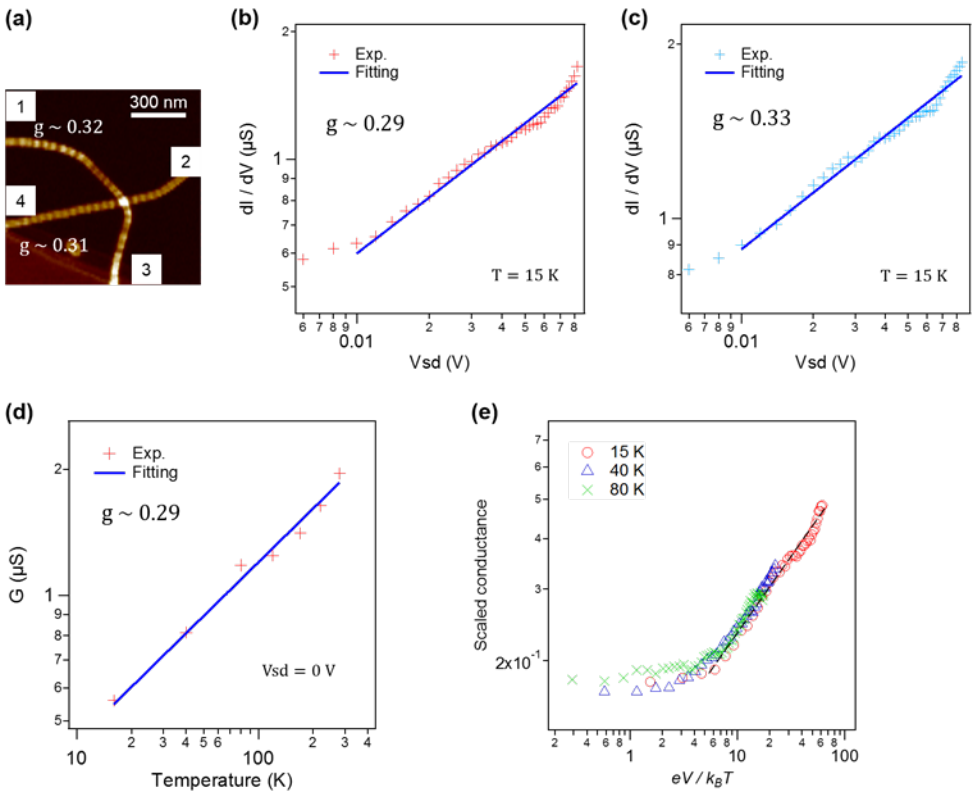

Figure 4.4 Correlation of electron tunneling and plasmon propagation in Luttinger liquid. (a) Near-field optical nanoscopy characterization on a metallic SWNT cross junction. Luttinger parameters are determined to be g ~ 0.32 (tube 1-3) and g ~ 0.31 (tube 2-4) for each of two nanotubes from the measured Luttinger liquid plamons. Metal contacts are denoted by numbers. (b) dI/dV measurement of the electron tunneling probability across the Luttinger liquid junction as a function of electrical bias (V_{sd}) at 15 K (through contacts 1 and 4). The SWNT junction dominates the total resistance and a two probe measurement is carried out. A power function fitting (blue line) yields the power index α ~ 0.43 which corresponds to g ~ 0.29 by using $\alpha = (g + g^{-1} - 2)/4$. (c) Power-law scaling behavior on electrical bias at 15 K at a different backgate voltage with respect to (b), which yields g ~ 0.33. (d) The corresponding temperature-dependent electron tunneling data (zero V_{sd}) with the same backgate voltage as in (b), which yields g ~ 0.29. (e) Scaled conductance $(dI/dV)/T^{\alpha}$ as a function of eV/k_BT at different temperatures, where α is the power component with bias scaling at each temperature. All data collapse onto a single curve reasonably well, which provides an independent verification of Luttinger liquid behavior.

Our near-field optical nanoscopy characterization in Figure 4.4a directly yields Luttinger parameters of the two metallic tubes, g ~ 0.32 (tube 1-3 between the electrical contacts 1 and 3) and g ~ 0.31 (tube 2-4 between the electrical contacts 2 and 4), respectively by the same analysis demonstrated in Figure 4.2. We then independently obtain Luttinger parameter g on the same SWNT cross junction through measuring the electron tunneling probability across two Luttinger liquids by the electrical transport measurements. The results are presented in Figures 4.4a to 4.4d. The resistance of the two individual SWNT devices (1-3 and 2-4) both are ~ 50 kΩ at room temperature which is about 10 times smaller than that of the junction (e.g. 1-4). Since the junction dominates the total resistance, we measure the electron tunneling process across the junction in a two probe configuration between contacts 1 and 4 with contacts 2 and 3 floating. Figure 4.4b shows

the measured d*I*/dV as a function of electrical bias V_{sd} in a double-logarithmic scale across the Luttinger tunneling junction (through contacts 1 and 4) at 15 K. The electron tunneling density of states in Luttinger liquid is characterized by a power-law decay of correlation functions with the decrease of excitation energy (this case is the applied bias) in which the measured d*I*/dV should scale with bias V as $\mathrm{dI/dV} \propto \mathrm{V}^{\alpha}$, where $\alpha = (g + g^{-1} - 2)/4$ for electron tunneling from one Luttinger liquid to another as discussed in Chapter 4.1.

Indeed, the experimentally observed d*I*/dV across the Luttinger liquid junction (red crosses in Figure 4.4b exhibits a well-defined power-law scaling (experimental fitting by blue line in Figure 4.4b), which yields $\alpha \sim 0.43$ and the corresponding $g \sim 0.29$. The power-law index shows a universal behavior, which remains a constant (within the experimental uncertainty) for electrical bias dependence at different backgate voltages and for temperature dependence. Figure 4.4c shows the electrical bias scaling behavior (through contacts 1 and 4) at a different backgate voltage at 15 K; experimental fitting by a power function (blue line) yields $g \sim 0.33$. The same power-law scaling behavior as in Figure 4.4b (with the same backgate voltage) is observed in its corresponding temperature-dependent tunneling data as presented in Figure 4.4d ($\mathrm{G} \propto \mathrm{T}^{\alpha}$ with zero V_{sd}), which yields $g \sim 0.29$. This is consistent with Luttinger liquid prediction for metallic SWNTs with linear band dispersion with a constant tunneling barrier. We also directly measure the $\mathrm{dI/dV}$ at different temperatures, which provides an additional verification of Luttinger liquid behavior for electron tunneling across the SWNT junction. To see this, by following previous reports, we present our d*I*/dV results at different temperatures (15 K, 40 K and 80 K) in Figure 4.4e, where the measured $\mathrm{dI/dV}$ is scaled by T^{α} and the bias voltage is called by the thermal energy $k_B T$. If the experimental results agree with Luttinger liquid theory, all data at different temperatures should be able to collapse onto a single universal curve. As can be seen in the Figure 4.4e, our data at different temperatures indeed collapse onto a single curve reasonably well. The quantitative agreement of Luttinger parameters, that is, g close to ~ 0.30, independently measured from electron tunneling density of states and plasmon propagation velocity in the same well-defined Luttinger liquid system provides an unambiguous demonstration of Luttinger liquid behaviors in SWNTs. This is the first experimental correlation of different interaction-determined Luttinger liquid physical properties in the same carbon nanotube.

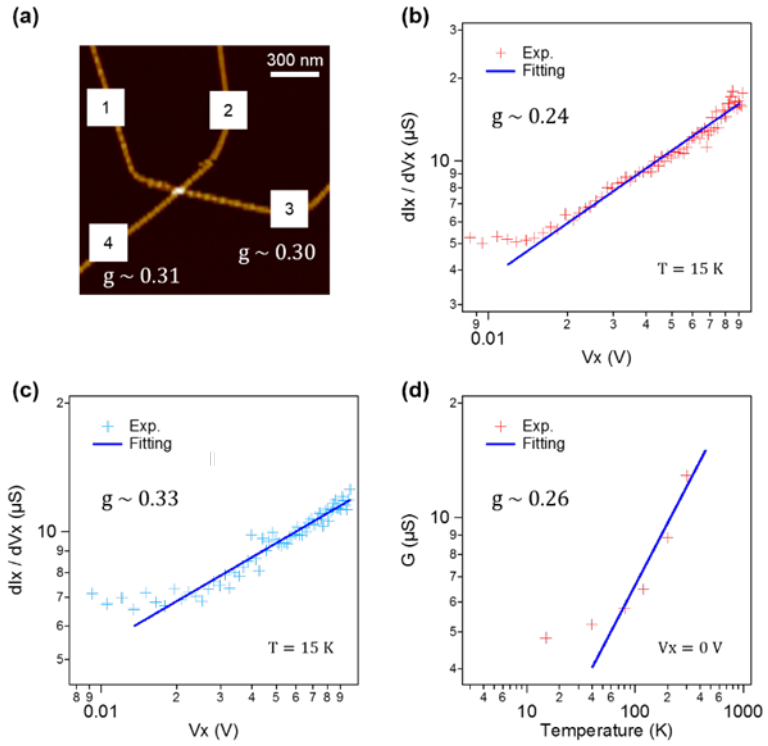

Figure 4.5 Correlation of electron tunneling and plasmon propagation in Luttinger liquid with a low-resistance tunneling junction. (a) Near-field optical nanoscopy characterization on a metallic SWNT cross junction. Luttinger parameters are determined to be g ~ 0.30 (tube 1-3) and g ~ 0.31 (tube 2-4), respectively. Metal contacts are denoted by numbers. (b) Differential conductance (dIx/dVx) measurement of the electron tunneling probability across the Luttinger liquid junction as a function of voltage drop across the junction (Vx) at 15 K. Measurements are carried out in a four probe configuration where the electrical current is forced to flow through contacts 1 and 2 and voltage drop is measured through contacts 3 and 4. A power function fitting (blue line) yields g ~ 0.24 by using $\alpha = (g + g^{-1} - 2)/4$. (c) dIx/dVx at 15 K at a different backgate voltage with respect to (b), which yields g ~ 0.33. (d) The corresponding temperature-dependent electron tunneling data (zero Vx) with the same backgate voltage as in (b), which yields a best fit of g ~ 0.26.

Correlation of electron tunneling and plasmon propagation in another SWNT cross junction is shown in Figure 4.5. The Luttinger parameters for the two constituent metallic SWNTs are determined to be g ~ 0.30 (tube 1-3) and g ~ 0.31 (tube 2-4) as presented in Figure 4.5a based on the near-field optical nanoscopy characterizations. The resistance for tube 1-3 and tube 2-4 is ~ 50 kΩ and ~ 60 kΩ at room temperature, and that the resistance for the SWNT junction is ~ 80 kΩ by a four probe measurement. Compared to the tunneling junction in Figure 4.4, this SWNT cross junction is highly conductive, and thus a four-probe measurement is carried out to investigate the electron tunneling across two Luttinger liquids. The four-probe tunneling measurement is achieved by forcing current to flow through contacts 1 and 2 and using contacts 3 and 4 as voltage probes. We first measure the electron tunneling density of states dIx/dVx as a function of voltage drop Vx across the junction at 15 K. The data is plotted in Figure 4.5b with a double-logarithmic scale. An apparent power-law scaling of tunneling conductance $dIx/dVx \propto (Vx)^{\alpha}$ across the Luttinger liquid tunneling junction is observed. Experimental fitting by a power function (blue line) yields

an effective g value of ~ 0.24. This g value shows a small deviation from the Luttinger parameters (g close to ~ 0.30) obtained from the plasmon velocity measurements on the same Luttinger liquid (Figure 4.5a). The corresponding temperature-dependent data exhibits a g value close to ~ 0.26 (Figure 4.5d), while the electrical bias scaling behavior at a different backgate voltage yields a best fit value of g ~ 0.33 (Figure 4.5c). Presumably this apparent g value variation from 0.24 ~ 0.33 is due to a small change of the tunneling coefficient as a function of the electrical bias and/or temperature that is caused by nanotube deformations under bias conditions. At present, we do not understand the microscopic origin of the small g variation observed in Figure 4.5. It does show that one should be careful with the interpretation of Luttinger parameters g observed solely from electrical tunneling measurements.

4.4 Summary and Discussion

In summary, we directly correlate two completely distinct physical properties, i.e., the electron tunneling density of states and the plasmon propagation velocity in the same SWNT cross junctions, to obtain the first definitive parameter-free test of the Luttinger liquid phenomena in carbon nanotubes. We demonstrate a very good agreement to the Luttinger liquid behavior in Luttinger liquid tunneling junction.

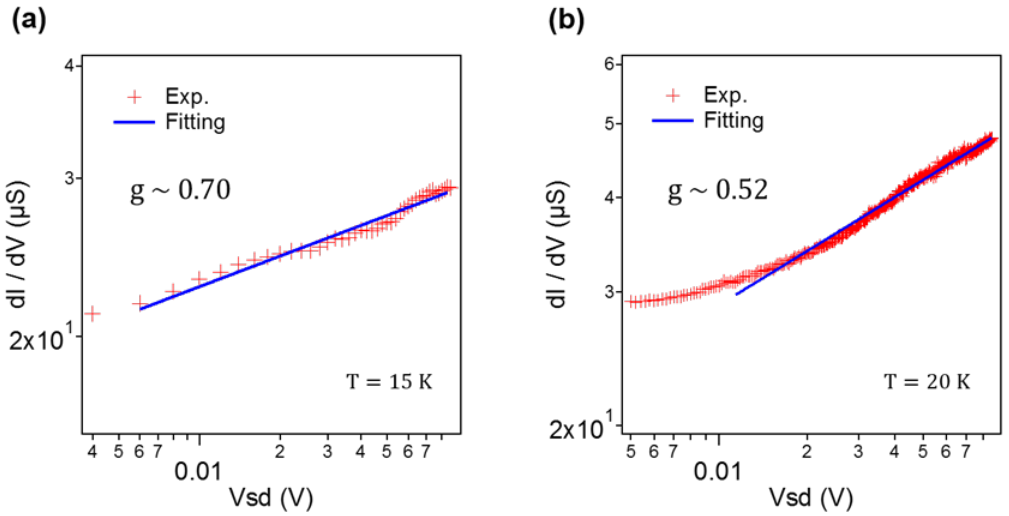

Figure 4.6 Power-law scaling with electrical bias in individual metallic SWNTs. (a) dI⁄dV results for the constituent metallic SWNT (tube 1-3 in Figure 4.4a) at 15 K with the same backgate voltage as used in Figure 4.4b. The power index from our best fitting is α ~ 0.11, which corresponds to g ~ 0.70. (b) dI⁄dV results for another isolated metallic SWNT measured at 20 K. The power index from our best fitting is α ~ 0.23, which corresponds to g ~ 0.52.

dI⁄dV measurements on the constituent individual metallic SWNT (tubes in Figure 4.4) are performed for comparison. The differential conductance of each SWNT exhibits an apparent power-law scaling with bias, which is similar to that reported in previous studies[41-43]. The power index α is related to g as $\alpha = (1/g - 1)/4$ for electron tunneling between metal contacts and SWNTs underneath them. Fitting the experimental data by a power function yields α ~ 0.11

and g ~ 0.70, which deviates significantly from the measured g ~ 0.32 by the near-field optical nanoscopy (Figure 4.4a). Measurements on other isolated individual metallic SWNTs show that the power scaling index varies significantly in different SWNTs, although the optically determined Luttinger parameter remains the same. We attribute this variation to the complicated and unknown nature of SWNT-metal contacts, which can modify the electron tunneling process in an uncontrolled fashion and mask the underlying Luttinger liquid behavior. It highlights the importance of a combined electrical and optical studies for quantitative understanding of Luttinger liquid physics in 1D systems.

Chapter 5 – Nonlinear Luttinger Liquid Plasmons in Semiconducting Single Walled Carbon Nanotubes

5.1 Introduction and Background

Electrons in three- and two-dimensional metals are well represented by weakly interacting quasi-particles within Fermi liquid theory. However, this theory breaks down in one dimension (1D) where Coulomb interactions become dominant and can qualitatively alter the electronic behaviors. Luttinger liquid theory, which is based on the linearization of the dispersion relation of the particles constituting the fluid, can successfully describe many exotic phenomena in 1D metals such as spin-charge separation and power-law dependence of spectral functions near the Fermi level[37-39, 42, 43, 59-61]. However, the electronic band dispersion in most 1D systems is often not strictly linear and the linearization taken in Luttinger liquid theory limits its validity to low-energy electron behaviors. In order to describe high-energy quasi-particle excitations and dynamics, novel theoretical approaches have been employed to replace the linear dispersion with a generic one, which is known as nonlinear Luttinger liquid theory[46, 47, 62-68]. This nonlinear theory predicts many intriguing electron behaviors beyond the linear Luttinger liquid paradigm. For instance, the collective electron excitations (i.e. plasmons) in a linear Luttinger liquid are expected to be extremely long-lived due to the absence of an intrinsic relaxation mechanism. We have shown in Chapters 3 and 4 that metallic SWNTs with the linear dispersion are ideal realizations of a linear Luttinger liquid. Long-lived plasmons are observed in metallic SWNTs with peculiar signatures well reproduced by the linear Luttinger liquid formulism. However, in a nonlinear Luttinger liquid, the nonlinearity of the band dispersion can strongly mix different plasmon excitations, resulting in a drastic reduction of plasmon lifetime. Such unusual excited state dynamics of a nonlinear Luttinger liquid have rarely been experimentally explored previously.

As discussed in Chapter 2.1, semiconducting SWNTs have a hyperbolic dispersion, providing an attractive realization of a nonlinear Luttinger liquid. There is large nonlinearity at the bottom of the band and this band curvature decreases as the band progressively becomes linear with higher Fermi energy. By tuning the carrier density in SWNTs while in situ performing infrared nanoimaging, we can investigate how nonzero band curvature affects the plasmonic excitations in the system. The experimental results will serve to test the nonlinear Luttinger liquid theory in semiconducting SWNTs.

5.2 Gate Dependent Infrared Nanoimaging of Metallic and Semiconducting SWNTs

Metallic and semiconducting SWNTs with diameter ranging from 0.7 to 2.0 nm are directly grown on hexagonal boron nitride (h-BN) flakes exfoliated on SiO2 (285 nm)/Si substrates by chemical vapor deposition (CVD). SWNTs on h-BN flakes are ultraclean and very long and can

be readily integrated into field-effect transistor (FET) devices. We probe the plasmons in gated nanotube devices at different carrier densities using infrared scanning near-field optical microscopy (SNOM) as illustrated in Figure 5.1a. This infrared nano-imaging technique is based on a tapping mode atomic force microscopy (AFM). Infrared (IR) light with wavelength 10.6 μm is focused onto the apex of a gold coated AFM tip. The sharp tip with its large momentum simultaneously enables the excitation of the plasmons and scattering of this plasmon field to the far field. The back scattered signal contains essential information about the plasmons and is captured by a mercury cadmium telluride (MCT) detector. The excited plasmon wave propagates along the nanotubes and gets reflected by the nanotube ends or other scatters. The interference between the tip-launched plasmon field and the reflected plasmon field produces a periodic electric field distribution. We probe this periodic electric field by scanning the tip along the nanotube, which enables the real-space visualization of the plasmons.

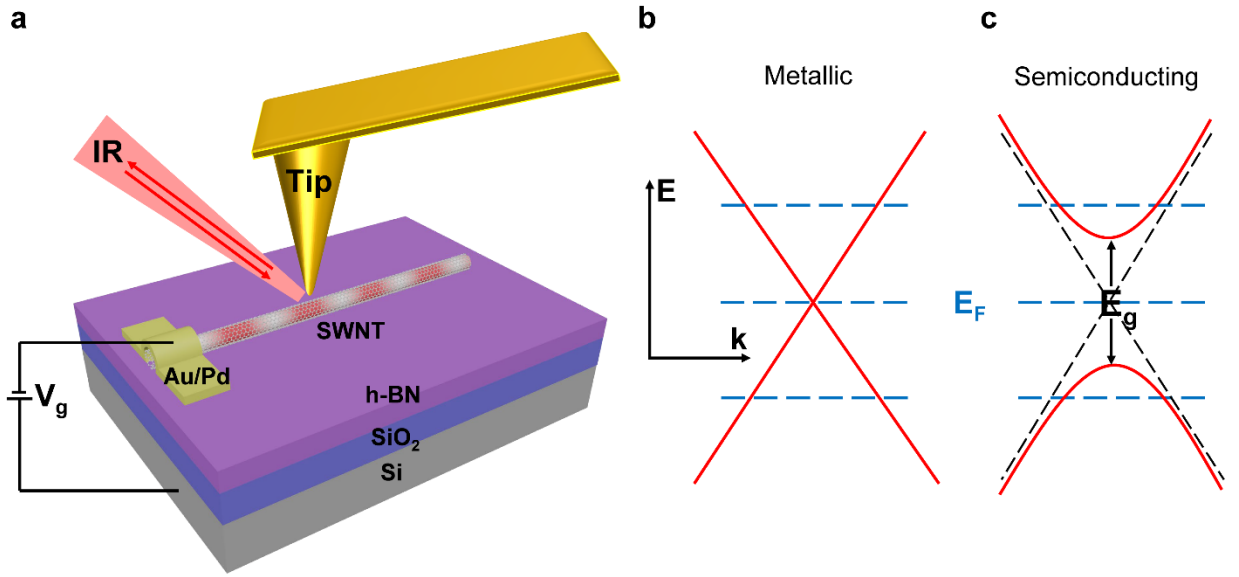

Figure 5.1 Schematic of SNOM of SWNTs with carrier density controlled by electrostatic gating. (a), Schematic of infrared nano-imaging of a nanotube FET device. SWNTs are directly grown on hexagonal boron nitride (h-BN) flakes exfoliated on SiO_2 (285 nm)/Si substrates by chemical vapor deposition (CVD). A back gate voltage V_g is applied between the metal electrode (Au/Pd) contacting the SWNT and the Si substrate to tune the carrier concentration in the SWNT. For infrared (IR) nano-imaging, IR light with wavelength 10.6 μm is focused onto the apex of a gold coated AFM tip. The sharp tip with its large momentum enables the excitation of the plasmons. The excited plasmon wave propagates along the nanotubes and gets reflected by the nanotube ends or other scatters. The interference between the tip-launched plasmon field and the reflected plasmon field produces a periodic electric field distribution schematically illustrated by the interference fringes in the SWNT. Probing of the electric field by scanning the tip along the nanotubes enables the direct visualization of the plasmons. (b), Band structure of metallic SWNTs. Metallic SWNTs feature a gapless linear energy-momentum (E-k) dispersion schematically shown as the red curve. (c), Band structure of semiconducting SWNTs. Semiconducting SWNTs feature a hyperbolic E-k dispersion (schematically shown as the red curve) with a finite band gap Eg. The diagonal black dashed lines indicate the linear band structure of metallic SWNTs for comparison with the hyperbolic band structure of semiconducting SWNTs. When a back gate voltage Vg is applied in a relative to the charge neutral point V_{cnp}, the Fermi level EF indicated by the horizontal dashed blue lines in metallic and semiconducting SWNTs can be continuously tuned.

The electronic band structures of SWNTs have been discussed in Chapter 2.1. The band structures of metallic and semiconducting SWNTs are illustrated in Figures 5.1b and 1c, respectively. Metallic nanotubes feature a gapless linear band dispersion, $E = \hbar v_0 k_F$, where $\hbar$ is the reduced Planck's constant, $v_0 \sim 0.8 \times 10^6\ m/s$ is the Fermi Velocity in graphene, and k_F is the Fermi wavevector. Their 1D linear bands provide an ideal realization of the linear Luttinger liquid. Semiconducting nanotubes, in contrast, have a finite band gap E_g and feature a hyperbolic dispersion, $E^2 = (E_g/2)^2 + (\hbar v_0 k_F)^2$, where E_g is inversely proportional to the nanotube diameter d as $E_g = 0.75eV/d\ (nm)$. When a back gate voltage V_g is applied (Figure 5.1a) relative to the charge neutral point V_{cnp}, the Fermi level E_F in both metallic and semiconducting SWNTs can be continuously tuned from hole doping to charge neutrality and to electron doping as illustrated in Figures 5.1b and 5.1c. The charge neutral point V_{cnp} is the gate voltage needed to offset the unintentional doping usually coming from the substrate.

In Figure 5.2, we systematically investigate the dependence of plasmon behaviors on carrier density in semiconducting SWNTs and compare that with plasmon behaviors in doped metallic SWNTs. When gate voltage V_g is varied from -20 to 20 V, the carrier type in SWNTs changes from hole doping to charge neutrality and then to electron doping. The near-field optical responses at these different gate voltages are shown in Figures 5.2a to 5.2f. The topography recorded simultaneously is shown in the top right inset in Figure 5.2a. In the near-field images, nanotubes labeled as M1 and M2 in Figure 5.2a exhibit prominent oscillation peaks at all gate voltages (Figures 5.2a to 5.2f). These are gapless metallic SWNTs with linear dispersion. The peaks in the near-field images correspond to the constructive interference between the plasmon wave launched by the tip and that reflected by the nanotube end. Plasmon wavelength can be simply determined as twice the oscillation period. By fitting the line profiles along the nanotubes in the near-field images at different gate voltages with a damped oscillator form $e^{-2\pi x/(Q\cdot\lambda_P)} \sin\left((4\pi x)/\lambda_p\right)$, we can determine the plasmon wavelength λ_p to be ~ 90 nm and the quality factor Q to be ~ 22 and observe that they are largely unchanged at different gate voltages. Plasmon velocity can be determined from $v_p = \lambda_p f \sim 2.5 \times 10^6\ m/s$ where f ~ 28.3 THz is the frequency of the excitation light. The Luttinger liquid parameter g, describing the interaction in SWNTs, can then also be determined to be $g = v_0/v_p \sim 0.31$, which indicates strong coulomb repulsion between electrons in metallic SWNTs. In marked comparison, near-field optical responses in nanotubes labeled as S1 and S2 in Figure 5.2a depend sensitively on gate voltages. These two nanotubes correspond to semiconducting SWNTs with hyperbolic dispersion. When the carrier density is near charge neutrality (Figure 5.2c), the near-field response is dramatically depleted and we observe weak contrast against the substrate. At substantial doping, well-defined plasmon features emerge and evolve with the gate voltage in both semiconducting nanotubes. The distinctly different plasmon behaviors highlight the critical role of nonlinear band dispersion in semiconducting SWNTs which goes beyond the conventional linear Luttinger liquid paradigm in metallic SWNTs.

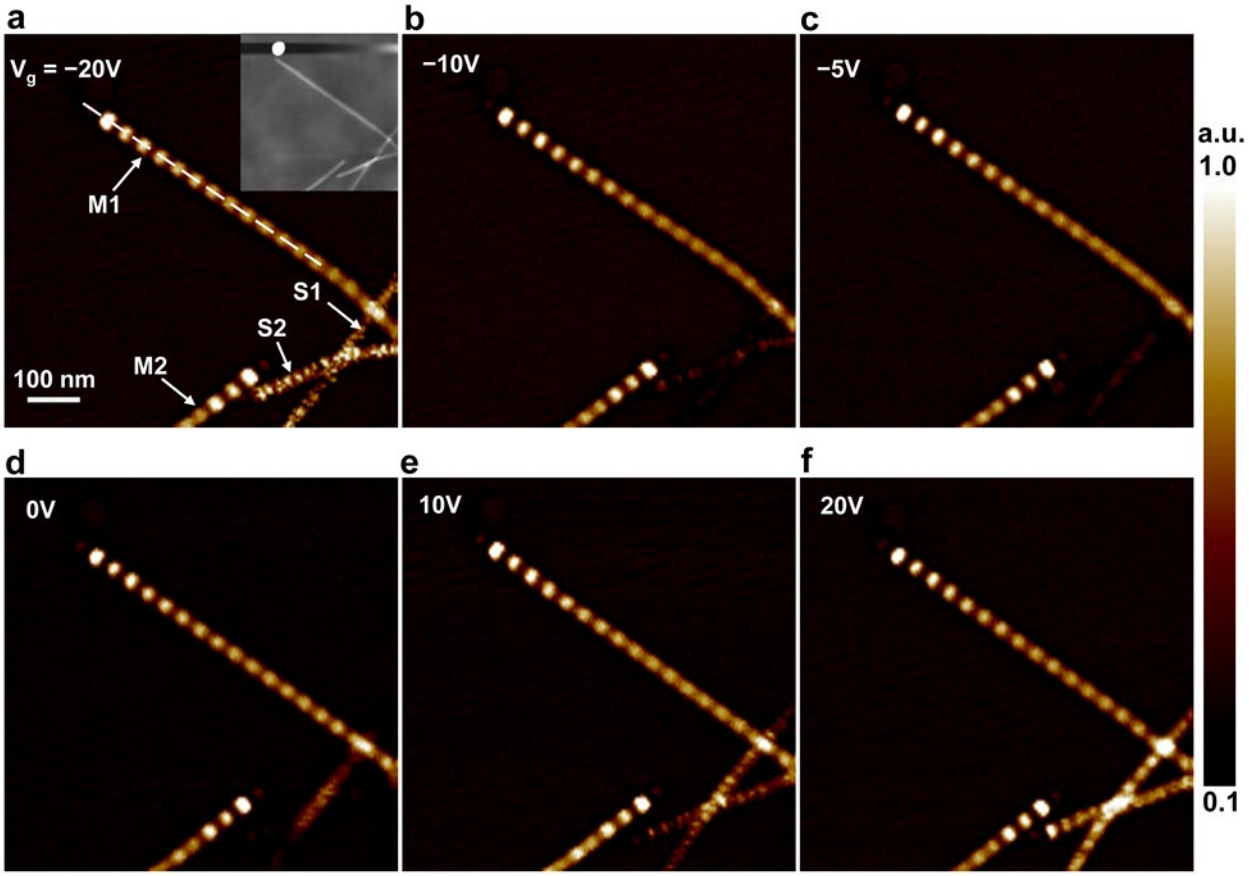

Figure 5.2 Infrared nano-imaging of metallic and semiconducting SWNTs at different gate voltages. From (a) to (f), the gate voltage is varied from -20 to 20V. The carrier density changes from hole doping to charge neutrality and then to electron doping. The plasmon features in metallic nanotubes labeled as M1 and M2 in a are largely unchanged. In marked comparison, near-field optical responses in semiconducting nanotubes labeled as S1 and S2 in a depend sensitively on gate voltages. The line profiles along the nanotube (indicated by the white dashed line in (a)) reveal how the plasmon wave in metallic nanotube M1 gets damped as it propagates. The profiles for different gate voltages ((a) to (f)) are plotted in Figure 5.4. The inset in (a) shows the topography recorded simultaneously with the near-field images.

Next we examine comprehensively the plasmon behaviors in semiconducting nanotubes and their dependence on carrier density. Figure 5.3a shows the topography of a semiconducting nanotube and the inset blue curve shows the height profile along the white dashed line across the nanotube. The diameter is determined to be 2 nm from the height profile and the nanotube thus has a band gap of ~ 0.37 eV. The near-field responses of the nanotube at different gate voltages from -20 to 24 V are presented in Figures 5.3b to 5.3l. The near-field response evolves in a systematic manner, which is consistent with the semiconducting SWNTs in Figure 5.2. At $V_g = -5V$ (Figure 5.3e), the response is almost completely depleted, which corresponds to the charge neutral point. When carrier density is increased to either hole-doped side (Figures 5.3b to 5.3d) or electron-doped side (Figures 5.3f to 5.3l), there is an increase in the near-field optical response and well-defined plasmons emerge at substantial doping as manifested by the oscillation peaks near the nanotube end. Line profiles along the dashed line in Figures 5.3b reveal how the plasmon wave is damped

as it propagates (Figure 5.4). By fitting the line profiles with a damped oscillator form, we can extract both the plasmon wavelength and quality factor as a function of gate voltage.

Figure 5.4 displays the line profiles of near-field images and plasmon analysis. Plasmon analysis for metallic SWNTs at different gate voltages is shown in Figure 5.4a. The line profiles (solid lines) along the white dashed line indicated in Figure 5.2a in the main text at three gate voltages are shown. Fitting of the profiles by a damped oscillator form (dashed lines) yields a plasmon wavelength ~ 90 nm and a quality factor ~ 22 for all gate voltages. Plasmon analysis for semiconducting SWNTs at different gate voltages is shown in Figure 5.4b. Line profiles (solid lines) along the white dashed line indicated in Figure 5.3b in the main text at different gate voltages are shown. Fitting of the profiles by a damped oscillator form (dashed lines) yields gate-dependent plasmon wavelength and quality factor. The results are summarized in Figures 5.5b and 5.5d. It is evident that plasmons in the semiconducting SWNT can be continuously tuned by means of electrostatic gating. With increasing gate voltage and thus higher Fermi level, the plasmon wavelength increases and the quality factor also shows concomitant growth. Below a critical carrier density indicated by the dashed line in Figure 5.5b, the damping is too large to support well-defined plasmons.

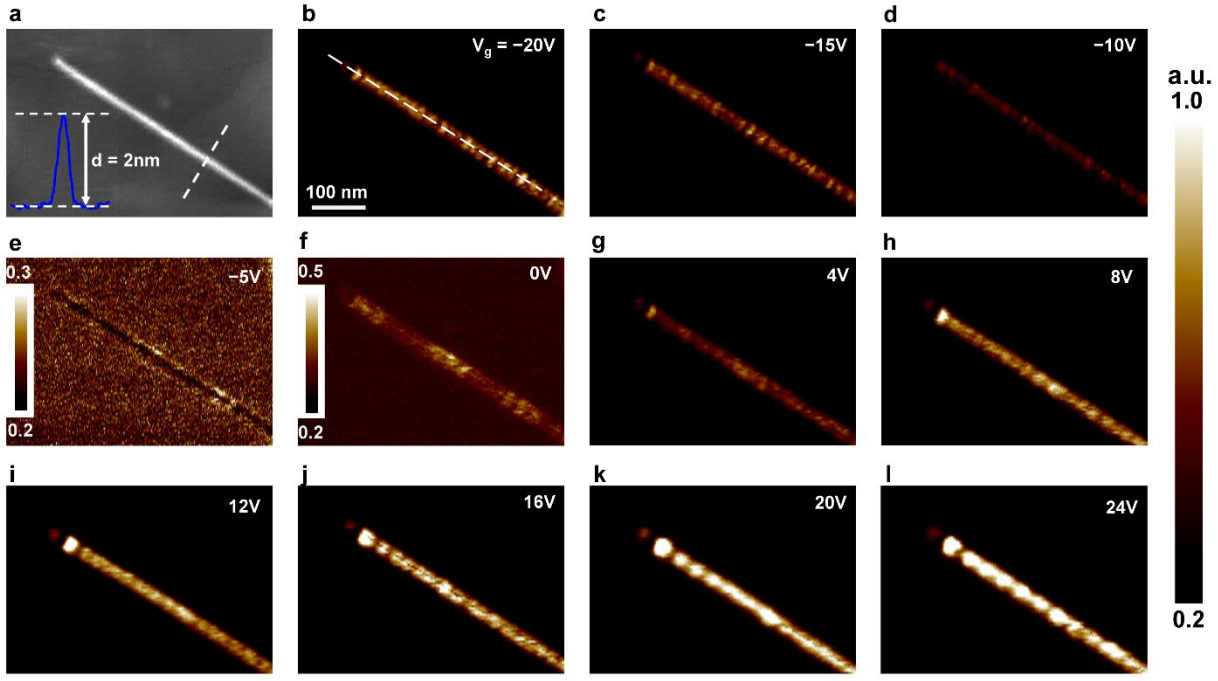

Figure 5.3 Gate-tunable plasmons in semiconducting SWNTs. (a), AFM topography of a semiconducting nanotube. The inset blue curve is the height profile along the white dashed line across the nanotube and the diameter is determined to be 2 nm from the profile. (b) to (l), Near-field responses of the semiconducting nanotube at different gate voltages from -20 to 24V. Plasmons in the semiconducting SWNT can be continuously tuned by means of electrostatic gating. With increasing gate voltage and thus higher Fermi level, the plasmon wavelength increases and the quality factor also shows concomitant growth. The figures share the same color scale (to give a direct comparison of the infrared responses at different gate voltages) except for (c) and (f), where the scales shown in insets are intentionally made smaller to offer better contrast between the nanotube and the substrate. The line profiles along the nanotube (indicated by the white dashed

line in b) reveal how the plasmon wave in the semiconducting nanotube gets damped as it propagates. The profiles for different gate voltages ((h) to (i)) are plotted in Figure 5.4b.

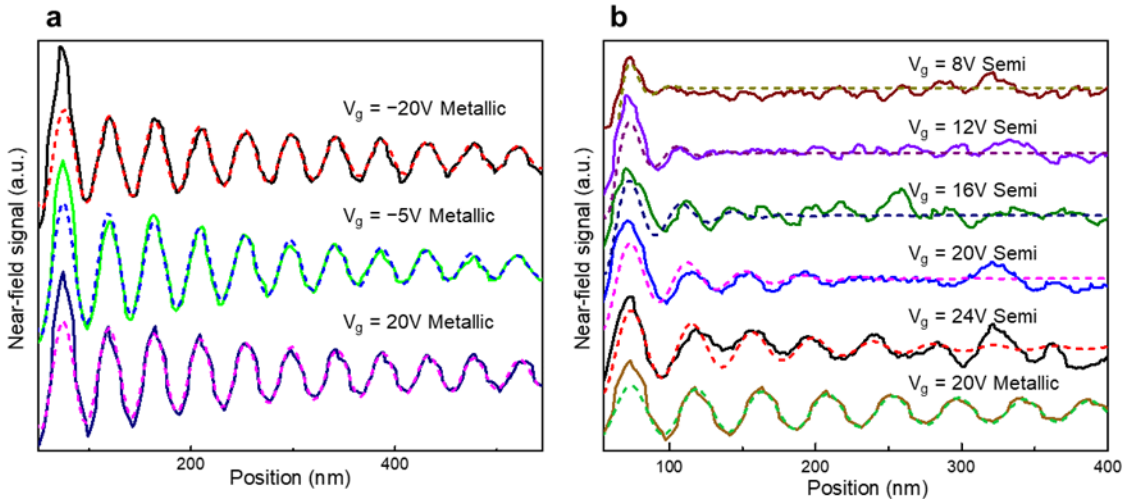

Figure 5.4 Line profiles of near-field images and plasmon analysis. (a), Plasmon analysis for metallic SWNTs at different gate voltages. The line profiles (solid lines) along the white dashed line indicated in Figure 5.2a in the main text at three gate voltages are shown. Fitting of the profiles by a damped oscillator form (dashed lines) yields a plasmon wavelength ~ 90 nm and a quality factor ~ 22 for all gate voltages. (b), Plasmon analysis for semiconducting SWNTs at different gate voltages. Line profiles (solid lines) along the white dashed line indicated in Figure 5.3b in the main text at different gate voltages are shown. Fitting of the profiles by a damped oscillator form (dashed lines) yields gate-dependent plasmon wavelength and quality factor.

As observed in Figure 5.2, the gate-independent plasmon behavior in metallic SWNTs is well described by linear Luttinger liquid theory. For an individual suspended carbon nanotube of radius R screened by a concentric metal shell of radius R_s, the linear Luttinger liquid theory predicts the Luttinger liquid interaction parameter g to be

$$\frac{1}{g} = \frac{v_p}{v_F} = \sqrt{1 + \frac{8e^2}{4\pi\varepsilon_{eff}\pi\hbar v_F}\ln\left(\frac{R_s}{R}\right)}$$

where v_p is the velocity of the collective charge mode, i.e. plasmon velocity, v_F is the Fermi velocity and ε_{eff} is the effective dielectric constant due to substrate screening. This parameter g describes the interaction type and strength in a Luttinger liquid and is only a function of Fermi velocity and the ratio R_s/R for a nanotube under given dielectric environment. The plasmon wavelength λ_p for a given frequency f is related to g as $\lambda_p = v_p/f = v_F/(gf)$. Because the Fermi velocity is a constant in metallic SWNTs, all the Luttinger liquid phenomena related to g, including the plasmon excitations, will remain the same regardless of carrier density.

5.3 Gate Tunable Nonlinear Luttinger liquid Plasmons in Semiconducting SWNTs

In contrast, the gate-tunable plasmon wavelength in semiconducting nanotubes stems from the hyperbolic band dispersion, where the Fermi velocity v_F depends on carrier density. As illustrated in Figure 5.5a, the Fermi velocity indicated by the slope of the black tangent line increases with higher Fermi energy. Due to the dominant strong repulsive interaction in SWNTs, plasmon velocity v_p is approximately proportional to $\sqrt{v_F}$ and plasmon wavelength in semiconducting nanotubes with band gap E_g depend on Fermi wavevector k_F as:

$$\lambda_p = \lambda_{p0}\sqrt{\frac{v_F}{v_0}} = \lambda_{p0}\sqrt{\frac{\hbar v_0 k_F}{\sqrt{(E_g/2)^2 + (\hbar v_0 k_F)^2}}}$$

where λ_{p0} and v_0 are the plasmon wavelength and Fermi velocity in metallic nanotubes for a given frequency. The dependence has been discussed in detail in Chapter 2.2. Thus, one can expect that the plasmon wavelength in semiconducting nanotubes will increase and progressively approach that in metallic ones with larger k_F. The experimentally observed tunable plasmon wavelength at substantially high doping in semiconducting nanotubes (Figures 5.3h to 5.3l) is well reproduced by the theoretical model (Figure 5b). In this fitting we have used $k_F = \frac{\pi}{4}n = \frac{\pi}{4}\beta C_g|V_g - V_{cnp}|$, where n is the carrier density, C_g is the geometric capacitance, β is a fitting parameter and indicates the overall gate efficiency.

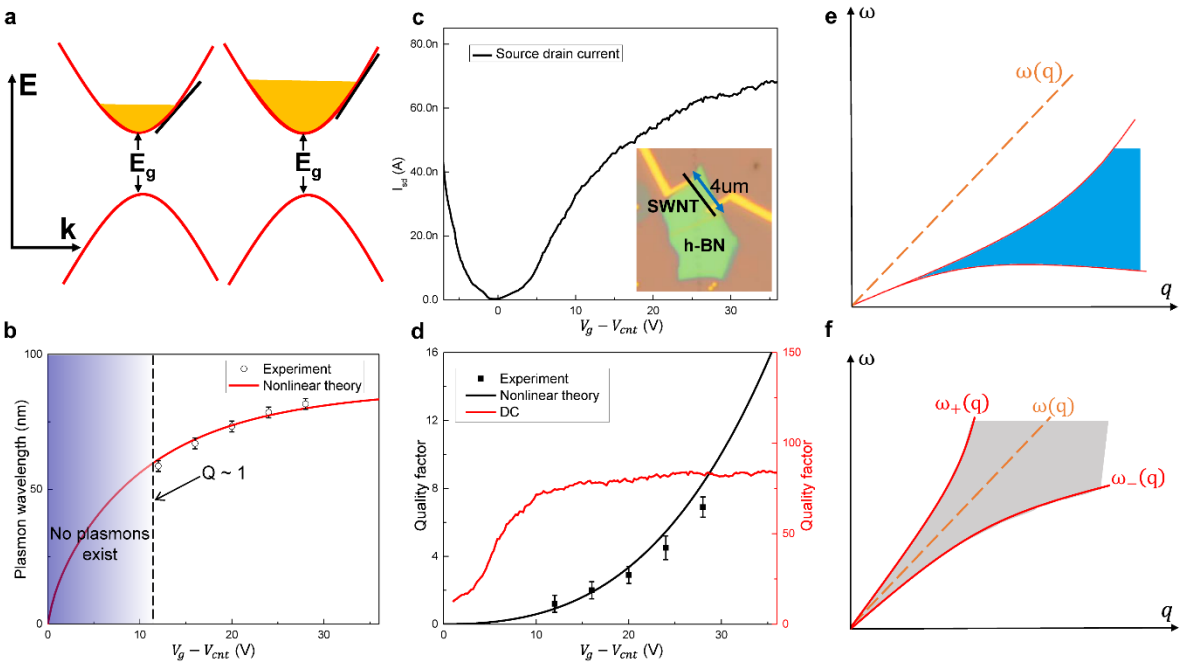

Figure 5.5 Nonlinear Luttinger liquid model and comparison with experimental results. (a), Illustrative hyperbolic energy-momentum (E-k) dispersion (red curve) and Fermi energy (filled yellow region) of a semiconducting SWNT with a band gap E_g. The Fermi velocity indicated by the slope of the black tangent line increases with higher Fermi energy. (b), Dependence of plasmon wavelength on gate voltage agrees

well with the theoretical model. Below a critical doping indicated by the dashed line (shaded blue area), the plasmon quality factor Q is not large enough for well-defined plasmons to exist. (c), I_{sd}-V_g (source drain current-gate voltage) curve for a 2 nm diameter semiconducting nanotube at a bias $V_{sd} = 6\ mV$. The inset is an optical image of the device with a channel length of ~ 4 μm. (d), The nonlinear theory (black line) can well reproduce the experimental dependence of quality factor on gate voltage (black symbols). On the other hand, the plasmon quality factor will be very high and exhibit a completely different gate dependence (red line and right scale) if the damping rate is the same as the electron scattering rate inferred from DC transport measurements. (e), Illustration of the plasmon dispersion within the RPA. Here the plasmon excitation, ω(q), indicated by the orange dashed line always lies outside the electron-hole continuum indicated by the blue shaded area and is thus free from Landau damping. f, Illustrative diagram of DSF from the universal nonlinear Luttinger liquid theory. In a nonlinear Luttinger liquid, the plasmon mode indicated by the gray shaded area is not an exact eigenstate $\omega(\mathrm{q}) = v_p q$ but is broadened with upper and lower bound $\omega_{\pm}(\mathrm{q}) = v_p q \pm q^2/2\tilde{m}$. Error bars in b and d indicate a 95% confidence interval determined from the curve fitting of the line profiles along the nanotube in Figure 5.3 with a damped oscillator form.

Apart from the tunable plasmon wavelength, the quality factor also depends sensitively on gate voltage as shown in Figure 5.5d. The tunable damping behaviors are reminiscent of those in graphene plasmons, which can be captured by Landau damping within the random-phase approximation (RPA). The gate-dependent plasmon damping behavior in semiconducting nanotubes shown in Figures 5.3h to 5.3l, however, cannot be explained by this simple picture. No interband damping can exist in a semiconducting nanotube due to its large band gap (~ 0.37 eV) compared to the excitation energy (~ 0.10 eV). It has also been shown that 1D plasmons will not decay to a single electron-hole pair through intraband scattering within the RPA[69]. As illustrated in Figure 5.5e, within the RPA theory, the plasmon excitation, ω(q), indicated by the orange dashed line, always lies outside the electron-hole continuum indicated by the blue shaded area, and thus is free from Landau damping.

We can rule out defect and/or acoustic phonon scattering as a main contribution to the plasmon damping by comparing the infrared near-field nanoscopy results with the electronic transport in semiconducting SWNTs with the same diameter and growth conditions. Figure 5.5c displays the gate-dependent DC transport data of a representative SWNT with a diameter of 2 nm and a channel length L of 4 μm by recording the source drain current I_{sd} for different gate voltages at a bias of $V_{sd} = 6\ mV$. The optical image of the SWNT device is shown in the inset. From the measured gate-dependent 1D channel resistance R, we can estimate the mean free path $L_m = \frac{L}{R4e^2/h - 1}$ and scattering time $\tau = L_m/v_F$ at different gate voltages. The scattering of electrons close to the Fermi surface, which dominates the electronic transport, is mainly due to defects and acoustic phonons in semiconducting SWNTs at room temperature[6, 70]. We obtain an electron scattering time longer than 300 fs, corresponding to a scattering rate of ~ $3ps^{-1}$, for carrier density approaching the saturation region for the semiconducting nanotube, which is consistent with previous findings in electronic transport studies of high-quality semiconducting SWNTs[6, 71]. This electron scattering rate is over an order of magnitude smaller than the observed plasmon damping rate. If we assume plasmon damping to have similar origins as the DC transport (i.e. dominated by defect and acoustic phonon scattering), the quality factor determined by ωτ will be very high and exhibit a completely different gate dependence (red line and right scale in Figure 5.5d) compared with the plasmon behavior. Our experimental data cannot be accounted for by

emission of optical phonons either, because the optical phonon scattering should have a weaker dependence on the doping concentration.

The observed unusual gate-dependent plasmon damping in semiconducting nanotubes, on the other hand, can be naturally understood as a consequence of the strong plasmon-plasmon coupling in a nonlinear Luttinger liquid: in metallic nanotubes with prefect linear dispersion, the plasmon excitations are free long-lived bosons without an intrinsic relaxation mechanism within the linear Luttinger liquid theory paradigm. The nonlinear band dispersion in semiconducting nanotubes, however, can enable extremely strong coupling between different plasmon modes because they all propagate at the same speed. As a result, a high-energy plasmon can efficiently decay into multiple low-energy plasmons in semiconducting nanotubes.

A universal description of the dynamic response function in a nonlinear Luttinger liquid has been theorized previously[46, 47]. As discussed in Chapter 2.2, the dynamic excitation of plasmons in a 1D system is determined by the dynamic structure factor (DSF). For a linear Luttinger liquid as in metallic SWNTs, the DSF takes the form $\mathrm{S}(\mathrm{q},\omega) = 2g|q|\delta(\omega - v_p q)$. This suggests that the plasmon mode features a linear dispersion $\omega(\mathrm{q}) = v_p q$ indicated by the dashed orange line in Figure 5.5f and is free of intrinsic relaxation. For a nonlinear Luttinger liquid as in gated semiconducting SWNTs, the DSF is given by

$$\mathrm{S}(\mathrm{q},\omega) = 2\frac{\tilde{m}g}{|q|}\theta\left(\frac{q^2}{2\tilde{m}} - \left|\omega - v_p q\right|\right)$$

with an effective mass $\tilde{m}$. The effective mass $\tilde{m}$ depends on electron-electron interactions and it can be expressed as $\frac{1}{\tilde{m}} = \frac{v_p}{2g}\frac{\partial}{\partial E_F}(v_p\sqrt{g})$. The plasmon mode is thus not an exact eigenstate but is broadened with upper and lower bound$\omega_{\pm}(\mathrm{q}) = v_p q \pm q^2/2\tilde{m}$, as indicated by the red lines in Figure 5.5f. The width of the broadening is $\delta\omega(q) = q^2/\tilde{m}$. For a given frequency, a set of plamson modes with different momenta can be excited in the shaded gray area where DSF differs from zero. This broadening reflects the finite lifetime and damping of the plasmons. Below a critical Fermi energy for a given frequency, indicated by the horizontal dashed line r_c in Figure 5.5f, the damping will be so large that no well-defined plasmons exist. This critical line corresponds to the dashed line in Figure 5.5b, below which no well-defined plasmons are observed experimentally. As the Fermi energy E_F increases compared to the excitation energy ω, the broadening becomes less severe and well-defined plasmons begin to emerge in agreement with experimental observations.

This dissipation reflected in the broadening of the DSF can be further quantitatively characterized as $\delta\omega/\omega = \omega/\tilde{m}v_p^2$. In semiconducting nanotubes with hyperbolic dispersion, this broadening depends on Fermi wavevector k_F as

$$\frac{\delta\omega}{\omega} = \frac{3\sqrt{3}}{8}\left(\frac{\sqrt{(E_g/2)^2 + (\hbar v_0 k_F)^2}}{\hbar v_0 k_F}\right)^{\frac{5}{4}} \frac{(E_g/2)^2}{(E_g/2)^2 + (\hbar v_0 k_F)^2}\frac{\omega}{v_0 k_F}$$

The plasmon quality factor determined by this nonlinear dispersion can be described as $\omega/\delta\omega$ and its dependence on gate voltage is depicted in Figure 5.5d. The nonlinear theory (black line) can well reproduce the experimental results (black symbols). With increasing carrier density and Fermi energy, the band structure gradually approaches linear dispersion. This decrease in the nonlinearity of dispersion leads to the increase of plasmon lifetime and a higher quality factor observed in the experiments. The small discrepancy might indicate that other damping mechanisms also play a role, but nevertheless, are not dominant in our experiment. We conclude that in doped semiconducting nanotubes with hyperbolic dispersion, at the high-energy regime where excitation energy is comparable to Fermi energy, the system should be described as a nonlinear Luttinger liquid and the plasmon damping mechanism is dominated intrinsically by the nonzero curvature of the band dispersion. Note that if we probe at the low-energy regime where excitation energy is much smaller than Fermi energy, $\delta\omega/\omega$ will be vanishingly small and the system will reproduce the linear Luttinger liquid regime. The intriguing gate dependent nonlinear Luttinger liquid plasmon behaviors offer the alluring capability of active electrical switching and tuning of plasmons in semiconducting nanotubes. The highly confined and tunable plasmons and their compatibility with FET devices hold great promise for novel nanophotonic application[72, 73].

5.4 Summary and Outlook

Studying and understanding how electrons interact in many-body systems at a fundamental level is the core in condensed matter physics. The Luttinger liquid formalism provides a general framework for characterizing low-energy physics of interacting electrons in one dimension (1D), where the electronic dispersion is assumed to be strictly linear. But the electronic band dispersion in real 1D systems is often not strictly linear and the linearization taken in the Luttinger liquid theory limits its validity to low-energy electron behaviors. In order to describe high-energy quasi-particle excitation and dynamics, novel theoretical approaches have been employed to replace the linear dispersion with a generic one, which is known as the nonlinear Luttinger liquid theory. Despite a large body of theoretic work, there are precious few experiments addressing the nature of quantum excitations in 1D quantum fluids.

In this Chapter, we probe nonlinear Luttinger liquid plasmonic excitations using gated semiconducting single walled carbon nanotubes (SWNTs) as a model system, and compare the behavior to that of a linear Luttinger liquid in metallic SWNTs. We combine infrared nano-imaging and electronic transport to systematically investigate behaviors of nonlinear Luttinger liquid plasmons in semiconducting SWNTs with carrier density controlled by electrostatic gating. We show that both the propagation velocity and the dynamic damping of the plasmons can be tuned continuously in semiconducting SWNTs, which is well captured by the nonlinear Luttinger

liquid theory. These behaviors are in striking contrast to the gate-independent plasmons in metallic nanotubes described by the linear Luttinger liquid theory.

Our findings provide fundamental insight into 1D systems beyond the conventional linear Luttinger liquid paradigm. It can open up new avenues to quantitatively understand the nature of excitations in different interacting 1D systems. The highly confined and gate-tunable plasmons demonstrated in our SWNTs field-effect transistor devices may also enable novel nanophotonic applications, including SWNTs-based chip integrated plasmonic circuits, quantum plasmonics and ultra-compact plasmonic sensing.

Chapter 6 – Metallic Carbon Nanotube Nanocavities as Ultracompact and Low-loss Fabry-Perot Plasmonic Resonators

6.1 Introduction and Background

We have discussed highly confined low-loss linear Luttinger plasmons in metallic SWNTs in Chapter 3 and gate tunable nonlinear Luttinger liquid plasmons in Chapters 5. Plasmons in metallic SWNTs at infrared frequencies exhibit the combination of low dispersion, deep subwavelength confinement (mode volume $<10^{-8}\ \lambda_0^3$) and high quality factor ($Q > 10$). Plasmonic resonators may take advantage of these unique capabilities and enable manipulation of light matter interaction at the nanoscale[74-77]. Plasmonic resonators based on noble metallic nanostructures have long been studied, but they typically operate in the visible and near-infrared range and are hindered by a trade-off between optical field confinement and losses imposed by Landau damping. Alternatives such as phonon polaritons in polar crystals are constrained to the Reststrahlen bands and cannot achieve broadband response[78-80].

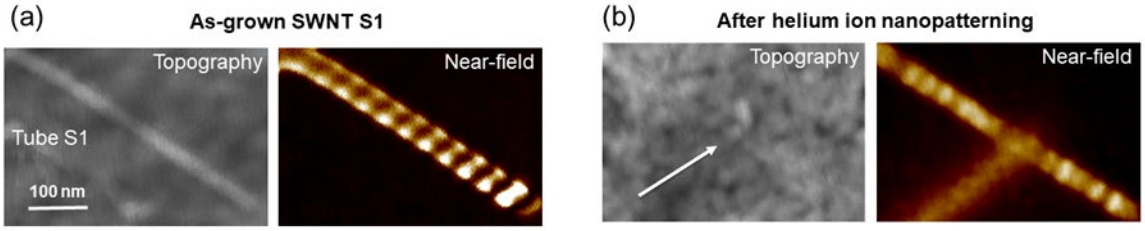

Figure 6.1 Helium ion microscopy (HIM) and nanopatterning of SWNTs. (a) Topography and near-field image of an as-grown SWNT S1. This metallic nanotube is ultraclean and exhibits prominent plasmon oscillations. (b) Topography and near-field images of tube S1 after helium ion nanopatterning. The white arrow indicates where line nanopatterning is performed. Tube S1 after helium ion nanopatterning features less pronounced plasmon oscillations and exhibits multiple plasmon scattering centers potentially due to random defects induced by helium ion implantation.

Long SWNTs can be fabricated into plasmonic nanocavities for control of light at the nanoscale. Nanolithography based on electron or focused ion beam has long been used to fabricate plasmonic nanostructures. Figure 6.1 shows infrared nanoimaging of a metallic nanotube before and after helium ion nanopatterning. Tube S1 after helium ion nanopatterning features less pronounced plasmon oscillations and exhibits multiple plasmon scattering centers potentially due to random defects induced by helium ion implantation. A clean nanofabrication method with resolution down to nanometers is required so that the quality of as-fabricated nanocavities is not compromised.

6.2 Electrode Free Scanning Probe Nanolithography of SWNTs

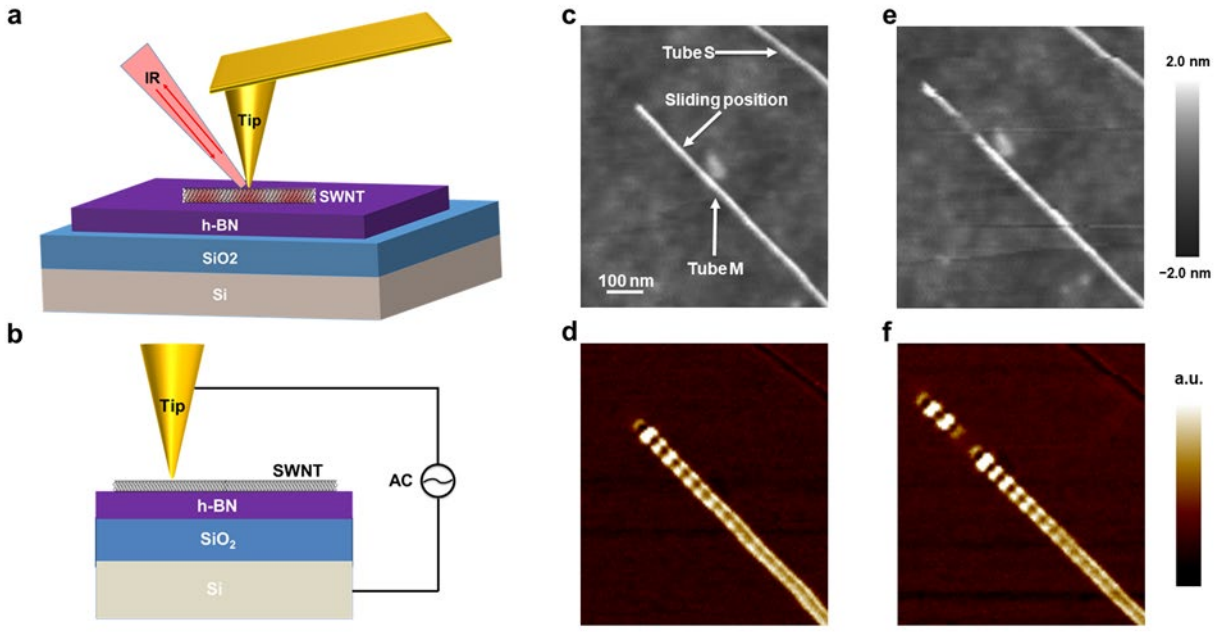

Figure 6.2 Infrared nano-imaging and scanning probe lithography of SWNTs. (a) Schematic of infrared nano-imaging of SWNTs. In brief, a gold-coated AFM tip is illuminated with a quantum cascade laser (QCL) with tunable wavelength from 11.1 to 9.5 μm. The backscattered signal from the tip-sample system carries essential plasmon information of the sample. By scanning the tip along the nanotubes, plasmon modes in the nanotubes can be visualized in real space. (b) Schematic of advanced scanning probe lithography. A high-frequency AC voltage is applied between the tip and the conductive Si layer of the substrate. Nanotube can be etched away due to oxidation of carbon by the oxygen-containing radicals generated between the tip and the nanotube. (c) Topography image of representative SWNTs. Tube M is a metallic SWNT whereas tube S is a semiconducting one. The white arrow labeled as sliding position indicates the nanoeteching position. (d) Corresponding near-field image to (c). Metallic nanotube M exhibits prominent plasmon oscillations whereas semiconducting nanotube S shows little near-field response. (e) Topography of SWNTs after nanolithography. The nanolithography results in a SWNT nanocavity with length ~ 100 nm. (f) Corresponding near-field image to (e). Plasmon modes in the nanocavity and the remaining long nanotube are visualized in real space. The excitation wavelength is 10.6 μm for the infrared nano-imaging. (c) to (f) share the same scale bar as shown in (c).

Electrode free scanning probe nanolithography (SPL) is used to trim the long metallic nanotubes into nanocavities[81-83]. The process is schematically shown in Figure 6.2b. While the tip is engaged at the desired location and brought across the nanotube, a high-frequency (~ 40 kHz) alternating voltage is applied between the AFM tip and the conductive Si layer of the substrate. This voltage generates a high-frequency AC current which penetrates the SiO_2 layer via capacitive coupling effect. As a result, a localized strong electric field can form between the tip and the nanotube, which attracts polar H_2O molecules from air and also decomposes them into oxygen-containing radicals (e.g., OH^- and O_2^-). Nanotubes can then be etched away due to oxidation of carbon by these oxygen-containing radicals. Notably, this SPL technique does not require prefabricated contact microelectrodes which are needed in conventional SPL to conduct DC

current between the tip and the sample. As a result, the nanotube nanocavities can remain ultraclean whereas conventional nanolithography techniques such as those based on electron or focused ion beams (Figure 6.1) can easily introduce defects or contaminants, compromising the quality of the nanocavities. Figure 6.2e shows a nanotube nanocavity cut at the position indicated by the white arrow in Figure 6.2c. The resulting cavity length is ~ 100 nm. Its plasmon mode, featuring two prominent symmetric peaks, is revealed by infrared nano-imaging (Figure 6.2f). The remaining larger nanotube with a newly defined end (Figure 6.2f) has a nearly identical infrared near-field response to the original uncut nanotube (Figure 6.2d), which points the cleanness of the nanoetching method.

Main factors affecting the effectiveness of the electrode free SPL are surrounding humidity, AC voltage amplitude and frequency, and suitable contact between tip and nanotube. For successful nanolithography of SWNTs, AFM works in a contact-lift mode: during forward scanning, AFM works under the normal tapping mode, where the feedback is on for tracking the topography information; during backward scanning, the metallic AFM tip is lifted down by ~ 100 nm. During the nanoetching process, we apply an AC voltage with an amplitude of 15 V and a frequency of 40 kHz. Humidity should be maintained at higher than 45% for sufficient H_2O molecules to form a water bridge between the tip and the nanotube for the oxidation. The tip sliding velocity should be less than 5 μm/s to allow sufficient interaction time with the nanotube. The accuracy of the cavity length achievable by this top-down nanolithography method is limited by the radius of the tip apex, which is ~ 20 nm in our experiment.

6.3 Visualization of Fabry-Perot Plasmon modes in SWNT Nanocavities of Different Length

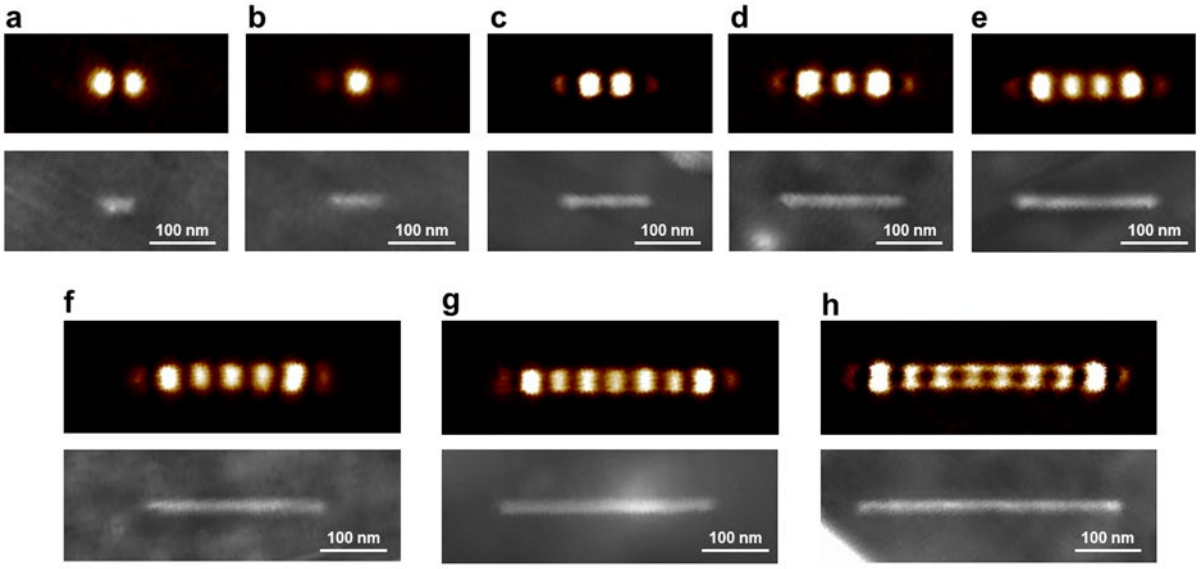

Figure 6.3 Infrared nano-imaging of SWNT nanocavities of different length. (a) to (h) Topography and corresponding near-field images for nanocavities with length ranging from 30 to 370 nm. In (a), the shortest

cavity ~ 30 nm cannot support even a single standing wave mode and the near-field response has on defined maximum at the cavity's center. With increasing cavity length from 55 to 370 nm as shown in (b) to (h), we clearly observe an increasing number l of near-field signal maxima from 1 to 8 along the nanotube, corresponding to the antinodes of the (l+1) th resonance order standing plasmon wave. The excitation wavelength is 10.6 μm for the infrared nano-imaging.

We employ this electrode-free SPL to tailor SWNTs into ultraclean nanocavities with controllable length ranging from 30 to 370 nm. The two nanocavities closest in length differ by 20 nm. Figures 6.3a-h show the topography images of different nanocavities and their corresponding near-field responses at a set excitation wavelength of 10.6 μm. Evidently, the plasmon modes depend dramatically on the length of the cavities. The nanotube nanocavities act as Fabry-Perot resonators for surface plasmons bouncing back and forth between the two ends of the cavity. The longitudinal cavity modes of the surface plasmon can be described by $2k_pL + 2\emptyset_R = 2\pi l$, where $k_p = 2\pi/\lambda_p$ is the plasmon wavevector, L is the length of the cavity, $\emptyset_R$ is the effective reflection phase by the ends and l is the resonance order. The shortest cavity ~ 30 nm cannot support even a single standing wave mode (Figure 6.3a) and the near-field response has no defined maximum at the cavity's center. With increasing cavity length from 55 to 370 nm (Figure 6.3b-h), we clearly observe an increasing number l of near-field signal maxima from 1 to 8 along the nanotube, corresponding to the antinodes of the $(l+1)$th resonance order standing plasmon wave. The separation between adjacent maxima corresponds to half of the plasmon wavelength and remains unchanged.

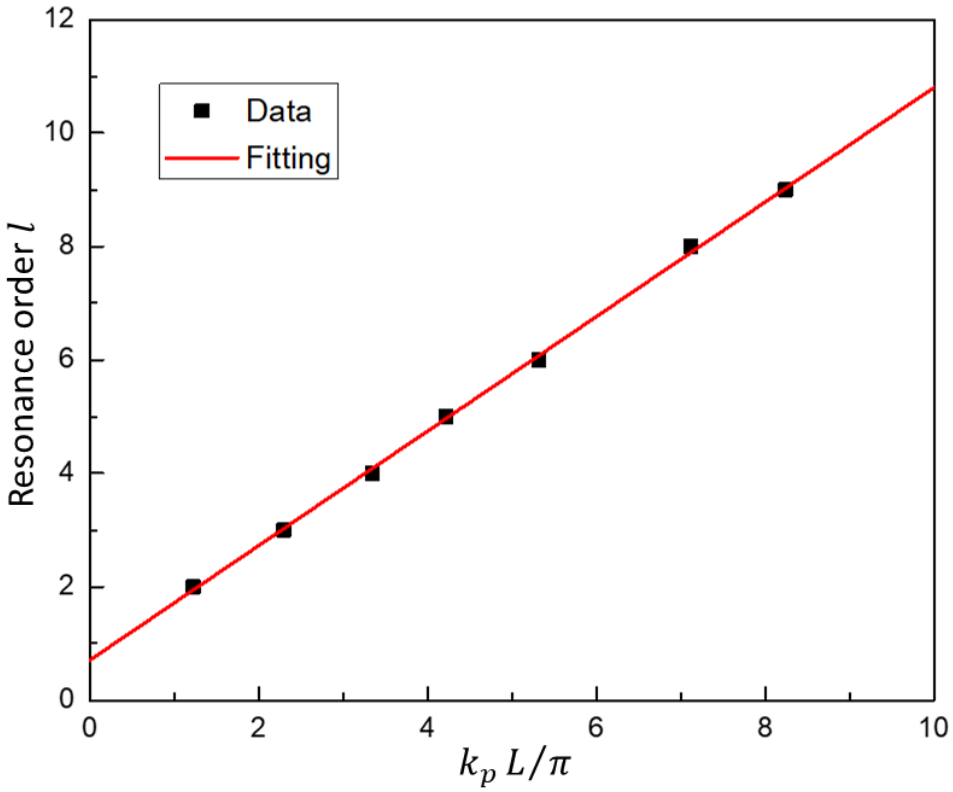

Figure 6.4 Resonance order l as a function of $k_p\, L/\pi$. Effective reflection phase $\emptyset_R$ can be extracted to be 0.70π.

The longitudinal cavity modes of the surface plasmon can be further described by $\emptyset_R/\pi + k_p L/\pi = l$. By plotting the resonance order number l against $k_p\, L/\pi$, we can extract an effective reflection phase $\emptyset_R \sim 0.70\pi$ from the intercept.

6.4 Spectrally Resolved Plasmon Resonance of Individual SWNT Nanocavities

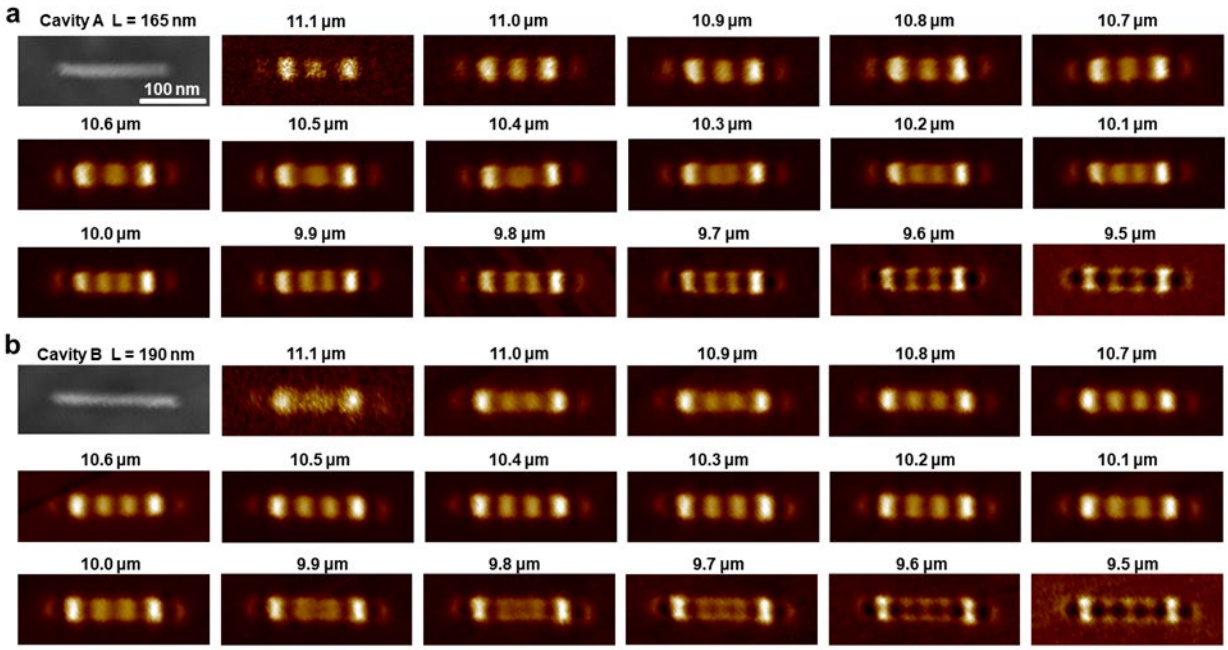

Figure 6.5 Spectral near-field responses of two SWNT nanocavities differing in length by about a quarter wavelength. (a) Topography and near-field images of nanotube cavity A with length ~ 165 nm at excitation wavelength from 11.1 to 9.5 μm. (b) Topography and near-field images of nanotube cavity B with length ~ 190 nm at excitation wavelength from 11.1 to 9.5 μm.

We further investigate the plasmon resonances in specific nanocavities by sweeping the wavelength of the excitation light λ_0, which sets the plasmon frequency ω and wavelength λ_p. The infrared nano-imaging results and analysis for a representative long metallic nanotube for the whole wavelength range starting from 11.1 and decreasing to 9.5 μm are shown in Figures 2.6 and 2.7 in Chapter 2.3. Plasmons in a long nanotube don't have cavity effects. The near-field responses of nanotube nanocavities for each wavelength are then normalized in amplitude by the responses of the long nanotube to reveal the cavity effects. As the excitation wavelength λ_0 is decreased from 11.1 to 9.5 μm, the plasmon wavelength λ_p shortens almost in a linear fashion from 98 to 76 nm. We then measure the wavelength-dependent plasmon modes in the nanocavities. Figures 6.5a and

6.5b show the near-field images of two different nanotube cavities, denoted as cavity A and B, respectively. The near-field responses for each wavelength are normalized in amplitude by the responses of the long nanotube at the same wavelength to reveal the cavity effects. Figure 6.5a displays the topography image of cavity A with length ~ 165 nm and the evolution of its near-field plasmon modes with the excitation wavelength. At 11.1 and 9.5 μm, the near-field images feature three and four crisp equally spaced maxima, respectively. Near 10.4 μm, however, a transition from three to four maxima occurs accompanied by a weakening and broadening of the center peak. In addition, Figure 6.5b shows cavity B with length ~ 190 nm along with its spectral near-field responses. While the length difference between cavity A and B is miniscule at about a quarter plasmon wavelength (~ 25 nm), this leads to strikingly different responses. Cavity B features 4 maxima in a well-defined sinusoidal wave pattern at around 10.4 μm while the transition to three and five maxima happens at 11.1 and 9.8 μm respectively. These behaviors can be qualitatively understood based on the plasmon cavity modes. The $l = 4$ and $l = 5$ plasmon cavity mode in A are resonantly excited at 11.1 and 9.5 μm laser wavelengths, respectively, while the $l = 5$ cavity mode in B is resonantly excited at 10.4 μm. The resonant modes exhibit a sinusoidal standing wave with well-defined nodes and antinodes. When the mode transition happens in cavity A at around 10.4 μm and in Cavity B at around 11.1 and 9.8 μm, the cavity resonance condition is not satisfied, and a well-defined resonance mode cannot fit nicely within the cavity. The overall response profile deviates from the simple sinusoidal wave form with less pronounced nodes and antinodes.

To further examine the spectrally resolved plasmon interference patterns in detail, we plot in Figures 6.6b and 6.6d the line profiles of near-field responses along cavity A (Figure 6.5a) and B (Figure 6.5b). The evolution with excitation wavelength can be modeled by a Fabry-Perot resonator model of a plasmon nanowaveguide terminated by highly reflective ends. As schematically shown in Figure 6.6a, we assume that a plasmon wave of constant amplitude is locally excited at studied positions along the nanocavities. The wave will propagate in both directions and be reflected back and forth by the two ends and add together to produce a collective response. By repeating the summation process at different positions along the cavities, we can record the amplitude profiles as a function of position. The loss is characterized by the quality factor Q when the plasmon wave propagates in a damped oscillator form as $e^{-2\pi x/(Q\cdot\lambda_P)}\sin\left((4\pi x)/\lambda_p\right)$. The reflection at the ends features an amplitude approximated as unity with a certain effective reflection phase $\emptyset_R$. The near-unity reflection amplitude originates from the large mode mismatch between the highly confined plasmon wave and the free space wave[54]. By adjusting the plasmon wavelength and quality factor obtained from infrared nano-imaging results for long metallic nanotubes (Figures 2.6 and 2.7 in Chapter 2.3), we acquire the simulated amplitude profiles for different excitation wavelengths from 11.1 to 9.5 μm.

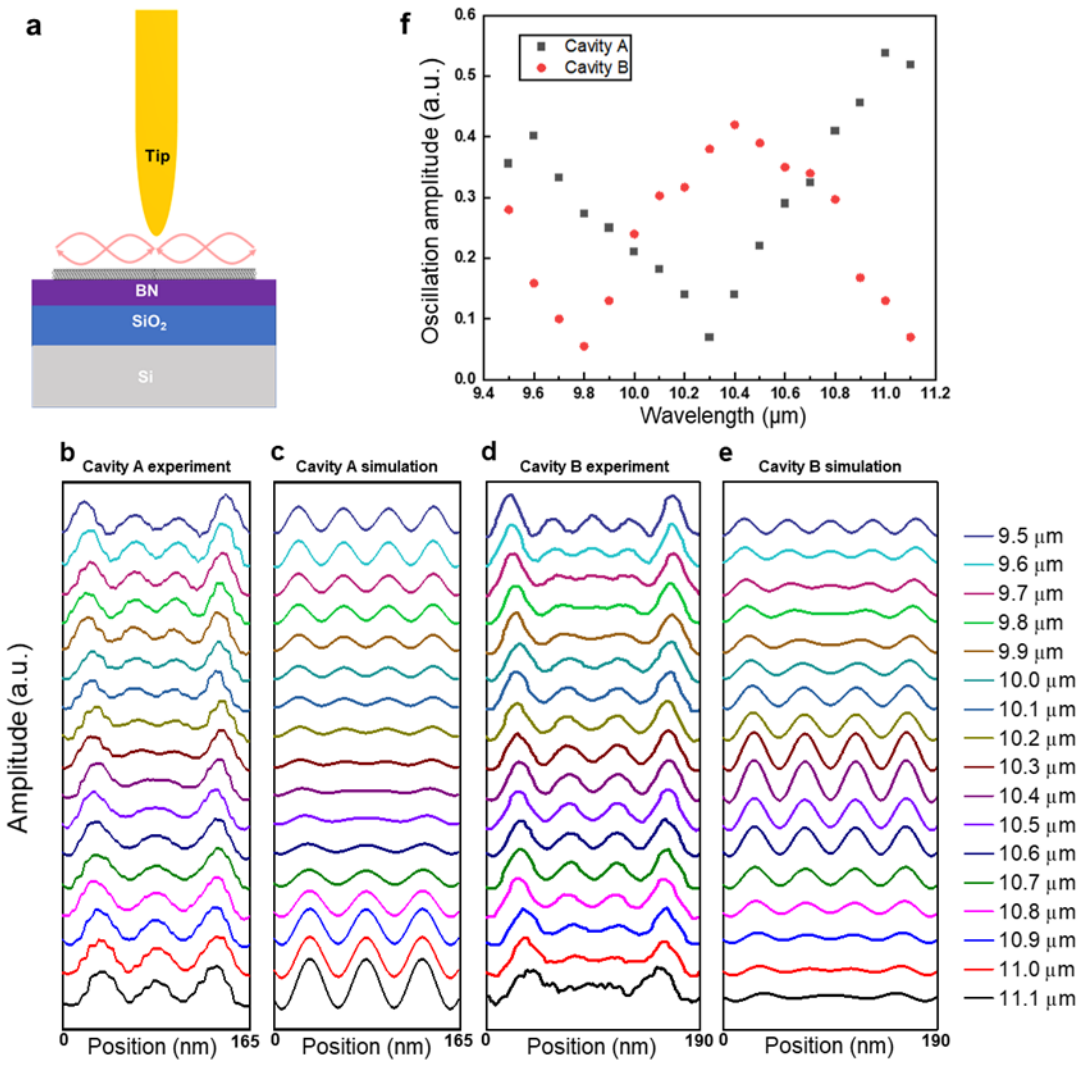

Figure 6.6 Comparison of experimental and simulated responses. (a) We assume that a plasmon wave of constant amplitude is locally excited at studied positions along the nanocavities. The wave will propagate in both directions and be reflected back and forth by the two ends and add together to produce a collective response. By repeating the summation process at different positions along the cavities, we can record the amplitude profiles as a function of position. (b) Experimental line profiles of near-field images of nanotube cavity A with length ~ 165 nm from 11.1 to 9.5 μm. (c) Simulated line profiles of nanotube cavity A by a lossy Fabry-Perot resonator model. (d) Experimental line profiles of near-field images of nanotube cavity B with length ~ 190 nm from 11.1 to 9.5 μm. (e) Simulated line profiles of nanotube cavity B by a lossy Fabry-Perot resonator model. The evolution of the experimental profiles with wavelength in the middle region of the cavity can be well captured by the model. (f) Experimental dependences of oscillation amplitude on excitation wavelength for cavity A and B.

The simulated profiles are shown in Figures 6.6c and 6.6e for comparison with experimental near-field responses shown in Figures 6.6b and 6.6d. The experimental antinodes near the ends of the cavities are noticeably stronger for all wavelengths. In addition, a relatively weak bright spot just outside the nanotube ends is also present in the experimental near-field images. Presumably, the phenomena arise from rather complicated coupling between the tip and the evanescent wave

at the nanotube end. When the nanotube plasmon wave meets its ends, the guided plasmon wave experiences a diffraction due to discontinuity in conductivity. The diffraction leads to a nonpropagating near-field evanescent wave near the ends in addition to the reflected propagating plasmon wave. The presence of the evanescent wave results in a stronger field of the antinodes near nanotube ends and a relatively weak field just outside the ends. The modified field distribution is captured by infrared nano-imaging. Similar phenomena have been reported in edge reflections of graphene plasmons. A detailed study of the phenomena in end reflections of nanotube plasmons is outside of the scope of this paper and will be reported elsewhere. Our model here accounts for the effects of the propagating wave and captures the evolution in the middle region. At 11.1 μm, cavity A is resonantly excited at order $l = 4$ and the plasmon mode shows a prominent sinusoidal wave form. The resonance condition increasingly deviates from $l = 4$ when the excitation wavelength is decreased from 11.1 to 10.4 μm, resulting in a systematic broadening and weakening of the center maxima. When the excitation wavelength is further decreased from the transition point (10.4 μm) to 9.5 μm, there is a gradual approach towards the resonance condition $l = 5$. Consequently, we see an increasing response amplitude in a better-defined sinusoidal wave form. Cavity B is longer than cavity A by about a quarter plasmon wavelength. At 10.4 μm excitation, we observe a prominent sinusoidal wave form corresponding to resonance order $l = 5$. Away from this resonance condition, there is a larger deviation from the sinusoidal wave with less pronounced nodes and antinodes. The experimental dependences of oscillation amplitude on excitation wavelength for cavity A and B are plotted in Figure 6.6f, exhibiting inverse trends. Cavity B has a well-defined plasmon resonance peak for our wavelength range. Assuming a constant quality factor Q within the wavelength range, we estimate Q of cavity B to be $\frac{\lambda_r}{\Delta\lambda_r} \sim 11.6$, where $\lambda_r \sim 10.4\ \mu m$ is the resonance wavelength for cavity B and $\Delta\lambda_r \sim 0.9\ \mu m$ is the width of the resonance peak. This estimated Q is within the range of those extracted from the imaging measurements in Figures 2.6 and 2.7 in Chapter 2.2. The dramatic dependence of the plasmon resonances on cavity length highlights the high quality and tunability of these resonators. This can have intriguing implications for wavelength selective applications such as plasmon filtering and sensing. For example, by finely controlling the cavity length and the corresponding resonance frequency, we can match the cavity resonance mode to the vibrational fingerprints of certain molecules, achieving strong resonant coupling and therefore higher sensitivity.

6.5 Summary and Outlook

In summary, advanced SPL is employed to tailor SWNTs into ultraclean nanocavities of controllable sizes. We then perform systematic spectrally resolved infrared nano-imaging of the plasmon resonances in these individual nanocavities. Assisted by theoretical modeling, the resonance behaviors can be well interpreted by a Fabry-Perot resonator model of a plasmon nanowaveguide terminated by highly reflective ends. We demonstrate that metallic SWNT nanocavities serve as one of the most compact nano-plasmonic elements with exceptional tunability and low loss.

We would like to remark that various metallic nanostructures, notably silver nanowires, have been proposed as plasmonic Fabry-Perot resonators in the visible and near-infrared range[84-86].

The plasmon spatial confinement characterized as λ_0/λ_p is typically around a few, which is much smaller than ~ 100 for SWNT cavities. The 1D plasmons in SWNTs with diameter ~ 1 nm feature even stronger transverse confinement ~ 1 nm, and the total mode volume is $V_p < 10^{-8}\,\lambda_0{}^3$. In addition, SWNT cavities have relatively lower dissipation during propagation and are also almost free from radiation damping upon reflection at cavity ends, which is evidenced by their near-unity reflection amplitude due to the large mode mismatch with free space wave. SWNT cavity-based plasmonic resonators also compare favorably to those based on graphene ribbon nanostructures, offering a higher field confinement and lower loss. Particularly, SWNT cavities do not have edges, thus avoiding additional loss mechanisms whereas the structural imperfections and contaminations at the edges of graphene nanostructures after lithography or etching can severely degrade the quality factor[87-89]. The combination of high quality factor (Q > 10) and ultra-small mode volume $V_p < 10^{-8}\,\lambda_0{}^3$ has interesting implications for enhanced light-matter interaction, for instance, in terms of Purcell factor, which describes spontaneous emission modified by the coupling to an optical cavity. A quantum emitter near the SWNT nanocavity should experience a Purcell enhancement factor $F_p = \frac{3}{4\pi^2}(\lambda_0{}^3)(\frac{Q}{V_p})$ exceeding 10^8. This is at least one order of magnitude larger than that reported so far with graphene nanoresonators or h-BN nanostructures and approaches the ultimate plasmon confinement limit[90, 91]. In addition, the coupling efficiency of an emitter to the SWNT plasmons (i.e., the fraction of decay into plasmons) has also been suggested to reach values nearing 100% over a very broad range of emitter-SWNT distances and emitter/plasmon frequencies[92]. The strong and efficient coupling between emitters and SWNT plasmons can in turn greatly affect the plasmon resonances of SWNT cavities. Therefore, SWNT cavities can act as ultracompact and ultrasensitive nanosensors by monitoring the changes in their plasmon responses.

For a broad spectrum from near-infrared to terahertz light, SWNT plasmonic nanocavities could serve in a role analogous to that of metallic nanostructures for visible frequencies. They can be further integrated, for instance, as nanoscale interconnects in nanophotonic circuits to facilitate plasmon coupling and detection. Plasmonic resonators based on metallic SWNTs nanocavities offer a viable route towards exceedingly strong and efficient light-matter interaction regime and show great promises in various appealing applications such as nanoscale lasers and amplifiers, quantum nano-optics, nonlinear nano-optics and ultra-sensitive plasmonic nanosensors potentially down to single molecules[92-96].

Bibliography

[1] A.R. Amori, Z. Hou, T.D. Krauss, Excitons in Single-Walled Carbon Nanotubes and Their Dynamics, Annual Review of Physical Chemistry, 69 (2018) 81-99.

[2] P. Avouris, M. Freitag, V. Perebeinos, Carbon-nanotube photonics and optoelectronics, Nature Photonics, 2 (2008) 341-350.

[3] R. Rao, C.L. Pint, A.E. Islam, R.S. Weatherup, S. Hofmann, E.R. Meshot, F. Wu, C. Zhou, N. Dee, P.B. Amama, J. Carpena-Nuñez, W. Shi, D.L. Plata, E.S. Penev, B.I. Yakobson, P.B. Balbuena, C. Bichara, D.N. Futaba, S. Noda, H. Shin, K.S. Kim, B. Simard, F. Mirri, M. Pasquali, F. Fornasiero, E.I. Kauppinen, M. Arnold, B.A. Cola, P. Nikolaev, S. Arepalli, H.-M. Cheng, D.N. Zakharov, E.A. Stach, J. Zhang, F. Wei, M. Terrones, D.B. Geohegan, B. Maruyama, S. Maruyama, Y. Li, W.W. Adams, A.J. Hart, Carbon Nanotubes and Related Nanomaterials: Critical Advances and Challenges for Synthesis toward Mainstream Commercial Applications, ACS Nano, DOI 10.1021/acsnano.8b06511(2018).

[4] R.H. Baughman, A.A. Zakhidov, W.A. de Heer, Carbon Nanotubes--the Route Toward Applications, Science, 297 (2002) 787-792.

[5] R. Saito, G. Dresselhaus, M.S. Dresselhaus, Physical Properties of Carbon Nanotube, Imperial College Press1998.

[6] M.S. Dresselhaus, G. Dresselhaus, P. Avouris, Carbon nanotubes: synthesis, structure, properties, and applications, Springer2001.

[7] E.A. Laird, F. Kuemmeth, G.A. Steele, K. Grove-Rasmussen, J. Nygård, K. Flensberg, L.P. Kouwenhoven, Quantum transport in carbon nanotubes, Reviews of Modern Physics, 87 (2015) 703-764.

[8] J.-C. Charlier, X. Blase, S. Roche, Electronic and transport properties of nanotubes, Reviews of Modern Physics, 79 (2007) 677-732.

[9] M.S. Dresselhaus, G. Dresselhaus, R. Saito, A. Jorio, Raman spectroscopy of carbon nanotubes, Physics Reports, 409 (2005) 47-99.

[10] J. Wang, Carbon-Nanotube Based Electrochemical Biosensors: A Review, Electroanalysis, 17 (2005) 7-14.

[11] M.J. Biercuk, S. Ilani, C.M. Marcus, P.L. McEuen, Electrical Transport in Single-Wall Carbon Nanotubes, in: A. Jorio, G. Dresselhaus, M.S. Dresselhaus (Eds.) Carbon Nanotubes: Advanced Topics in the Synthesis, Structure, Properties and Applications, Springer Berlin Heidelberg, Berlin, Heidelberg, 2008, pp. 455-493.

[12] N. Gupta, S.M. Gupta, S.K. Sharma, Carbon nanotubes: synthesis, properties and engineering applications, Carbon Letters, 29 (2019) 419-447.

[13] A. Reina, M. Hofmann, D. Zhu, J. Kong, Growth Mechanism of Long and Horizontally Aligned Carbon Nanotubes by Chemical Vapor Deposition, The Journal of Physical Chemistry C, 111 (2007) 7292-7297.

[14] M. Nasseri, A. Ansary, M.J. Boland, D.R. Strachan, Aligned van der Waals Coupled Growth of Carbon Nanotubes to Hexagonal Boron Nitride, Advanced Materials Interfaces, 0 1800793.

[15] R.J. Hermann, M.J. Gordon, Nanoscale Optical Microscopy and Spectroscopy Using Near-Field Probes, Annual Review of Chemical and Biomolecular Engineering, 9 (2018) 365-387.

[16] G. Hills, C. Lau, A. Wright, S. Fuller, M.D. Bishop, T. Srimani, P. Kanhaiya, R. Ho, A. Amer, Y. Stein, D. Murphy, Arvind, A. Chandrakasan, M.M. Shulaker, Modern microprocessor built from complementary carbon nanotube transistors, Nature, 572 (2019) 595-602.

[17] I. Shapir, A. Hamo, S. Pecker, C.P. Moca, Ö. Legeza, G. Zarand, S. Ilani, Imaging the electronic Wigner crystal in one dimension, Science, 364 (2019) 870-875.

[18] B. Liu, F. Wu, H. Gui, M. Zheng, C. Zhou, Chirality-Controlled Synthesis and Applications of Single-Wall Carbon Nanotubes, ACS Nano, 11 (2017) 31-53.

[19] S. Zhao, S. Wang, F. Wu, W. Shi, I.B. Utama, T. Lyu, L. Jiang, Y. Su, S. Wang, K. Watanabe, T. Taniguchi, A. Zettl, X. Zhang, C. Zhou, F. Wang, Correlation of Electron Tunneling and Plasmon Propagation in a Luttinger Liquid, Physical Review Letters, 121 (2018) 047702.

[20] S. Wang, F. Wu, S. Zhao, K. Watanabe, T. Taniguchi, C. Zhou, F. Wang, Logarithm Diameter Scaling and Carrier Density Independence of One-Dimensional Luttinger Liquid Plasmon, Nano Letters, 19 (2019) 2360-2365.

[21] S. Wang, F. Wu, K. Watanabe, T. Taniguchi, C. Zhou, F. Wang, Metallic Carbon Nanotube Nanocavities as Ultra-compact and Low-loss Fabry-Perot Plasmonic Resonators, Nano Letters, DOI 10.1021/acs.nanolett.0c00315(2020).

[22] S. Wang, S. Zhao, Z. Shi, F. Wu, Z. Zhao, L. Jiang, K. Watanabe, T. Taniguchi, A. Zettl, C. Zhou, F. Wang, Nonlinear Luttinger liquid plasmons in semiconducting single-walled carbon nanotubes, Nature Materials, DOI 10.1038/s41563-020-0652-5(2020).

[23] K.S. Novoselov, A.K. Geim, S.V. Morozov, D. Jiang, M.I. Katsnelson, I.V. Grigorieva, S.V. Dubonos, A.A. Firsov, Two-dimensional gas of massless Dirac fermions in graphene, Nature, 438 (2005) 197-200.

[24] Y. Zhang, Y.-W. Tan, H.L. Stormer, P. Kim, Experimental observation of the quantum Hall effect and Berry's phase in graphene, Nature, 438 (2005) 201-204.

[25] E.H. Hwang, S. Adam, S.D. Sarma, Carrier Transport in Two-Dimensional Graphene Layers, Physical Review Letters, 98 (2007) 186806.

[26] C.L. Kane, E.J. Mele, Size, Shape, and Low Energy Electronic Structure of Carbon Nanotubes, Physical Review Letters, 78 (1997) 1932-1935.

[27] A.A. Maarouf, C.L. Kane, E.J. Mele, Electronic structure of carbon nanotube ropes, Physical Review B, 61 (2000) 11156-11165.

[28] X. Blase, L.X. Benedict, E.L. Shirley, S.G. Louie, Hybridization effects and metallicity in small radius carbon nanotubes, Physical Review Letters, 72 (1994) 1878-1881.

[29] C. Rutherglen, A.A. Kane, P.F. Marsh, T.A. Cain, B.I. Hassan, M.R. AlShareef, C. Zhou, K. Galatsis, Wafer-scalable, aligned carbon nanotube transistors operating at frequencies of over 100 GHz, Nature Electronics, 2 (2019) 530-539.

[30] F. Wang, G. Dukovic, L.E. Brus, T.F. Heinz, The Optical Resonances in Carbon Nanotubes Arise from Excitons, Science, 308 (2005) 838-841.

[31] K. Liu, J. Deslippe, F. Xiao, R.B. Capaz, X. Hong, S. Aloni, A. Zettl, W. Wang, X. Bai, S.G. Louie, E. Wang, F. Wang, An atlas of carbon nanotube optical transitions, Nat Nano, 7 (2012) 325-329.

[32] V. Schroeder, S. Savagatrup, M. He, S. Lin, T.M. Swager, Carbon Nanotube Chemical Sensors, Chemical Reviews, 119 (2019) 599-663.

[33] M. Foldvari, M. Bagonluri, Carbon nanotubes as functional excipients for nanomedicines: II. Drug delivery and biocompatibility issues, Nanomedicine: Nanotechnology, Biology and Medicine, 4 (2008) 183-200.

[34] G. Baym, C. Pethick, Landau Fermi-liquid theory: concepts and applications, John Wiley & Sons2008.

[35] L.I. Glazman, Testing the nonlinear Luttinger liquid, Nature Materials, DOI 10.1038/s41563-020-0675-y(2020).

[36] C. Kittel, Introduction to solid state physics, Wiley New York1976.

[37] S.-i. Tomonaga, Remarks on Bloch's method of sound waves applied to many-fermion problems, Progress of Theoretical Physics, 5 (1950) 544-569.

[38] J.M. Luttinger, An Exactly Soluble Model of a Many-Fermion System, Journal of Mathematical Physics, 4 (1963) 1154-&.

[39] F.D.M. Haldane, 'Luttinger liquid theory' of one-dimensional quantum fluids. I. Properties of the Luttinger model and their extension to the general 1D interacting spinless Fermi gas, Journal of Physics C: Solid State Physics, 14 (1981) 2585.

[40] C. Kane, L. Balents, M.P.A. Fisher, Coulomb interactions and mesoscopic effects in carbon nanotubes, Physical Review Letters, 79 (1997) 5086-5089.

[41] M. Bockrath, D.H. Cobden, P.L. McEuen, N.G. Chopra, A. Zettl, A. Thess, R.E. Smalley, Single-electron transport in ropes of carbon nanotubes, Science, 275 (1997) 1922-1925.

[42] M. Bockrath, D.H. Cobden, J. Lu, A.G. Rinzler, R.E. Smalley, L. Balents, P.L. McEuen, Luttinger-liquid behaviour in carbon nanotubes, Nature, 397 (1999) 598-601.

[43] Z. Yao, H.W.C. Postma, L. Balents, C. Dekker, Carbon nanotube intramolecular junctions, Nature, 402 (1999) 273-276.

[44] J. Lee, S. Eggert, H. Kim, S.J. Kahng, H. Shinohara, Y. Kuk, Real Space Imaging of One-Dimensional Standing Waves: Direct Evidence for a Luttinger Liquid, Physical Review Letters, 93 (2004) 166403.

[45] S.J. Tans, A.R.M. Verschueren, C. Dekker, Room-temperature transistor based on a single carbon nanotube, Nature, 393 (1998) 49.

[46] A. Imambekov, T.L. Schmidt, L.I. Glazman, One-dimensional quantum liquids: Beyond the Luttinger liquid paradigm, Reviews of Modern Physics, 84 (2012) 1253-1306.

[47] A. Imambekov, L.I. Glazman, Universal Theory of Nonlinear Luttinger Liquids, Science, 323 (2009) 228-231.

[48] A. Lereu, A. Passian, P. Dumas, Near field optical microscopy: a brief review, International journal of nanotechnology, 9 (2012) 488.

[49] J. Takahara, S. Yamagishi, H. Taki, A. Morimoto, T. Kobayashi, Guiding of a one-dimensional optical beam with nanometer diameter, Opt. Lett., 22 (1997) 475-477.

[50] S. Soleymani, S. Golmohammadi, Surface Plasmon Polaritons Propagation Along Armchair and Zigzag Single-Wall Carbon Nanotubes With Different Radii, IEEE Transactions on Nanotechnology, 16 (2017) 307-314.

[51] H. Wei, S. Zhang, X. Tian, H. Xu, Highly tunable propagating surface plasmons on supported silver nanowires, Proceedings of the National Academy of Sciences, 110 (2013) 4494-4499.

[52] Z. Fei, A.S. Rodin, G.O. Andreev, W. Bao, A.S. McLeod, M. Wagner, L.M. Zhang, Z. Zhao, M. Thiemens, G. Dominguez, M.M. Fogler, A.H.C. Neto, C.N. Lau, F. Keilmann, D.N. Basov, Gate-tuning of graphene plasmons revealed by infrared nano-imaging, Nature, 487 (2012) 82-85.

[53] J.A. Scholl, A.L. Koh, J.A. Dionne, Quantum plasmon resonances of individual metallic nanoparticles, Nature, 483 (2012) 421.

[54] J.-H. Kang, S. Wang, Z. Shi, W. Zhao, E. Yablonovitch, F. Wang, Goos-Hänchen Shift and Even–Odd Peak Oscillations in Edge-Reflections of Surface Polaritons in Atomically Thin Crystals, Nano Letters, 17 (2017) 1768-1774.

[55] Electrons in one dimension and the Luttinger liquid, in: G. Giuliani, G. Vignale (Eds.) Quantum Theory of the Electron Liquid, Cambridge University Press, Cambridge, 2005, pp. 501-549.

[56] B. Gao, A. Komnik, R. Egger, D.C. Glattli, A. Bachtold, Evidence for Luttinger-Liquid Behavior in Crossed Metallic Single-Wall Nanotubes, Physical Review Letters, 92 (2004) 216804.

[57] N.Y. Kim, P. Recher, W.D. Oliver, Y. Yamamoto, J. Kong, H. Dai, Tomonaga-Luttinger Liquid Features in Ballistic Single-Walled Carbon Nanotubes: Conductance and Shot Noise, Physical Review Letters, 99 (2007) 036802.

[58] A. Komnik, R. Egger, Nonequilibrium Transport for Crossed Luttinger Liquids, Physical Review Letters, 80 (1998) 2881-2884.

[59] T. Giamarchi, Quantum physics in one dimension, Oxford university press2004.

[60] Y. Jompol, C.J.B. Ford, J.P. Griffiths, I. Farrer, G.A.C. Jones, D. Anderson, D.A. Ritchie, T.W. Silk, A.J. Schofield, Probing Spin-Charge Separation in a Tomonaga-Luttinger Liquid, Science, 325 (2009) 597-601.

[61] V.V. Deshpande, M. Bockrath, L.I. Glazman, A. Yacoby, Electron liquids and solids in one dimension, Nature, 464 (2010) 209-216.

[62] Y. Jin, O. Tsyplyatyev, M. Moreno, A. Anthore, W.K. Tan, J.P. Griffiths, I. Farrer, D.A. Ritchie, L.I. Glazman, A.J. Schofield, C.J.B. Ford, Momentum-dependent power law measured in an interacting quantum wire beyond the Luttinger limit, Nature Communications, 10 (2019) 2821.

[63] M. Moreno, C.J.B. Ford, Y. Jin, J.P. Griffiths, I. Farrer, G.A.C. Jones, D.A. Ritchie, O. Tsyplyatyev, A.J. Schofield, Nonlinear spectra of spinons and holons in short GaAs quantum wires, Nature Communications, 7 (2016) 12784.

[64] T.L. Schmidt, A. Imambekov, L.I. Glazman, Spin-charge separation in one-dimensional fermion systems beyond Luttinger liquid theory, Physical Review B, 82 (2010) 245104.

[65] G. Barak, H. Steinberg, L.N. Pfeiffer, K.W. West, L. Glazman, F. von Oppen, A. Yacoby, Interacting electrons in one dimension beyond the Luttinger-liquid limit, Nature Physics, 6 (2010) 489.

[66] A. Imambekov, L.I. Glazman, Phenomenology of One-Dimensional Quantum Liquids Beyond the Low-Energy Limit, Physical Review Letters, 102 (2009) 126405.

[67] M. Pustilnik, M. Khodas, A. Kamenev, L.I. Glazman, Dynamic Response of One-Dimensional Interacting Fermions, Physical Review Letters, 96 (2006) 196405.

[68] P.F. Williams, A.N. Bloch, Self-consisten dielectric response of a quasi-one-dimensional metal at high frequencies, Physical Review B, 10 (1974) 1097-1108.

[69] S. Das Sarma, E.H. Hwang, Dynamical response of a one-dimensional quantum-wire electron system, Physical Review B, 54 (1996) 1936-1946.

[70] X. Zhou, J.-Y. Park, S. Huang, J. Liu, P.L. McEuen, Band Structure, Phonon Scattering, and the Performance Limit of Single-Walled Carbon Nanotube Transistors, Physical Review Letters, 95 (2005) 146805.

[71] M.S. Purewal, B.H. Hong, A. Ravi, B. Chandra, J. Hone, P. Kim, Scaling of Resistance and Electron Mean Free Path of Single-Walled Carbon Nanotubes, Physical Review Letters, 98 (2007) 186808.

[72] X. He, H. Htoon, S.K. Doorn, W.H.P. Pernice, F. Pyatkov, R. Krupke, A. Jeantet, Y. Chassagneux, C. Voisin, Carbon nanotubes as emerging quantum-light sources, Nature Materials, DOI 10.1038/s41563-018-0109-2(2018).

[73] E. Ozbay, Plasmonics: Merging Photonics and Electronics at Nanoscale Dimensions, Science, 311 (2006) 189-193.

[74] A.F. Koenderink, A. Alù, A. Polman, Nanophotonics: Shrinking light-based technology, Science, 348 (2015) 516-521.

[75] J.A. Schuller, E.S. Barnard, W. Cai, Y.C. Jun, J.S. White, M.L. Brongersma, Plasmonics for extreme light concentration and manipulation, Nature Materials, 9 (2010) 193.

[76] D.K. Gramotnev, S.I. Bozhevolnyi, Plasmonics beyond the diffraction limit, Nature Photonics, 4 (2010) 83.

[77] R. Zia, M.D. Selker, M.L. Brongersma, Leaky and bound modes of surface plasmon waveguides, Physical Review B, 71 (2005) 165431.

[78] M. Tamagnone, A. Ambrosio, K. Chaudhary, L.A. Jauregui, P. Kim, W.L. Wilson, F. Capasso, Ultra-confined mid-infrared resonant phonon polaritons in van der Waals nanostructures, Science Advances, 4 (2018).

[79] D. Siyuan, T. Mykhailo, Y. Yafang, M. Qiong, P.V. Marta, W. Kenji, T. Takashi, J.H. Pablo, F.M. M., A. Andrea, B.D. N., Manipulation and Steering of Hyperbolic Surface Polaritons in Hexagonal Boron Nitride, Advanced Materials, 30 (2018) 1706358.

[80] M. Autore, P. Li, I. Dolado, F.J. Alfaro-Mozaz, R. Esteban, A. Atxabal, F. Casanova, L.E. Hueso, P. Alonso-González, J. Aizpurua, A.Y. Nikitin, S. Vélez, R. Hillenbrand, Boron nitride nanoresonators for phonon-enhanced molecular vibrational spectroscopy at the strong coupling limit, Light: Science &Amp; Applications, 7 (2018) 17172.

[81] H. Li, Z. Ying, B. Lyu, A. Deng, L. Wang, T. Taniguchi, K. Watanabe, Z. Shi, Electrode-Free Anodic Oxidation Nanolithography of Low-Dimensional Materials, Nano Letters, DOI 10.1021/acs.nanolett.8b04166(2018).

[82] R. Garcia, A.W. Knoll, E. Riedo, Advanced scanning probe lithography, Nature Nanotechnology, 9 (2014) 577.

[83] J.-Y. Park, Y. Yaish, M. Brink, S. Rosenblatt, P.L. McEuen, Electrical cutting and nicking of carbon nanotubes using an atomic force microscope, Applied Physics Letters, 80 (2002) 4446-4448.

[84] Surface plasmon polaritons in metal stripes and wires, Philosophical Transactions of the Royal Society of London A: Mathematical, Physical and Engineering Sciences, 362 (2004) 739-756.

[85] H. Ditlbacher, A. Hohenau, D. Wagner, U. Kreibig, M. Rogers, F. Hofer, F.R. Aussenegg, J.R. Krenn, Silver Nanowires as Surface Plasmon Resonators, Physical Review Letters, 95 (2005) 257403.

[86] M. Allione, V.V. Temnov, Y. Fedutik, U. Woggon, M.V. Artemyev, Surface Plasmon Mediated Interference Phenomena in Low-Q Silver Nanowire Cavities, Nano Letters, 8 (2008) 31-35.

[87] V.W. Brar, M.S. Jang, M. Sherrott, J.J. Lopez, H.A. Atwater, Highly Confined Tunable Mid-Infrared Plasmonics in Graphene Nanoresonators, Nano Letters, 13 (2013) 2541-2547.

[88] I. Soto Lamata, P. Alonso-González, R. Hillenbrand, A.Y. Nikitin, Plasmons in Cylindrical 2D Materials as a Platform for Nanophotonic Circuits, ACS Photonics, 2 (2015) 280-286.

[89] A.Y. Nikitin, P. Alonso González, VélezS, MastelS, CentenoA, PesqueraA, ZurutuzaA, CasanovaF, L.E. Hueso, F.H.L. Koppens, HillenbrandR, Real-space mapping of tailored sheet and edge plasmons in graphene nanoresonators, Nat Photon, 10 (2016) 239-243.

[90] R. Chikkaraddy, B. de Nijs, F. Benz, S.J. Barrow, O.A. Scherman, E. Rosta, A. Demetriadou, P. Fox, O. Hess, J.J. Baumberg, Single-molecule strong coupling at room temperature in plasmonic nanocavities, Nature, 535 (2016) 127.

[91] D. Alcaraz Iranzo, S. Nanot, E.J.C. Dias, I. Epstein, C. Peng, D.K. Efetov, M.B. Lundeberg, R. Parret, J. Osmond, J.-Y. Hong, J. Kong, D.R. Englund, N.M.R. Peres, F.H.L. Koppens, Probing the ultimate plasmon confinement limits with a van der Waals heterostructure, Science, 360 (2018) 291-295.

[92] L. Martín-Moreno, F.J.G. de Abajo, F.J. García-Vidal, Ultraefficient Coupling of a Quantum Emitter to the Tunable Guided Plasmons of a Carbon Nanotube, Physical Review Letters, 115 (2015) 173601.

[93] N.P. de Leon, B.J. Shields, C.L. Yu, D.E. Englund, A.V. Akimov, M.D. Lukin, H. Park, Tailoring Light-Matter Interaction with a Nanoscale Plasmon Resonator, Physical Review Letters, 108 (2012) 226803.

[94] A.S. Kadochkin, S.G. Moiseev, Y.S. Dadoenkova, V.V. Svetukhin, I.O. Zolotovskii, Surface plasmon polariton amplification in a single-walled carbon nanotube, Opt. Express, 25 (2017) 27165-27171.

[95] P.-H. Ho, D.B. Farmer, G.S. Tulevski, S.-J. Han, D.M. Bishop, L.M. Gignac, J. Bucchignano, P. Avouris, A.L. Falk, Intrinsically ultrastrong plasmon–exciton interactions in crystallized films of carbon nanotubes, Proceedings of the National Academy of Sciences, DOI 10.1073/pnas.1816251115(2018).

[96] T. Uda, A. Ishii, Y.K. Kato, Single Carbon Nanotubes as Ultrasmall All-Optical Memories, ACS Photonics, 5 (2018) 559-565.